

Laser-Compton Gamma-Ray Source by using 2 μ m Tm-Laser

Sho Amano, Shuji Miyamoto
LASTI/UH

Abstract

In order to expand energy range of the Compton gamma-ray, we considered to introduce a Tm-fiber laser operating at 2 μ m to generate gamma rays in the energy range of 4–21 MeV, using a laser-focusing design to generate the maximum flux. The generated luminosity is calculated to be 6400 photons/(W·mA·s) with a laser power of 4 W and a beam current of 200 mA. This is at the same level as for the Nd:YVO₄, and CO₂, laser. Tm-fiber laser is also capable of operating in a high-power regime and can generate kW-level output power. At present, the maximum gamma-ray flux is limited only by the laser power. When operating the laser at 1 kW of output power with a beam current of 200 mA, we expect a flux of up to $\sim 10^9$ photons/s. At NewSUBARU, up to several dozen MeV gamma-ray sources are capable of generating such high power.

Introduction

Initially, we generated gamma rays in the range of 17–37 MeV by using a Nd:YVO₄ laser operating at 1.06 μ m. The gamma-ray source is used for various studies. Several applications, however, demand gamma-ray energies of several MeV, prompting us to install a CO₂ laser operating at 10.6 μ m to generate gamma rays in the range of 1–4 MeV. In addition to the Nd:YVO₄ and the CO₂ lasers, the installation of a third laser with a wavelength of approximately 2 μ m is planned to generate gamma rays in the energy range that is not currently attainable. With the addition of the 2- μ m laser, we will have the capacity to generate gamma rays with a continuously tunable energy range from 1 to 37 MeV. The Tm-doped fiber laser is a candidate for the 2- μ m laser. Recently, a high-power Tm-doped fiber laser has been developed with an output power at the kW level. In general, both Nd:YVO₄ and CO₂ lasers are capable of operating in a high-power regime, and output powers exceeding the kW level have already been achieved. Because the laser-Compton gamma-ray flux is proportional to power of the driving laser, these high power lasers make it possible to generate a high flux of gamma rays. Thus, by using the high power lasers, the gamma-ray source in NewSUBARU will be capable of producing a high flux of gamma rays in the energy spectrum from 1 to 37 MeV.

In this paper, we present a theoretical prediction of the performance expected using a 2- μ m laser.

Compton gamma-ray beamline (BL1a)

Figure 1 shows the experimental setup of the laser-Compton gamma-ray source in NewSUBARU, which is an electron storage ring with stored energies from 0.7 to 1.5 GeV. Laser-Compton gamma-ray experiments are conducted on one of the straight sections in combination

with beamline 1 (BL1). The Nd:YVO₄ and CO₂ lasers are installed in the experimental hall, and only the beam transport path for the Nd:YVO₄ or CO₂ laser is shown in Fig.1. The beam transport paths for the Nd:YVO₄ and CO₂ laser are called the N-path and the C-path, respectively. The transmittance of each path corresponds to each laser wavelength and each path has an optimized collision point (A or B) for laser beam and electron. Figure 2 shows the RMS size of the electron beam calculated from Twiss parameters, and the laser beam radii ($1/e^2$) in the straight section. To maximize the interaction length, the focusing optic in the N-path of the Nd:YVO₄ laser (1.064 μ m) is designed to create a laser spot with a radius of 0.5 mm at position A at the center of the straight section, which is one advantage offered by NewSUBARU. At position A, the laser beam collides with the electron beam, which is of nearly equal size. However, in the C-path the focusing optics were redesigned to focus the laser at position B near the laser window; because diffraction is an order of magnitude greater than for the Nd:YVO₄ laser. Considering the effective hard apertures along the C-path, we find that the radius of the laser spot is 1.2 mm at position B, which is about twice the size of the electron beam.

Calculated results

By introducing a 2- μ m laser, we expect to be able to generate gamma rays with energies spanning the 4- to 21-MeV range, with electron energies tuned to 0.7–1.5 GeV. Thus, driving with such a laser will enable us to generate gamma rays spanning an energy range that is not attainable using the present lasers. We proceeded by considering a beam transport path for a 2- μ m laser and calculating the expected gamma-ray luminosity. The first case considered entailed passing the 2- μ m laser beam through the N-path so that it collides with the equal-sized electron

beam at point A. However, this design proved unsatisfactory because of diffraction losses for the 2- μm laser. We next considered the following two cases (Fig. 2): (1) At point A, the 2- μm laser beam that has passed through the N-path collides with the electron beam. The laser beam radius at point A is 1.2 mm (twice as large as the radius of the electron beam). (2) At point B, a laser beam that has passed through the C-path collides with the electron beam. The laser beam radius at point B is 0.6 mm, which is the same size as the electron beam. From the same calculation that produced results for the case of the Nd:YVO₄ and CO₂ lasers, we estimate a luminosity for cases (1) and (2) to be 6400 photons/(W·mA·s) and 3500 photons/(W·mA·s), respectively. We conclude that higher luminosity can be obtained for case (1), with the collision at point A, where the long interaction zone may be used with advantage even with a large laser beam radius. Under these conditions, the luminosity of the gamma rays generated by a 2- μm laser should be at the same level as for the Nd:YVO₄ and CO₂ lasers.

At present, gamma-rays with energies of 17–37 MeV and 1.7–3.9 MeV are achieved using an Nd:YVO₄ and a CO₂ laser, respectively, and the luminosities obtained in both cases are 6000–7000 photons/(W·mA·s). The maximum gamma-ray flux is currently 5×10^6 photons/s, obtained using a laser power of 4 W and an electron-beam current of 200 mA. We also estimate that the gamma-ray luminosity produced by a 2- μm laser should be 6400 photons/(W·mA·s), with energies covering the range of 4–21 MeV.

Nd:YVO₄, CO₂, and Tm-doped fiber lasers (the latter as a 2- μm laser) are all capable of generating kW-level output power. Using this level laser power with an electron-beam current of 200 mA allows a gamma-ray flux of 10^9 photons/s to be achieved. Thus, the laser-Compton gamma-ray source in NewSUBARU has the potential to generate such high fluxes over a continuously tunable energy range from 1 to 37 MeV.

References

- [1] S.Amano *et al.*, AIP Conf. Proc, **1234**, pp.489 (2010).

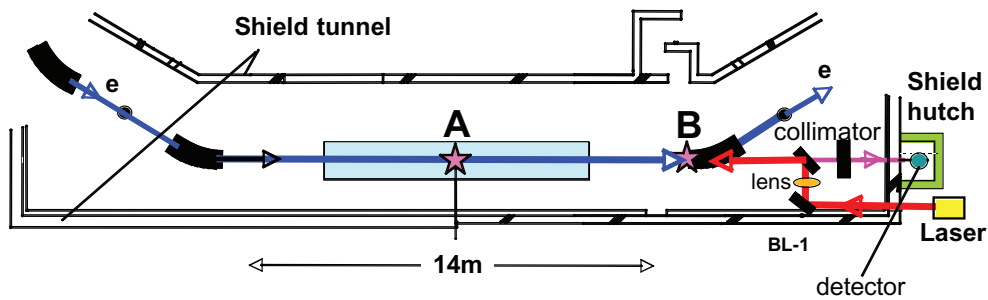


FIG1. Experimental setup of laser Compton gamma-ray

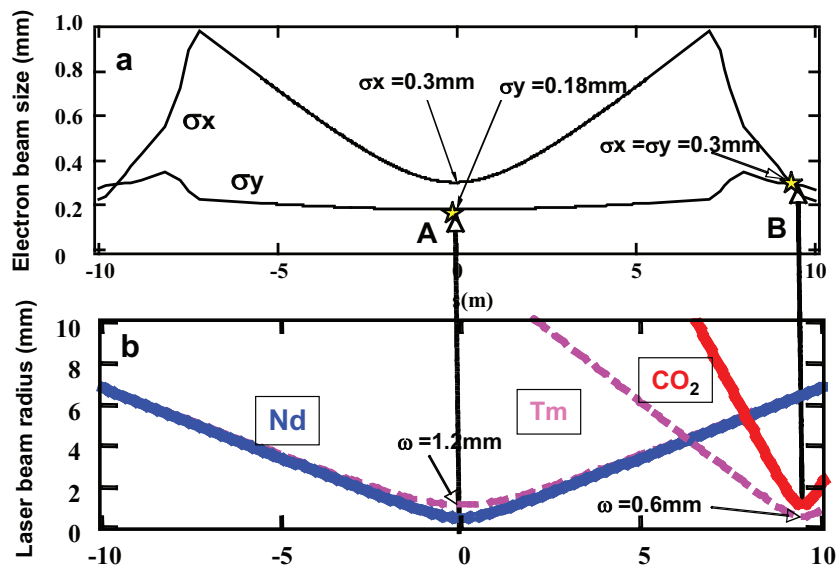


FIG2. (a) Electron beam size and (b) laser beam radius of the Nd:YVO₄, CO₂ and Tm lasers in the interaction zone. The zero value on the horizontal axis refers to the center of the long straight section.

Sun

Imaging for Stress Corrosion Cracking in Stainless Steel with Laser Compton Scattering Gamma Ray

T.Hasegawa¹⁾, S.Nakahigashi¹⁾, T.Fujishiro²⁾, K.Horikawa³⁾, M.Terasawa³⁾ and S.Miyamoto³⁾

¹⁾Japan Power Engineering and Inspection Corporation, ²⁾University of Hyogo, ³⁾LASTI, University of Hyogo

Abstract

In order to detect SCC non-destructively, laser compton scattering gamma ray imaging was examined. As a result, imaging with 1.76MeV gamma ray was available to detect artificial slit for 30mm thick stainless steel and SCC for 10mm thick stainless steel.

Introduction

The simulation technique for ultrasonic propagation is very useful as a support tool to analyze the result of practical ultrasonic testing (UT). In Japan power Engineering and Inspection Corporation (JAEIC), large-scale ultrasonic simulation system used finite element method has been developed and put to practical use [1-3].

In ultrasonic simulation, the information, such as specimen shape, physical properties of specimen, three-dimensional defect shape and distribution, is necessary. Particularly, the information about defect is very important to evaluate the validity of simulation model and to simulate more accurately.

Stress corrosion cracking (SCC), known as a defect occurred in the structure in nuclear power plant or chemical plant, has very intricate ramification and narrow crack width. Therefore, it has been difficult to observe actual 3D SCC shape in the specimen so far.

Recently, the authors have succeeded for the first time to observe 3D SCC image occurred in stainless steel and nickel-based alloy by synchrotron radiation used Spring-8, synchrotron radiation facility [4-5]. Fig.1 shows the 3D CT image of SCC in stainless steel as an example [6]. However, it was impossible to compare the actual result of UT since the size of specimen was very small (a few mm diameters) and UT was not available.

Therefore, we tried to perform imaging experiment by gamma(γ) ray for larger size of specimen (a few dozens of millimeter thick).

Experiments

SUS316L stainless steels were used as specimens in this imaging experiment. For each specimen, SCC was artificially developed in high-pressure pure hot water at 300°C. SCC specimen size was 10x10mm and the thickness was from 10 to 50mm. Fig.1 shows the SCC specimen. Some of SUS316L blocks were prepared as standard specimen machined the slit artificially. We also prepared the weld joint specimen with SCC. The base metal was SUS304 and filler metal was SUS308. The thickness of specimen was 10mm.

Imaging experiment was performed by γ ray in NEW SUBARU BL01A. In this experiment, γ ray

was generated by collision between CO₂ laser and electron. This γ ray energy was 1.76MeV. Imaging plate (IP) which had 50um resolution was utilized to detect the image. Table 1 shows the examination condition and fig.2 shows experimental equipment, respectively.

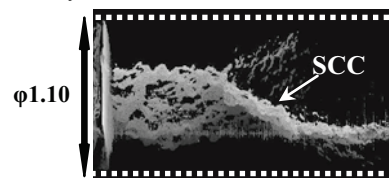


Fig.1 Three dimensional CT image of SCC in stainless steel observed by synchrotron radiation [6].

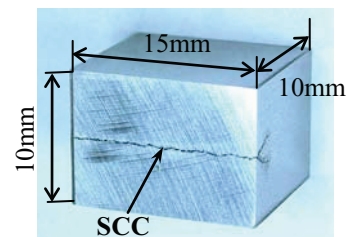


Fig.2 SCC specimen for imaging experiment.

Table 1. Experimental condition.

Electron energy	1.0 GeV
Laser	CO ₂ laser (λ :10.54um)
Gamma ray energy	1.76MeV
Irradiation time	1h, 3h, 6h, 9h
Image detection	Imaging plate
Specimen thickness	10-50mm
Artificial slit	Width:0.245mm Depth:1mm~5mm

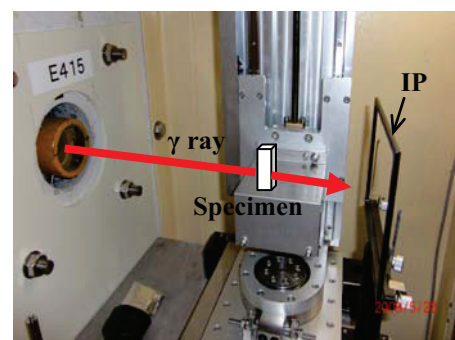


Fig.2 Experimental equipment.

Experimental results

Imaging experiment was performed for 10mm thick standard specimen which had 21 slits (width: 0.245mm, depth: ~1.7mm) at 2mm intervals. Fig.3 shows the image for standard specimen. 7 slits were confirmed both sides of beam center on the image. The slit images between third and sixth from beam center were clear. The energy of γ ray at the position from third to sixth slit was estimated at 0.6 ~1.0MeV in calculation.

In order to examine effects of specimen thickness and irradiation time for the image contrast, imaging experiments for two kinds of standard specimen with 10mm and 30mm thick were carried out. Irradiation times were 3hrs, 6hrs and 9hrs. Fig.4 shows the result of 3hrs irradiation as an example. In cases of slit size in this experiment, there was no remarkable difference in the slit image contrast between 10mm and 30mm thick specimen. The image resolution was saturated above 6hrs irradiation although the image was clearer with increasing with irradiation time until 6hrs.

Imaging experiment was also performed for the 10mm thick SUS316L specimen with SCC. Irradiation time was for 3hrs and the beam center of γ ray was located at 5mm distance from the crack. Fig.5 shows the image of SCC in SUS316L. Y-shaped crack was confirmed on the image although the contrast was not so clear. In cases of measurement by optical microscope, the size of crack width near the specimen surface was about 250 μ m. On the other hands, the width near the crack tip was 50~100 μ m.

Moreover, the experiment was carried out for weld joint specimen with SCC. The irradiation time was for 3hrs. Fig.6 shows the image of weld joint specimen. It was confirmed by the figure that the crack was occurred at heat affected zone (HAZ) and propagated toward the specimen depth. It was noted that the crack penetrated into filler metal from HAZ, with its propagating. The crack depth was measured about 13mm.

Conclusions

Imaging measurements by 1.76MeV γ ray were performed for stainless steels which had SCC or artificial slit. Clear slit image was confirmed for stainless steel specimen up to 30mm thick. On the other hands, SCC image was confirmed for 10mm thick specimen although the image was not so clear.

Laser compton scattering gamma ray imaging may be good tool as non-destructive defect detection technique to compare with the result of UT since the defect detection for 10mm thick stainless steel by UT is available.

References

- [1] I.Komura *et al.*, ULTRASONIC TECHNO, Vol.13, No.2 (2001), P10 (in Japanese).
- [2] T.Furukawa *et al.*, Maintenology, Vol.3, No.3

(2004), P10 (in Japanese).

- [3] I.Komura *et al.*, JAPEIC NDE Center Technical Review, Vol.4 (2001), P10 (in Japanese).
- [4] S.Nakahigashi *et al.*, Proc. 2007 Spring Meeting of AESJ (2007), P36 (in Japanese).
- [5] S.Nakahigashi *et al.*, Proc. 2008 Fall Meeting of AESJ (2008), P929 (in Japanese).
- [6] S.Nakahigashi *et al.*, Maintenology, Vol.8 No.3 (2009), P69 (in Japanese).

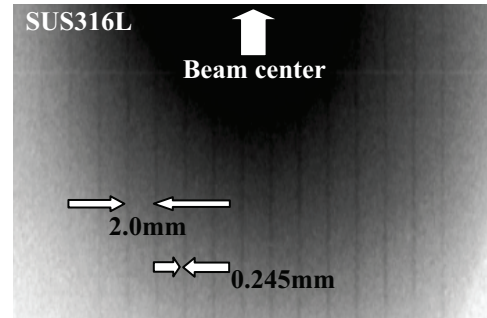


Fig.3 The γ ray image of standard specimen.

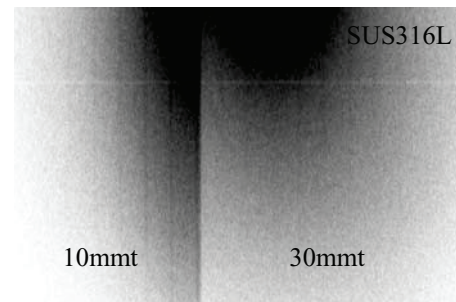


Fig.4 The effect of specimen thickness.

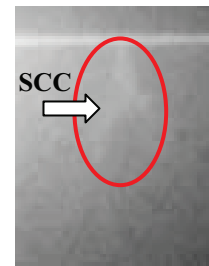


Fig.5 The image of SCC in SUS316L specimen.

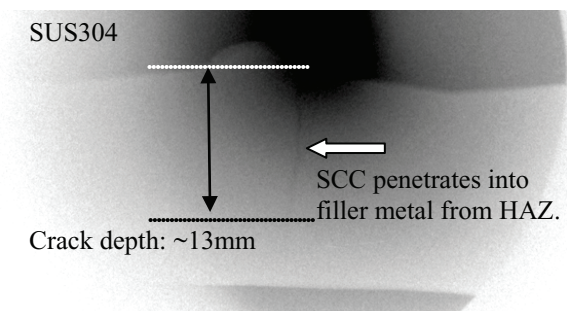


Fig.6 The image of SCC penetrated into filler metal from heat affected zone (HAZ).

Study of $^{12}\text{C}(\gamma,2\alpha)^4\text{He}$ with NewSUBARU laser Compton scattered γ -ray beam

Tatsushi Shima^a, Yasuki Nagai^b, Shuji Miyamoto^c, Sou Amano^c, Ken Horikawa^c,
Takayasu Mochizuki^c, Hiroaki Utsunomiya^d and Hidetoshi Akimune^d

^aResearch Center for Nuclear Physics, Osaka University

^bNuclear Science and Engineering Directorate, Japan Atomic Energy Agency

^cLaboratory of Advance Science and Technology for Industry, The University of Hyogo

^dDepartment of Physics, Konan University

Abstract

The $^{16}\text{O}(\gamma,2\alpha)^4\text{He}$ reaction cross section was measured at the γ -ray energies between 16 MeV and 39 MeV using an active target method and a quasi-monochromatic γ -ray beam provided at the Laboratory of Advanced Science and Technology for Industry (LASTI) of the University of Hyogo. The cross section is found to be rather small in the energy region corresponding to the 2^+ and 4^+ excited states of the intermediate ^8Be nucleus, while it becomes large above the energy corresponding to the ^8Be 1^- state, being in contrast to the latest result reported by Afanas'ev and Khodyachikh. The present result suggests the cross sections are dominated by the contributions of the 1^- states in ^8Be and ^{12}C excited with the E1 transition.

Introduction

The triple-alpha reaction and the $^{12}\text{C}(\alpha,\gamma)^{16}\text{O}$ reaction are considered to play essential roles in the evolution and the nucleosynthesis of the stars in the He-burning phase [1]. It has been discussed that the triple-alpha reaction plays important roles also in various processes such as the He-ignition in Type I X-ray bursts [2] and the break out from the H-burning in the rp-process in neutrino-driven wind [3]. To study those processes in detail, accurate data of the triple-alpha reaction rate are demanded. The cross section of the reaction, however, is hardly measured by a laboratory experiment, because it is a fusion reaction of three alpha-particles, and the reaction rate must be calculated with some reliable theoretical model for the three-alpha system. To develop such a reliable theory, the information about the inverse reaction, i.e., the photodisintegration of ^{12}C is expected to be helpful. For that purpose we made a new measurement of the $^{12}\text{C}(\gamma,2\alpha)^4\text{He}$ reaction cross section with use of an active target and a quasi-monochromatic γ -ray beam. In this contribution the preliminary result is presented.

Experiment

The experiment was performed at the Laboratory of Advanced Science and Technology for Industry (LASTI) at the University of Hyogo. A quasi-monochromatic γ -ray beam in the energy range of between 16 MeV and 39 MeV was generated at the BL01 beam line of the NewSUBARU storage ring in LASTI using the laser Compton-backscattering (LCS) method [4,5]. Figure 1 shows a schematic view of the experimental setup.

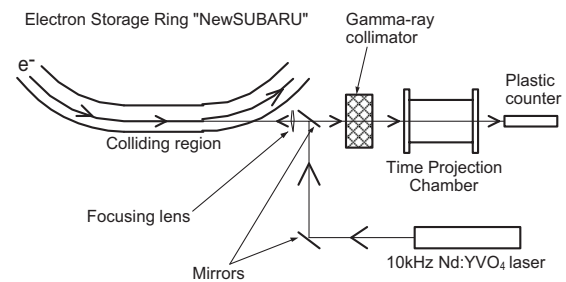


Fig. 1. A schematic drawing of the experimental setup (top view).

The LCS γ -ray was generated by the head-on collision of the electron beam and the laser lights with the wavelengths of 1064nm (fundamental wave) and 532nm (second harmonics) of a Nd:YVO₄ pulse laser. The 180° backscattered γ -ray was extracted by using a collimator made of 10 cm thick lead brick. Using a collimator with the collimation angle of 0.081 mrad, the γ -ray energy spread of 4.5% (FWHM) was achieved.

The intensity of the incident γ -ray was 20000~40000 photons/s, which was measured online by using a plastic scintillation counter whose detection efficiency was calibrated with a BGO counter with the absolute efficiency better than 99%. The energy distribution of the incident γ -rays was determined so as to reproduce the pulse height spectrum measured with a 6'' ϕ \times 5'' NaI(Tl) scintillation counter using its response functions calculated with the EGS5 Monte Carlo code. Fig. 2 shows an example of the γ -ray pulse height spectrum and the intrinsic γ -ray energy distribution.

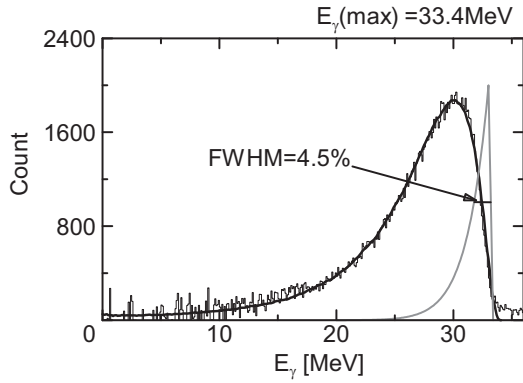


Fig. 2. A typical pulse height spectrum of the LCS g-ray measured with a NaI(Tl) scintillation counter (histogram) and the reproduced pulse height spectrum (black solid curve) assuming the intrinsic distribution (gray solid curve) of the γ -ray energy.

The γ -ray beam was introduced into a time-projection chamber (TPC) which contained a gas mixture of 80% He and 20% CD₄ [6]. The ¹²C nuclei in the CD₄ gas worked as an active target, provided a detection efficiency better than 98.5% and an acceptance of the solid angle of 4π for the ¹²C($\gamma,2\alpha$)⁴He reaction events. The overall sensitivity for the photodisintegration was checked by the simultaneous measurement of the D(γ,p)n reaction, whose cross section has been well known both experimentally and theoretically. As shown in Fig. 3, the present result on the D(γ,p)n reaction cross section is in a good agreement with the existing data [6,7,8,9] as well as a theoretical calculation [10] and the ENDF/B-VII evaluation [11].

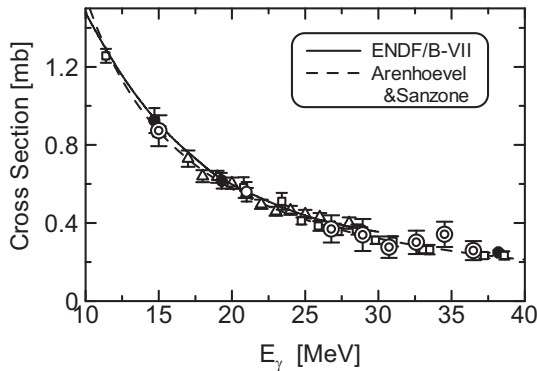


Fig. 3. D(γ,p)n reaction cross section. The open circles and double circles indicate our previous data measured at AIST and the present ones, respectively. The triangles, filled circles, and boxes denote the data from Refs. [7], [8], and [9], respectively. The solid curve and dashed curve are the theoretical calculation with the potential model [10] and the evaluated data [11], respectively.

The ¹²C($\gamma,2\alpha$)⁴He events were identified by requiring the existence of the three tracks of the charged fragments emitted from the γ -ray beam axis and their large energy losses in the TPC gas. Figures 4 and 5 show the examples of the tracks of three α -particles from the ¹²C($\gamma,2\alpha$)⁴He reaction and the major background probably due to the α -decays of the radon isotopes contained in the TPC gas, respectively.

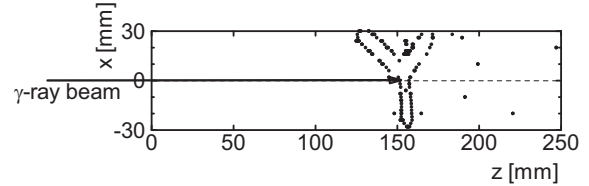


Fig. 4. An example of the tracks of the α -particles from the ¹²C photodisintegration. The box shows the edge of the effective volume of the TPC (side view). The γ -rays are injected from the left.

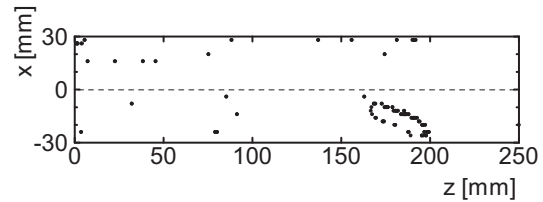


Fig. 5. An example of the track of the background due to the α -decay of a radioactive isotope contained in the TPC gas. It can be easily distinguished from the ¹²C($\gamma,2\alpha$)⁴He events because of the absence of the three tracks originating in the γ -ray beam axis.

¹²C($\gamma,2\alpha$)⁴He cross section

The cross section was obtained from the numbers of the observed ¹²C($\gamma,2\alpha$)⁴He events as a function of the incident γ -ray energy. Figure 6 shows the preliminary result from the present experiment together with the existing data including our previous data measured by using the LCS γ -ray source at the National Institute of Advanced Industrial Science and Technology (AIST). Compared to the latest result [15], the present cross section is significantly smaller in the energy region below ~ 20 MeV where the 2^+ and 4^+ excited states of the intermediate ⁸Be nucleus exist. As shown in Tables 1 and 2, there are few 1^- states below $E_\gamma \sim 20$ MeV in ⁸Be and ¹²C, while many 1^- states with relatively large widths exist above ~ 20 MeV. Therefore the present result suggests the reaction is dominated by the E1 transition to the 1^- excited states of the target ¹²C nucleus and the intermediate ⁸Be nucleus.

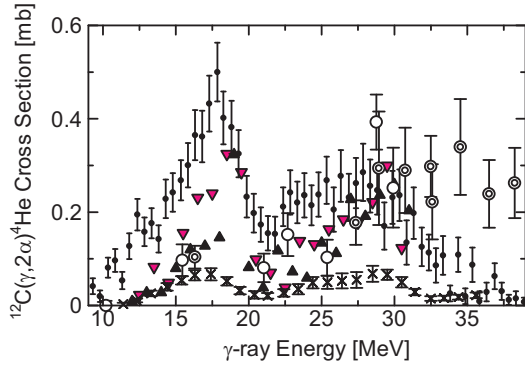


Fig. 6. $^{12}\text{C}(\gamma,2\alpha)^4\text{He}$ reaction cross section. The open circles and double circles indicate our previous data measured at AIST and the present ones, respectively. The filled triangles, gray downward triangles, diagonal crosses, and dots denote the data from Refs. [12], [13], [14] and [15], respectively.

Table 1. Excited states of ^8Be [16]. E_x , J^π and Γ stand for the excitation energy, spin-parity, and the total width of a state.

E_x [MeV]	J^π	Γ [MeV]
0	0^+	5.57×10^{-6}
3.040	2^+	1.5
11.400	4^+	3.5
19.400	1^-	0.65
19.860	4^+	0.7
20.100	2^+	1.1
20.900	4^-	1.6
21.500	3^+	1.0
22.000	1^-	4
24.000	$(1,2)^-$	7

Table 2. Excited states of ^{12}C [17].

E_x [MeV]	J^π	Γ [MeV]
0	0^+	0
4.439	2^+	1.08×10^{-8}
7.654	0^+	8.50×10^{-6}
9.641	3^-	0.034
10.300	(0^+)	3
10.844	1^-	0.315
17.230	1^-	1.15
19.200	(1^-)	~ 1.1
22.650	1^-	3.2
25.400	1^-	2
27.000	(1^-)	1.4
28.200	1^-	1.6

On the other hand, a large strength was observed in the energy region above 29 MeV where a lot of excited states with unknown J^π exist. It will be important for better understanding of the mechanism of the $^{12}\text{C}(\gamma,2\alpha)^4\text{He}$ reaction to determine J^π of those excited states

experimentally. The spin and parity of each excited state are to be determined from the angular distribution and analyzing power at the relevant excitation energy, and the LCS γ -ray will be a promising tool for such measurements because of its nice features such as a very high polarization, a small energy spread and a small angular spread.

Summary and Discussion

The $^{12}\text{C}(\gamma,2\alpha)^4\text{He}$ reaction cross section was measured by means of a quasi-monochromatic γ -ray beam for the first time. Using an active target technique, the absolute cross section was determined with high accuracy, and it will be useful to develop a reliable theoretical method to calculate the triple-alpha fusion reaction.

Acknowledgment

This work was supported in part by Grant-in-Aid for Specially Promoted Research of the Japan Ministry of Education, Science, Sports and Culture and in part by Grant-in-Aid for Scientific Research of the Japan.

References

- [1] A.Bcdefg *et al.*, J. Lasti Rev., **34**,2, pp.1234-1244 (2000).
- [1] E.E. Salpeter, ApJ **115**, 326 (1952); F. Hoyle, ApJ Supp. **1**, 121 (1954).
- [2] K. Nomoto, F.-K. Thielemann, and S. Miyaji, A&A **149**, 239 (1985); F.-K. Thielemann *et al.*, Prog. Par. Nucl. Phys. **46**, 5 (2001).
- [3] S. Wanajo, ApJ **647**, 1323 (2006).
- [4] K. Aoki *et al.*, Nucl. Instr. Meth. in Phys. Res. A **516**, 228 (2004).
- [5] S. Miyamoto *et al.*, Radiation Meas. **41**, S179-S185 (2006).
- [6] T. Kii, T. Shima, T. Baba, and Y. Nagai, Nucl. Instr. Meth. in Phys. Res. A **552**, 329 (2005).
- [7] D.M. Skopik *et al.*, Phys. Rev. C **9**, 531 (1974).
- [8] R. Bernabei *et al.*, PRL **57**, 1542 (1986).
- [9] C. Dupon *et al.*, Nucl. Phys. A **445**, 13 (1985).
- [10] H. Arenhövel and M. Sanzone, Few-Body Systems Suppl. **3**: *Photodisintegration of the Deuteron* (Springer-Verlag, Wien,1991).
- [11] ENDF/B-VII data file for ^1H (MAT=125). 2006, evaluated by G.M. Hale.
- [12] V.N. Maikov, Zh. ekper. teor. Fiz. **34**, 1406 (1958) (Soviet Physics-JETP **7**, 973 (1958)).
- [13] A. Murakami, J. Phys. Soc. Japan **28**, 1 (2008).
- [14] E.A. Kotikov *et al.*, Izv. Ross. Akad. Nauk, Ser. Fiz. **66**, 445 (2002).
- [15] S.N. Afanas'ev and A.F. Khodyachikh, Phys. Atomic Nuclei **71**, 1827 (2008).
- [16] ENDSF file for ^8Be , edited by J.H. Kelley, J.L. Godwin, C.G. Sheu, *et al.*, 2004.
- [17] ENDSF file for ^{12}C , edited by F. Ajzenberg-Selove and J.H. Kelley, Nucl. Phys. A **506**, 1 (1990).

Laser-plasma debris from a rotating cryogenic–solid-Xe target

S.Amano, Y.Inaoka, H.Hiraish, S.Miyamoto, T.Mochizuki
LASTI/UH

Abstract

We investigate the characteristics of laser plasma debris that is responsible for damaging optics. The debris is composed of fast ions, neutral particles, and fragments, and originates from a solid Xe target on a rotating drum that we developed as an extreme ultraviolet (EUV) source. The ice fragments appear to be a problem most notably with solid Xe targets; however, we find that the damage induced by Xe ice fragments can be avoided by simply reducing the laser pulse energy. We find the number of fast neutral particles to be an order of magnitude less than the number of ions, and we clarify that the plasma debris is primarily composed of fast ions. In addition, we find that the number of fast ions having a few dozen keV's of energy decreases when using the rotating target compared with the rest target. We attribute this to a gas curtain effect from the Xe gas localized at the rotating target surface. We estimate the sputtering rate of the Mo/Si mirror, which is caused primarily by the fast ions, to be 104 nm/1 M shots at 190 mm from the source plasma and at an 11.25° angle from the incident laser beam. Up to the 1M shots exposure, remarkable degradation of the mirror reflectivity is not observed though the sputtering damages the mirror. Mitigation of the ions by using gas and/or magnetic fields will further improve the mirror lifetime. By comparing with a liquid jet Xe target, we conclude that the sputtering rate per conversion efficiency when using the solid Xe targets on the rotating drum is the same as that when using the liquid Xe targets. The high conversion efficiency of 0.9% in the rotating drum solid Xe target makes this technique useful for developing laser plasma EUV sources.

Introduction

Laser plasma radiation from high density, high temperature plasma constitutes an attractive, high brightness point source for producing EUV to x-ray radiation. It is achieved by illuminating a target with high-peak-power laser irradiation.

We originally developed a fast rotating cryogenic drum system, which can continuously supply a solid Xe target. Using the drum system, a maximum CE of 0.9% was demonstrated at 13.5 nm and with the 2% bandwidth required for an EUVL source. The source operated continuously with an output power of 1W.

We investigated the plasma debris from the drum target system, that is responsible for damaging optics. The debris consists of fast ions, fast neutrals, and ice fragments. In this article, we report in detail the characteristics of the debris and discuss the damage it causes on a Mo/Si mirror.

Experiments

Figure 1 shows the experimental setup used to obtain data on the characteristics of the plasma debris from a cryogenic solid Xe target on a rotating drum. Initially, data characteristic of fast ions, neutrals, and fragments, which were thought to be main elements of plasma debris, were obtained in single-shot laser experiments using a conventional Nd:YAG rod laser with a wavelength of 1064 nm and a 10 ns pulse width. By adjusting the focal lens position, laser

intensity on the target was optimized to be $\sim 1 \times 10^{10}$ W/cm² to maximize the EUV radiation around 13.5nm.

Ions from the plasma were detected using a charge collector (CC) with an applied bias voltage of -100 V, and their kinetic energies were estimated from time of flight (TOF) signals. The CC was fixed 190 mm from the plasma and at a 22.5° angle with respect to the incident laser beam.

We used a double micro-channel plate (MCP) (Hamamatsu, F4655-10) to detect neutral particles, after an electrical field repelled the ions. We positioned the MCP at 45° with respect to the laser beam, and mounted it inside a small vacuum chamber that was connected via a vacuum tube to the main vacuum chamber. The tube included a pair of electrodes and a 0.75 mm diameter pinhole. The pinhole allowed us to differentially pump the MCP chamber and keep the vacuum pressure below 10⁻⁴ Pa. The distance from the plasma target point to the MCP was 1050 mm.

To observe damages by fragment impact, we placed a Si substrate 100 mm from the plasma target point and at a 22.5° angle with respect to the incident laser beam.

Next, we conducted multi-shot laser experiments to study mirror damage caused by the total plasma debris (ions, neutrals, and fragments) using a high-repetition-rate Nd:YAG pulsed slab laser developed in-house. The slab laser was configured to generate 1064 nm pulses with pulse widths of 20 ns at a repetition rate of 320 Hz. In

the experiments, a Mo/Si mirror sample and a gold-coated quartz crystal microbalance (QCM) sensor (Sigma, SQM-160) were placed 100 mm from the plasma at 22.5° and 45° angles, respectively, to measure total erosion rates upon extended multi-shot plasma operation.

EUV energy from the plasma was also monitored by an EUV energy monitor placed 190 mm from the plasma at an 11.25° angle with respect to the incident laser beam. The energy monitor consisted of an X-ray diode with a Mo/Si filter (IRD, AXUV-20) and a Mo/Si mirror to select the wavelength band around 13.5 nm. Mirror damage leading to reduced reflectivity is detected by monitoring the decrease in EUV energy during multi-shot laser operation.

Results

Being an inert gas at room temperature, Xe is deposition-free compared with other metal targets. However, damage to mirror surfaces occurs due to sputtering. In particular, damage by Xe ice fragments was considered problematic for solid Xe targets. We find, however, that this damage can be avoided simply by reducing the laser pulse energy. We find that the number of fast neutral particles is approximately an order of magnitude less than the number of ions, and we demonstrate that the major plasma debris component is fast ions. We also find that the number of the fast ions having a few dozen keV's of energy decreases when using the rotating target compared to that observed when using the stationary target. We attribute this to the gas curtain effect of Xe gas localized on the rotating target surface.

The sputtering of the Mo/Si mirror is mainly caused by fast ions, and the sputtering rate is estimated to be 104 nm/1 M shots with the mirror 190 mm from the plasma at 11.25° from the incident laser beam. If a Mo/Si multilayer mirror having more than 40 layers pairs is used, the degradation of its reflectivity under such conditions will be kept under 10% for an exposure of up to 1M shots.

The major plasma debris component is ions, and we believe its mitigation to be comparatively simple. To reduce the debris and improve the mirror lifetime, we are now developing ion-mitigation techniques that involve using gas.

The measured sputtering rate per CE at 51° from the incident laser beam is essentially equal to that obtained when using the liquid Xe jet. Assuming that the debris distribution for both solid and liquid targets is identical, we conclude that the sputtering rate per CE for solid Xe rotating targets is the same as for liquid Xe targets. Considering the higher efficiency (0.9%) obtained using a solid Xe rotating target compared with a liquid Xe jet target (0.3%), we conclude that a solid Xe rotating target is advantageous for laser plasma EUV sources.

References

- [1] S.Amano *et al.*, Rev. Sci. Instrum., **81**,023104 (2010).

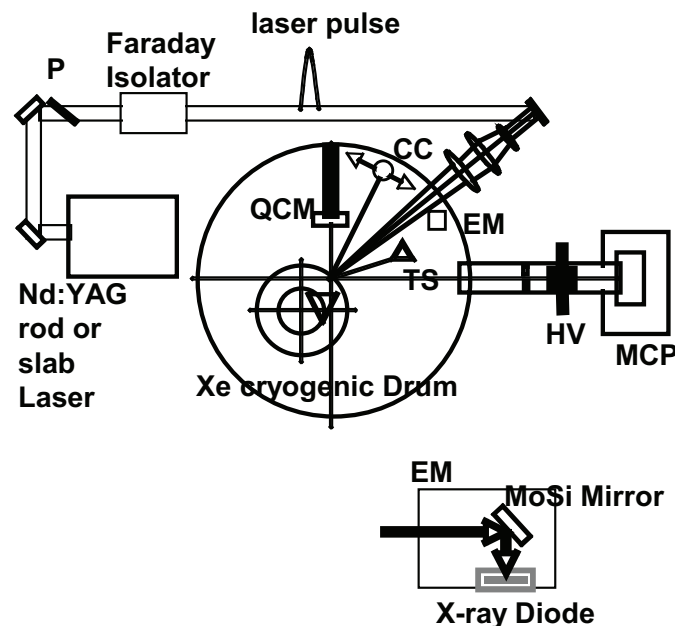


Fig.1 Experimental setup.

Mitigation by argon buffer gas of fast debris from cryogenic xenon laser plasma EUV light source

T. Sekioka¹, S. Amano², T. Inoue², and T. Mochizuki²
¹Graduate School of Engineering, University of Hyogo,
²LASTI, University of Hyogo

Abstract

One of the serious problems in the laser-produced plasma for an extreme ultraviolet (EUV) light source used for the next generation lithography is the generation of fast ions that damage the EUV collector optics. Gas curtain method is regarded as one of the most efficient methods for mitigation of fast debris without serious loss of EUV light. We have investigated the mitigation of fast ions from laser-produced xenon plasma on the rotating drum xenon cryogenic target by argon gas curtain. Energy spectra of fast Xe^+ , Xe^{2+} , Xe^{3+} ions from the xenon plasma were obtained at back ground pressure of 4×10^{-4} Pa, before argon gas was introduced into the chamber. Argon gas flow rate was increased by 100 ml/min step to the extent of 800 ml/min. We have obtained the pressure dependence of the energy spectra of xenon ions for each charge state. These data on the attenuation of xenon ions by argon buffer gas are indispensable for designing a gas curtain debris mitigation system.

Introduction

An extreme ultraviolet (EUV) light source is under development for use in EUV lithography. However, in general, these targets emit particle debris that produce mechanical damage and/or deposition on the mirrors degrading their reflectivity in a short period. Mirror cleaning will become a serious problem. In this study, we investigated the mitigation by argon gas curtain of the fast xenon ions from the cryogenic xenon target.

Experiments and results

A schematic diagram of the experimental setup is shown in Fig. 1. A xenon cryogenic target on the rotating drum^[1] was irradiated in a target chamber by a pulsed 1.06 μm Nd:YAG slab laser^[2] with a energy of 0.3 J at incident normal. The back ground pressure inside the target chamber was 4×10^{-4} Pa. Fast ions were measured with a Thomson parabola (TP) ion analyzer which was set at an angle of 45° with respect to the laser axis. The fast ions were collimated with double pinholes of 0.3mm in diameter, and travel on species-dependent trajectories determined by electric and magnetic deflections and then impinge upon the micro channel plate (MCP). Both the magnetic field and electric field were applied between 1-cm-thick and 5-cm-length space. Figure 2 shows the luminescent image of the fluorescent screen which was set at the output of the MCP, from a single laser shot. Thomson parabolas of Xe^+ , Xe^{2+} and Xe^{3+} were confirmed.

Argon gas was introduced into the target chamber, and the argon gas flow rate was increased by 100 ml/min step. For each argon gas flow rate, we obtained the energy spectra of xenon ions resolving their charge state.

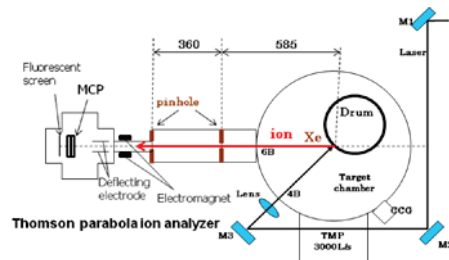


Fig.1. Experimental setup.

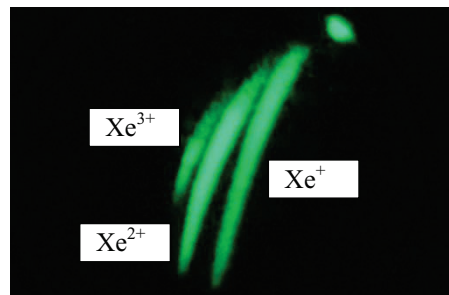


Fig.2. A typical image of Thomson parabola ion analyzer.

Figs.3, 4 and 5 show the energy spectra of Xe^+ , Xe^{2+} and Xe^{3+} at several argon gas flow rates. The response of MCP for ions was not considered in the analysis. Above argon gas flow rate of 500 ml/min, only Xe^+ ions could be observed. Above 800 ml/min, where the argon partial pressure was 0.56 Pa, the Xe^+ ions intensity was so weak that they were buried in the back ground.

Data analysis is on the progress for determining the argon column density that is required to stop the fast xenon ions to the level where no sputtering occurs without serious loss of X-ray^[3].

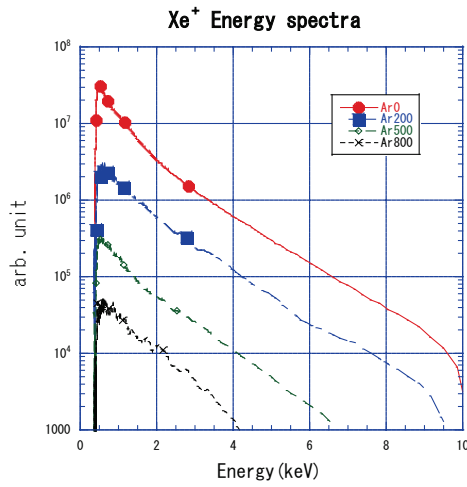


Fig.3. Energy spectra of fast Xe^+ debris ions at several argon gas flow rates. The flow rates are 0, 200, 500 and 800 ml/min.

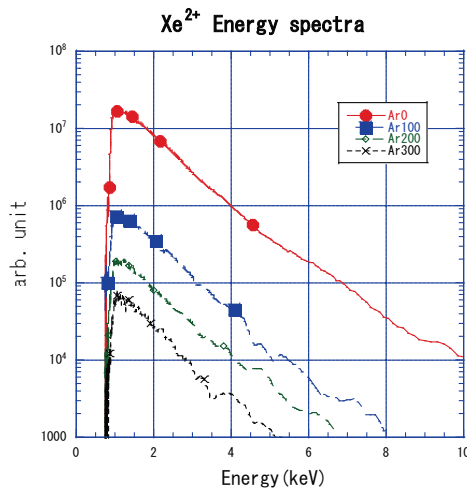


Fig.4. Energy spectra of fast Xe^{2+} debris ions at several argon gas flow rates. The flow rates are 0, 100, 200 and 300 ml/min.

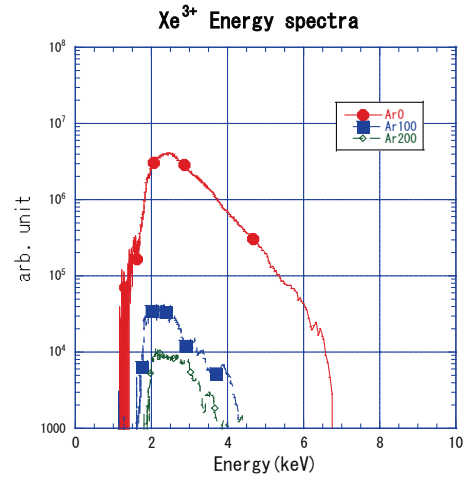


Fig.5. Energy spectra of fast Xe^{3+} debris ions at several argon gas flow rates. The flow rates are 0, 100 and 200 ml/min.

References

- [1] K.Fukugaki *et al.*, Rev. Sci. Instrum. **77**, 063114 (2006)
- [2] S.Amano *et al.*, Rev. of Laser Engineering, Vol. 29, pp.679-682 (2001)
- [3] T.Inoue *et al.*, Lasti Annual Report, Vol.10, pp27-28 (2008)

Mitigation effect of plasma debris from cryogenic xenon target by argon jet

T. Inoue, S. Amano, T. Mochizuki
University of Hyogo LASTI

Abstract

In order to mitigate the sputtering effect on collection mirror which was caused by xenon fast debris, the mitigation effect of plasma debris from the rotating drum xenon cryogenic target by an argon gas jet and its absorption for soft X-ray from the plasma were investigated. The sputtering by xenon debris was mitigated to be 1/50 when the argon gas flow was 0.75L/min. The measurement of ion debris showed that a decrease in the energy of the colliding particle contributed to the mitigation than a decrease of the number of collision particles. In addition, the attenuation of soft X-rays was found to be 10% or less as well as a buffer method.

Introduction

X-ray source generated from laser produced xenon plasma has a broad-band spectrum, and it would become a compact and high efficiency soft X-ray source. We achieved a generation of the soft X-ray (5-17nm) of $20\text{W}/2\pi\text{Sr}$ by using a rotating drum xenon cryogenic target^[1] and a 100W/320pps Nd:YAG slab laser system^[2]. Furthermore a focusing of soft X-ray, which improved its intensity by 27-times ($1.26\text{mJ}/\text{cm}^2 @ 1\text{mm}\Phi$) compared with that without focusing^[3] was accomplished by using a cylindrical ruthenium mirror system under the single laser pulse operation. However to use this mirror system at the operation condition of 100W/320pps, the mirror sputtering effect by xenon plasma debris must be mitigated because it causes a deterioration of the mirror reflectivity. We used an argon buffer gas which had a low absorption ratio of soft X-ray from xenon plasma and was able to mitigate the sputtering. The sputtering caused by the xenon debris was able to be mitigated to 1/18 on the condition of the argon gas of 8Pa filled thoroughly in the chamber.

In this paper, we report on a mitigation effect of plasma debris from xenon cryogenic target by an argon jet which can be increased the gas density locally.

Experiments and Results

The experiment arrangement is shown in Fig.1. Nd:YAG Slab laser was used, and the laser pulse was focused on a rotating drum xenon cryogenic target at incident normal. The laser energy was 0.3 J with a pulse duration of 20 ns at 160pps or single pulse operation. The position of focus lens was $LP=5\text{mm}$ where the conversion efficiency maximized. The rotating drum was operated at 130rpm and its vertical movement velocity was 3mm/s at 30mm width. A thickness of xenon layer was adjusted about $500\mu\text{m}$ by two wipers inside the drum cover and fresh surfaces were supplied in each shot. An argon buffer gas was supplied by using a nozzle with a inside diameter of $0.75\text{mm}\Phi$ near the source. A SUS wall with a thickness of $400\mu\text{m}$ and

10mm width was placed in front of the nozzle to increase the argon density of that position. In order to evaluate a debris mitigation effect by the argon jet, we measured a sputtering rate in a gold film coated on a Quartz Crystal Micro-balance (QCM) which was mounted at 45 degree and a distance of 73 mm from a light source point. The soft X-ray energy was measured by an X-ray calorimeter at 45 degree and a distance of 190mm from the source. The ion debris was measured by a charge collector at 45 degree and a distance of 73mm.

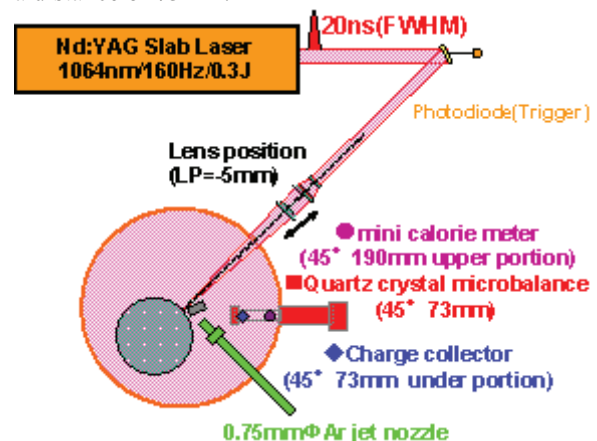


Fig.1 Experimental Setup

Fig.2 shows the result of measurements by QCM. The sputtering by xenon debris was mitigated to be 1/50 when the argon gas flow was 0.75L/min. At this time, the wave of charge collector signal shown Fig.3 was delayed and increased the width of the time. However the integer of the charge collector signal that means the number of ions was not so decrease. These results suggest that a decrease in the energy of the colliding particle mainly contributed to the mitigation rather than a decrease of the number of ions. In addition, the attenuation of soft X-rays was 10% or less as well as a buffer method. It is proven that the jet method effectively mitigates the plasma debris. If the attenuation up to 10% can be allowed, the debris mitigation of about 1/500 will be achieved.

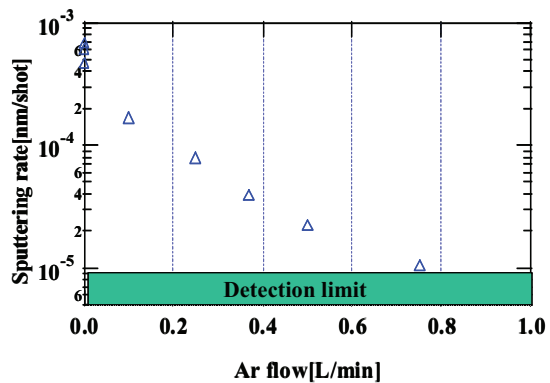


Fig.2 the mitigation effect of gold film sputtering rate as a function of argon flow.

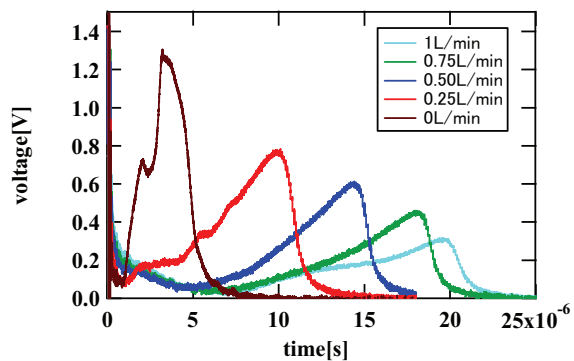


Fig.3 ion signal measured by charge collector

References

- [1] K.Fukugaki *et al* , Rev. Sci. Instrum. **77**, 063114 (2006)
- [2] S.Amano *et al* , Rev. of Laser Engineering, Vol.**29**, pp.679-682 (2001)
- [3] T.Inoue *et al* , Lasti annual report vol.**10** p27-28(2008)

Propose of Three-dimensional Micro Fluidics Device Using Centrifugal Force

Yuichi Utsumi*, Tsukasa Azeta*, Yoshiaki Ukita**and Saki Kondo*

*Laboratory of Advanced Science and Technology for Industry, University of Hyogo, Japan

**School of Materials Science, Japan Advanced Institute of Science and Technology, Japan

Abstract

Lab-on-a-CD enables automation of chemical operations for overall assay protocol [1, 2], however there is strong restriction to the lab-on-a-CD, due to limited area for integration of multiple and multiple reactor units and different modules. This paper reports a new concept of lob-on-a-CD with three-dimensional (3D) microchannel interconnection, which enables fast, high-sensitive and high-throughput analysis.

Introduction

There have been paid much attention to the lab-on-a-CD for the use of enzyme-linked immunosorbent assay (ELISA), due to its convenience for the automation of multiple microreactors. However it is difficult to simultaneously realize the performance and integration of multiple reactor units due to the limited chip area. One of the biggest problem arise from the limitation is inadequate sensitivity due to shortage of surface area for the immobilization of antibody. To resolve these problems, we propose a new type lab-on-a-CD concept based on three-dimensional (3D) microchannel network.

The important contributions of the 3D structure are summarized in two types of benefits as listed in below.

1. As shown in fig.1, stack concept of lab-on-a-CD contributes to the large-scale integration of various modules and reactor systems by stacking various layers of disks with different functions. Seven multiple reservoirs with different functions are integrated and connected each other with 3D microchannel network. It is notable that we succeeded in to increase the density of integrated microreactor unites by utilizing three-dimensionally stacked layers.
2. Flexibility of structural design, arises from 3D microstructure, enhances of performance of various modules. For example our device has 3D scaffolds for the immobilization of antibody onto the surface [3], and stacked structure of 3D detection reservoir resulting in the increase of signal-to-noise ratio as shown in fig. 2.

To realize the concept, the most important key-technology is a controlling of “vertical” liquid transportation which enables transfer of reagents between different layers of the stacked CD.

To investigate the feasibility of the valving and liquid transportation by centrifugal force, computational fluid dynamics (CFD) using “FLUENT” software is carried out. We assumed the

driving force arisen from spinning speed from 0 rpm to 2000 rpm. As shown in fig. 3(a), the liquid is held by surface tension with spinning speed less than 1000rpm and it becomes transported through capillary bundle structure with spinning speed greater than 1000rpm. The results suggest possibility of vertical liquid transportation through vertical capillary bundle structure by converting the planar centrifugal driving force into isotropic pressure to drive the liquid in vertical direction.

Experiments and Results

The poly-dimethylsiloxane (PDMS) disks with planer microchannels are fabricated by conventional rapid prototyping and poly-methylmethachrylate (PMMA) disks are fabricated by deep X-ray lithography as shown in fig. 4[3]. To construct 3D microchannel network, these disks are aligned and reversibly bonded.

To demonstrate the automatic sequencing in 3D CD platform, we loaded pure water and stained into the reservoirs and CD platform is spun for the sequencing. The burst frequency and flow behaviors are measured and observed by using strobe scope system. The four step flow sequencing involving vertical liquid flow around reaction reservoir are successfully demonstrated. As shown fig. 5, the reproducibility is indeed good between 8 individual measurements.

Achieved flow sequencing driven by controlled centrifugal force in 3D fluidic interconnection is expected to realize high-efficiency and high-throughput total assay on one platform.

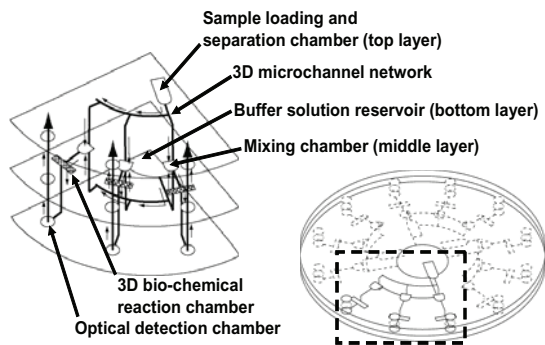


Figure 1. Schematic diagram of new CD-like microfluidic platform with three-dimensional fluid network

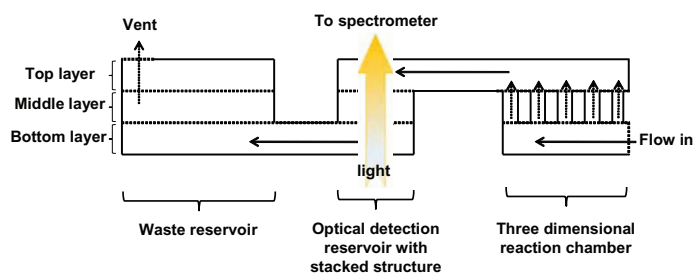


Figure 2. Cross sectional view of three-dimensional microchannel interconnection

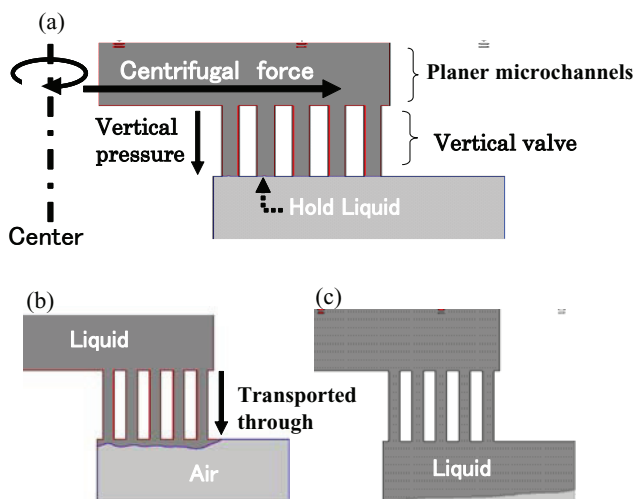


Figure 3. Analysis model of three-dimensional structure by centrifugal force.
 (a) Liquid is held by surface tension. [500rpm]
 (b), (c) Centrifugal force was over surface tension [over 1000rpm].



Figure 4. Photographs of designed and fabricated CD platform consist of three layers

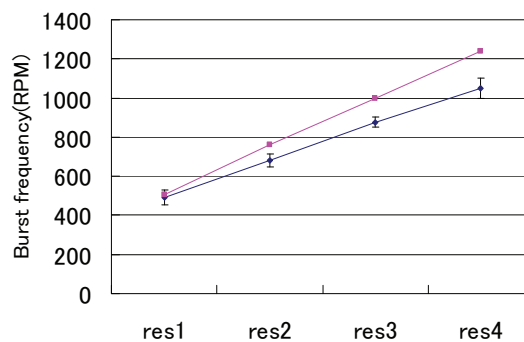


Figure 5. (a) Images of flow sequencing of water
 (b) Measured burst frequency

REFERENCES:

- "Design of a Compact Disk-like Platform for Enzyme-Linked Immunosorbent Assay," S. Lai, S. Wang, J. Luo, L. J. Lee, S. T. Yang, and M. J. Madou, *Analytical Chemistry*, **76**, 1832 (2004)
- "A fully automated immunoassay from whole blood on a disk" B. S. Lee *et al.*, *Lab Chip*, **9**, 1548, (2009)
- " Proposal of a new microreactor for vertical chemical operation," Y. Utsumi, T. Asana, and Y. Ukita, *Japanese Journal of Applied Physics*, **45**, 2606 (2006).

Fabrication of electrodes for multiplex neural interface

Mitsuhiro Yoshida*, Yoshiaki Ukita*, Kunihiro Mabuchi**, Yuichi Utsumi

*Laboratory of Advanced Science and Technology for Industry, University of Hyogo

**Dept. of Information physics & Computing, Grad. School of Info. Sci. & Tech. The University of Tokyo

Abstract

“Microneurography” developed by Karl-Erik Hagbarth and Ake B. Vallbo, is a technique for reading and manipulating nerve signals by tools, acting as “nerve signal interfaces”^[1]. The “flexible regeneration type nerve electrode” is an interface device for nerves, connecting nerve fibers to signal conducting lines on a macro structure, making it usable for “Microneurography”^[2]. Our chips buildup is based on multiple stacked SU-8-layers.

Introduction

Information on the neural system is expressed by the action potential transmitted in the neuronal cell. This neural coding can be measured by mounting the electrode in the neighborhood of the neuronal cell or the neuronal cell. More, it is also possible to stimulate the neuronal cell oppositely, and to generate the neural coding. Such an electrode is called a nerve electrode. It becomes possible to analyze the function of the neural system by measuring the neural coding. And, a multi activity of a cell simultaneous metrology that records the activity of two or more neuronal cells at the same time is paid to attention. There is a nerve regeneration type electrode using the ability of regeneration for the peripheral nerve to make the action potential transmitted in the neuronal cell a multi channel. The model of the nerve regeneration electrode is shown Fig.1 Flexible regeneration type nerve electrode relies on the regeneration ability of nerves. By putting a pair of cut nerves at both ends of a capillary, they grow through the capillary to reconnect. When an electrode is embedded inside of the capillary, it become possible to detect the potential of nerves by the electrode. This method is suitable to detect signals inside and outside of the nerve fiber. The development of implantable neural interface will realize brain-driven prosthetic limb and the artificial organ, or its also possible to apply to scientific application such as understanding of biological functions of nerves.

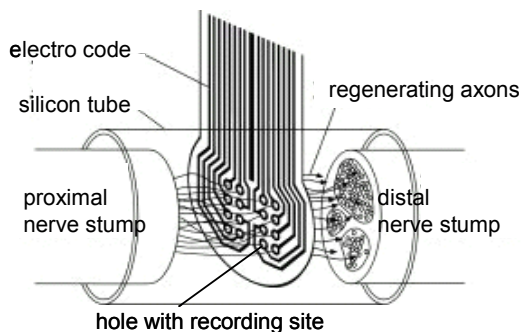


Fig.1 Model of nerve reproduction electrode

Design

Fig.2 (a) shows the outline of the nerve regeneration electrode. To increase the number of electrodes we propose stacked type electrode structure. It is difficult to integrate many electrodes by using single layer due to small area. Thus the electrode shape is designed to be stacked allowing three-dimensional (3D) crossing of multiple electrode lines. For the first attempt, designed electrode structures have 12 channels electrode on a single layer and total 24 channels are realized by stacking two layers. Fig.2 (b) shows the designed nerve reproduction electrodes.

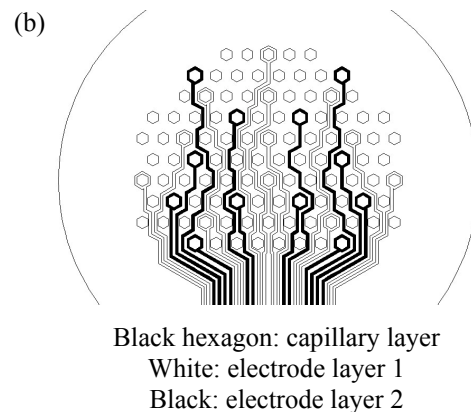
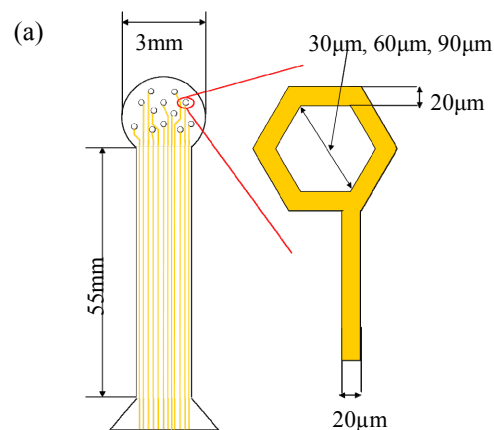


Fig.2 (a) Outline of electrode

(b) Designed nerve reproduction electrodes

Experiments

Our chips buildup is based on multiple stacked SU-8-layers. The prepared single layer electrode chips are piled up together with the precise alignment and bonding process. Fig.3 shows the fabrication process image of bonding. For the bonding process the unique characteristic of SU-8 is utilized for the patterning of capillaries and bonding^[3].

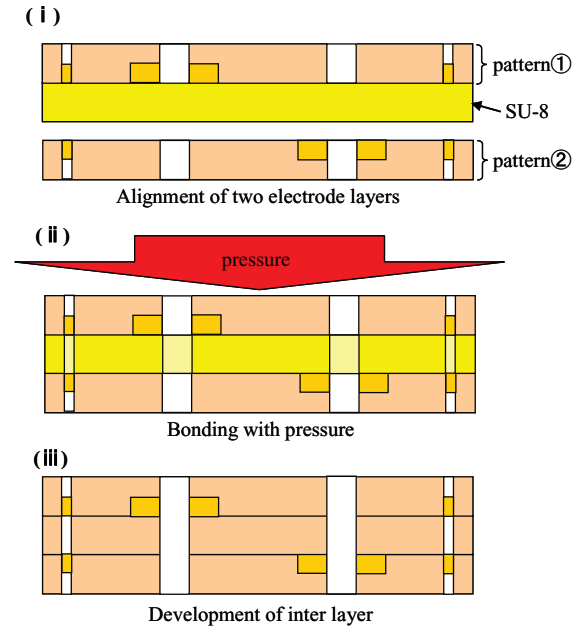


Fig.3 Fabrication process image of bonding

Results

Fig.4(a) shows photographs of outer view fabricated electrodes. Fig.4(b) shows photographs of zoom up of structure of electrodes. As shown in Fig.4(b) the three-dimensionally stacked electrodes and through capillary for nerve growth are successfully aligned and patterned in monolithic SU-8 chip. We inspected the method to manufacture it for three-dimensions to realize the multi channel of the flexible regeneration type nerve electrode in this study and demonstrated that it was possible for the first time. We will aim at the optimization of the structure parameter and the multistage of the stacking step and the advancement of the fabrication process in future. Moreover, it is necessary to verify it by measuring an actual neural coding by mounting.

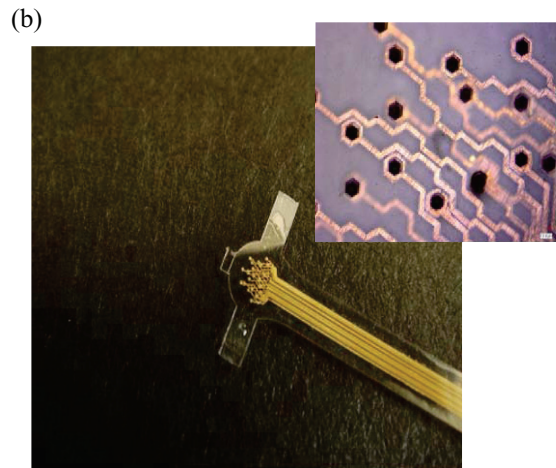
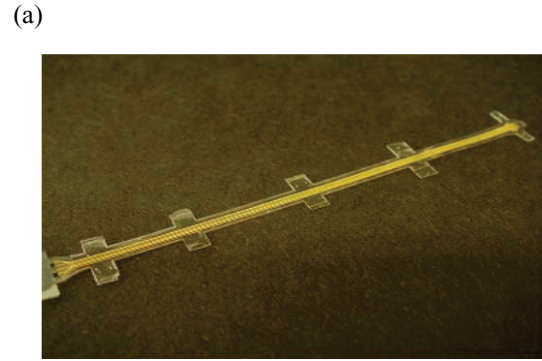


Fig.4 (a) Outer view fabrication electrodes
(b) Zoom up of structure of electrodes

References

- [1] Åke B. Vallbo, Karl-Erik Hagbarth, and B. Gunnar Wallin : “Microneurography: how the technique developed and its role in the investigation of the sympathetic nervous system”, *J Apply Physiol* 96, p.1262-1269 (2004)
- [2] Takafumi Suzuki, Takashi Saito, Kunihiko Mabuchi : “Development of a multi-channel nerve electrode for peripheral nervous system”, *Technical report of IEICE, Vol. 100, No. 479 pp.63 -66 (2000)*
- [3] F J Blanco, M Agirregabiria, J Garcia, J Berganzo, M Tijero, M T Arroyo, I Aramburu and Kepa Mayora : “Novel three-dimensional embedded SU-8 microchannels fabricated using a low temperature full wafer adhesive bonding”, *J.Micromech..Microeng*, Vol. 14, pp.1047 -1056 (2004)

HIGH EFFICIENCY MICROFLUIDIC REACTOR CHIP OPERATED ONLY USING SURFACE-ACOUSTIC-WAVE

Takeshi Komoto*, Tsunemasa Saiki***, and Yuichi Utsumi*

*Laboratory of Advanced Science and Technology for Industry, University of Hyogo, Japan

** Hyogo Prefectural Institute of Technology, JAPAN

Abstract

Surface acoustic wave (SAW) devices are expected for micro total analysis systems, because their structures are simple. We studied flow actuators driven by SAWs. We then fabricated a micro-mixer driven by the SAWs. In this study, on the basis of the mixer and the flow actuator, we proposed and fabricated a novel micro-reactor driven by the SAWs, and investigated its reaction property. As a result, we found that the local rapid mixing of micro solutions was possible by using the SAWs, and high availability of our micro reactor was demonstrated.

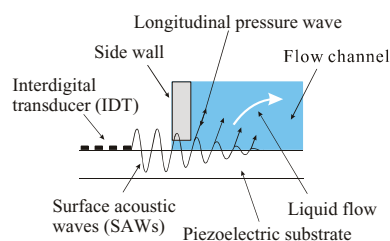
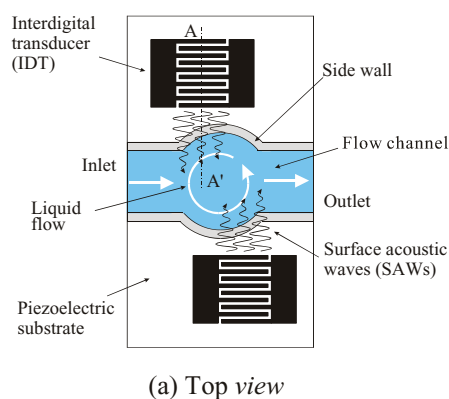
Introduction

The manufacturing process for each component device in a lab on a chip must be simplified to integrate multiple functional devices. Surface acoustic wave (SAW) devices with very simple structures have attracted attention. Therefore, we studied SAW actuators that could enable a continuous liquid to flow with high efficiency [1] and enable a small amount of liquid to be rotated at high revolution [2]. The knowledge obtained from our previous research enabled us to fabricate a high efficiency microfluidic mixing chip [3]. In this study, we evaluated the chemical reactivity of the chip.

Structure of our reactor

The top view and magnified sectional view of our micro reactor operated using SAWs are shown in Figure 1 (a) and (b). SAWs are generated from the IDTs when high frequency voltage is applied to interdigital transducers (IDTs). The SAWs propagate in the surface layer of the substrate and pass through a sidewall to the bottom plate of the flow channel. The liquid in the flow channel then becomes energized due to longitudinal pressure wave radiation from the SAWs and flows in the propagated direction of the SAWs. Overall, the liquid in the reactor flows with some rotation in a stream from the inlet to the outlet through external pumps.

A photograph of a microfluidic reactor (mixing) chip operated using SAWs is shown in Figure 2. The chip consists of one y-type flow channel, three reservoirs, one reactor, and two pumps. Not only the micro reactor but also the pumps were driven in the microfluidic chip using SAWs. The flow channel widths upstream and downstream of the merging point were 0.5 mm and 1 mm. The depth of the flow channel was approximately 250 μm . The IDTs of the reactor and the pumps had pitches of 200 μm , 20 pairs, and apertures of 0.5 mm.



(b) Magnified sectional view (A-A')

Figure 1. Overview of micro reactor operated using SAWs.

Experiments

Our experimental setup for investigating the reaction characteristic of the microfluidic chip is shown in Figure 3. Before starting the experiment, we filled reservoir 1 with solution A, which was a mixture of 10% NaOH water solution of 15 μL and 0.075 mg of luminol reagent, and filled reservoir 2 with solution B, which was a mixture of 7.5 vol% H_2O_2 water solution of 15 μL and 0.45 mg of potassium ferricyanide. In the experiment, these solutions flowed through the two pumps, which operated simultaneously. We then took photographs of the liquid behavior in the reaction area using a highly sensitive camera.

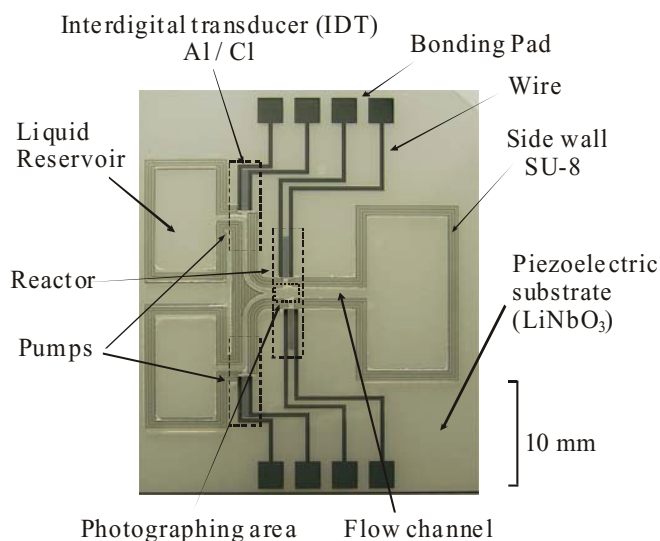


Figure 2. Photograph of microfluidic reactor chip operated using SAWs.

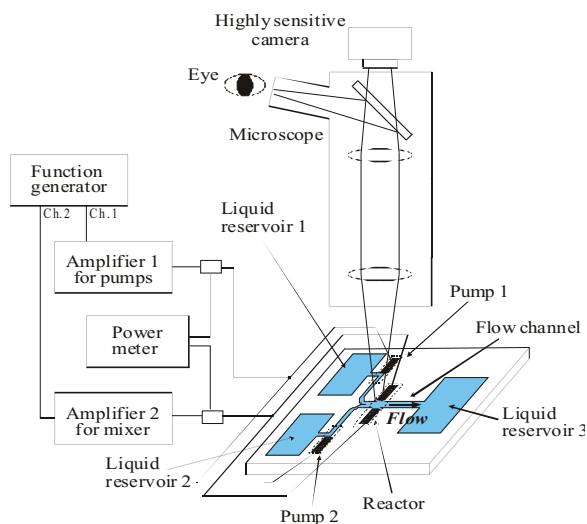
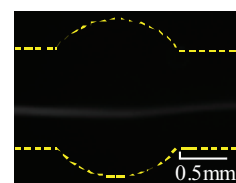


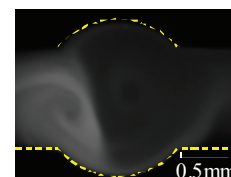
Figure 3. Experimental setup.

Results

The photographs of luminol luminescence in the reaction area are shown in Figure 4. Here, the flow velocities in the channels were about 5 mm/sec, and driving power P_R of the micro reactor was 250 mW. When the micro reactor did not operate, only one line of luminescence was observable near the center of the flow channel. However, when the micro reactor did operate, luminescence occurred in the whole flow channel. These observations demonstrated that local and rapid mixing of these solutions was possible by using the SAWs. Moreover, our micro reactor demonstrated high applicability.



(a) Non-operation of reactor (PR=0mW)



(b) Operation of reactor (PR=250mW)

Figure 4. Photographs of luminescences with luminol reactions.

REFERENCES:

1. "Proposal of a Novel Continuous Flow Pumping Operated by Surface Acoustic Wave," Y. Utsumi, T. Saiki, K. Okada, 12th International Conference on Miniaturized Systems for Chemistry and Life Sciences (μ TAS2008), 715 (2008).
2. "Fabrication and Estimation of Novel Micro Liquid Rotor that Operates with Surface-acoustic-wave," T. Saiki, K. Okada, Y. Utsumi, 12th International Conference on Miniaturized Systems for Chemistry and Life Sciences (μ TAS2008), 387 (2008).
3. "High Efficiency Mixing and Pumping of Continuous Liquid Flow using Surface-Acoustic-Wave," Y. Utsumi, T. Saiki, K. Okada, 13th International Conference on Miniaturized Systems for Chemistry and Life Sciences (μ TAS2009), 58 (2009).

High-sensitive enzyme-linked immunosorbent assay in three-dimensional lab-on-a-CD

Yoshiaki Ukita, Laboratory of advanced science and technology for industry
Tsukasa Azeta, Laboratory of advanced science and technology for industry
Saki Kondo, Laboratory of advanced science and technology for industry
Yuichi Utsumi, Laboratory of advanced science and technology for industry

Abstract

This paper reports a new lab-on-a-CD with three-dimensional(3D) microchannel network for the highly versatile and automatic immunoassay system. The lab-on-a-CD is consist of disks with planer microchannels and vertical channels, which fabricated by using conventional rapid prototyping method and x-ray lithography. The three dimensional lab-on-a-CD is applied to ELISA with standard sandwich protocol. The results suggest quite low detection limit (the several ng/ml order detection limit of immune globlin G of mouse).

Introduction

The lab-on-a-CD is promising for the automation of multiple microreactor systems. Recently, high-performance systems based on lab-on-a-CD has been proposed [1, 2]. However it is difficult to simultaneously realize the integration of many reactor units and various modules due to the restriction of chip size. In fact, the lab-on-a-CDs proposed by the references are integrating a few systems [1, 2].

To resolve this problem, we propose a new type lab-on-a-CD concept based on three-dimensional (3D) microchannel network. Figure 1 shows schematic illustration of 3D lab-on-a-CD consists of multiple layers of CD-like disks with different functions. By stacking multiple layers of lab-on-a-CD, it can compactly be integrated microreactor systems. It is also notable that the use of three-dimensional structure enhances the performance of modules. For example, it can be realized to improve the sensitivity of ELISA by increasing surface area for the immobilization of antibody, and optical path length is also increased by utilizing stacked structure as shown in fig. 1(b).

Experiments and Results

To demonstrate the ELISA, we carried out the sandwich ELISA by means of standard sandwich ELISA in fabricated 3D lab-on-a-CD. Planer PDMS lab-on-a-CD and through-hole PMMA lab-on-a-CD are fabricated by rapid prototyping and deep X-ray lithography respectively, and figs. 2(a, b) show the photograph of the disks and SEM images of bundle-like capillary structures.

To estimate the immobilization and specificity of antibody, we compared three different reaction conditions in the lab-on-a-CD. As shown in fig. 4, the absence of 1st antibody or absence of analyte result in low level signal, and presence of immobilized 1st antibody and analyte result in the higher signal. This result suggests successful immobilization of antibody with sufficient activity on the capillary bundle structure. It is also

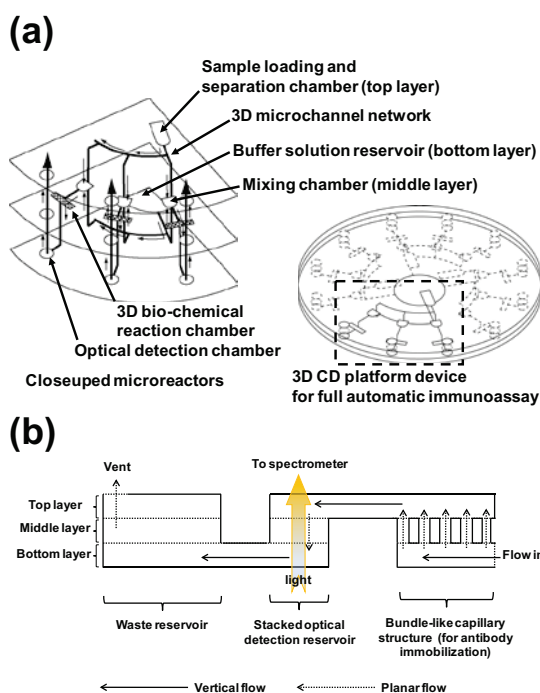


Figure 1: The schematic illustration of three-dimensional lab-on-a-CD. (a) Multiple layers with different functions are stacked and integrated together, to construct high-performance assay system. (b) Cross section of the 3D reaction chamber and optical detection reservoir.

notable that we succeeded in on-chip detection by means of absorption spectroscopy in three-dimensionally stacked detection reservoir with optical path of 700 μ m.

It is also very important to realize the on-chip washing for the automation. Prof. Madou's group reports the consumed volume of wash is three-times of the reaction reservoir, however it is concerned that the complex flow behavior in bundle-like capillary structure result in the difficulty of the washing. Thus we demonstrated and compared the results of ELISA by on-chip

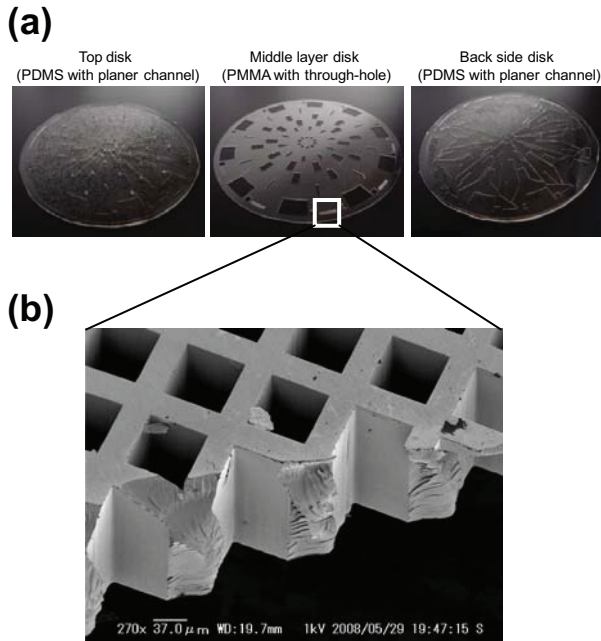


Figure 2. (a) Photographs of fabricated disks of 3D lab-on-a-CD. (b) SEM image of bundle-like capillary structure for antibody immobilization.

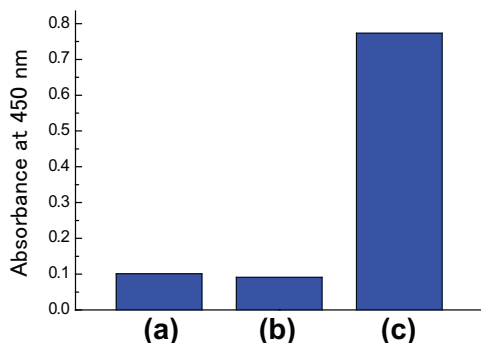


Figure 3. Comparison of three different reaction conditions. (a) with 1st antibody, and without analyte (Mouse IgG) (b) without 1st antibody, and with analyte (10 μg/ml of Mouse IgG) (c) with 1st antibody, and with analyte (10 μg/ml of Mouse IgG)

and off-chip washing step.

As shown in fig. 5, we successfully detected reasonable dose response of the signal reflecting the concentration of analyte. The corresponding assays to the each plot in the fig. 5 were simultaneously carried out and detected by on-chip absorption spectroscopy and the result also suggests stable filling of capillary bundle by centrifugal pumping. The estimated detection limit is quite sensitive less than several ng/ml and oval reaction time is less than 25 min. By comparing the results of on-chip washing and off-chip washing, it is very encouraging that the result of on-chip washing also exhibit clear dose response and plot of 1 ng/ml analyte is quite close to the back ground level of off-chip washing. We

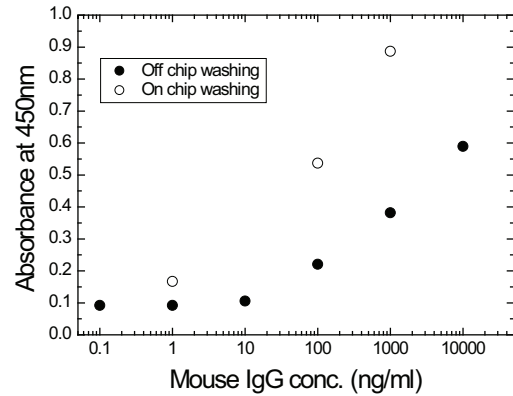


Figure 5. Obtained calibration curve by using three-dimensional lab-on-a-CD. The mouse IgG (analyte) is sandwiched by anti mouse IgG goat IgG and enzyme conjugated (HRP) anti-mouse IgG goat IgG. The signal of the enzyme reaction is amplified by high-sensitive peroxidase substrate (TMBZ). Closed plots are taken by off-chip washing protocol, and opened plots are taken by on-chip washing protocol.

believe that the on-chip washing is effectively controlling the back ground due to nonspecific binding of proteins.

References

- [1] B. S. Lee *et al.*, 1. "A fully automated immunoassay from whole blood on a disk", *Lab Chip*, **9**, 1548, (2009)
- [2] S. Lay *et al.*, 2. "Design of a compact disk-like microfluidic platform for enzyme-linked immunosorbent assay", *Anal. Chem.*, **76**, 1832, (2004)

Mask Observation Results using a Coherent EUV Scattering Microscope at NewSUBARU

Tetsuo Harada^{a)}, Junki Kishimoto, Takeo Watanabe, Hiroo Kinoshita

LASTI, University of Hyogo, 3-1-2, Koto, Kamigori, Ako, Hyogo, Japan 678-1205

JST, CREST, Japan

Dong Gun Lee

Samsung Electronics Co., LTD., San #16 Banwol-Dong, Hwasung-City, Gyeonggi-Do, Korea, 445-701

^{a)} Electronic mail: harada@lasti.u-hyogo.ac.jp

A coherent scattering microscope for extreme ultraviolet (EUV) light has been developed for the actinic inspection of EUV lithography masks. It was installed at the NewSUBARU synchrotron facility. It provides aberration-free, diffraction-limited imaging and a high numerical aperture. Coherent EUV light scattered (diffracted) from a mask is recorded using a CCD camera with a numerical aperture of 0.15. An image of the sample is reconstructed using a hybrid input-output algorithm, which retrieves the phase from the intensity data. Masks containing periodic line-and-space and hole patterns with a half pitch ranging from 100 nm to 400 nm were fabricated in our laboratory and imaged. The reconstructed images correlate well with images obtained with a scanning electron microscope (SEM). The actinic critical dimension of the line width of TaN absorber patterns on a mask was measured and was consistently found to be 25 nm larger than that obtained from the SEM data.

I. INTRODUCTION

Extreme ultraviolet (EUV) lithography is a promising technology for the production of semiconductor devices at the 32-nm node. The fabrication of a defect-free mask is a critical issue. An EUV mask consists of a glass substrate with a reflective multilayer coating and a patterned absorber coating. A Mo/Si multilayer exhibits a high reflectivity of 70% at $\lambda = 13.5$ nm, which is the working wavelength of EUV lithography. The required accuracy of the critical dimension (CD) for the 32-nm node is less than 2.6 nm.¹ To achieve that level of accuracy, it is necessary to be able to precisely determine the line width of a mask pattern. Thus, at-wavelength observations with an EUV microscope is essential for estimating the actinic CD of the reflection profile. There are two types of defects in EUV lithography masks: amplitude defects, which are caused by particles on the surface of a mask, and phase defects, which are caused by defects in the substrate and particles in the multilayer. To detect phase defects on mask blanks, SELETE has developed a dark-field inspection tool employing Schwarzschild optics and a laser plasma source². To inspect finished (patterned) masks, the LBNL group has developed an actinic inspection tool that employs a Fresnel zone plate as an optical component.^{3,4} It is installed at the ALS synchrotron facility. This microscope has a numerical aperture (NA) of 0.0875

and a field diameter of 5 μm , and can estimate CDs ranging from 100 nm to 500 nm. However, aberration makes it difficult to obtain a high NA at the Fresnel zone plate. We have developed an EUV microscope that employs Schwarzschild optics and an X-ray zooming tube,^{5,6} and installed it at the NewSUBARU synchrotron facility. It has a high NA of 0.3 and a large field with a diameter of 50 μm . Because of the low magnification (30 \times) of the Schwarzschild optics, the zooming tube uses electromagnetic lenses to magnify a projected mask image by 10-200 \times . The optics for these actinic inspection tools are difficult to produce and align, and they become more complex as the NA and magnification become higher.

This paper describes a coherent EUV scattering microscope (CSM) based on X-ray diffraction microscopy.^{7,8} It requires no objective and uses only coherent EUV light. The scheme is simple: Coherent EUV light illuminates a region of a patterned EUV mask, and an EUV CCD camera records the intensity distribution of the scattered (diffracted) light. In a conventional diffraction imaging setup, an objective collects both phase and amplitude information from the sample. In contrast, the CSM records only the diffraction intensity of the sample, which contains only amplitude information. The missing phase information is retrieved by using a hybrid input-output (HIO) algorithm,⁹ which iteratively

calculates the Fourier transform and the inverse Fourier transform, subject to constraints.

The CD for a periodic mask can be determined from the intensity ratios of the zero, 1st, 2nd, and

II. DESIGN OF COHERENT EUV SCATTERING MICROSCOPE

The CSM is installed on the BL-3C beamline¹⁰ of the NewSUBARU synchrotron facility, which has a bending-magnet source. Two toroidal mirrors collimate the white light, and a Mo/Si multilayer deflects the beam at the C station by a designed angle of 0.75 mrad. This multilayer has a peak reflection wavelength around 13.5 nm at an angle of incidence of 10°. Figures 1 and 2 show a schematic and a photograph, respectively, of the CSM at the end station of the BL-3C; and Table 1 lists the specifications. The optical path in the CSM chamber begins with a 5- μm -diameter pinhole and a 200-nm-thick Zr filter, which reduces the beam diameter and partially monochromatizes the beam. Next, a concave spherical mirror reflects the beam

higher diffraction orders, which makes the CSM a useful tool for quickly estimating the CD. The zero diffraction order means direct reflection from the mask.

(incident angle: 3°) and a planar mirror reflects it (incident angle: 39°) onto an EUV mask. The two mirrors are coated with 40 pairs of Mo/Si layers, which have a peak reflectivity of 43% at $\lambda = 13.4$ nm, and 52% at $\lambda = 13.5$ nm. The Zr filter, the three Mo/Si multilayers of the branching mirror, and the two mirrors of the CSM monochromatize the beam striking the EUV mask at a wavelength of 0.3 nm. When the CSM is used for estimating the CD, the results accurately take the shadowing effects of the absorber pattern into account because the angle of incidence on an EUV mask is 6°, which is the same as that for the alpha EUV exposure tools ADT (ASML) and EUV1 (Nikon).

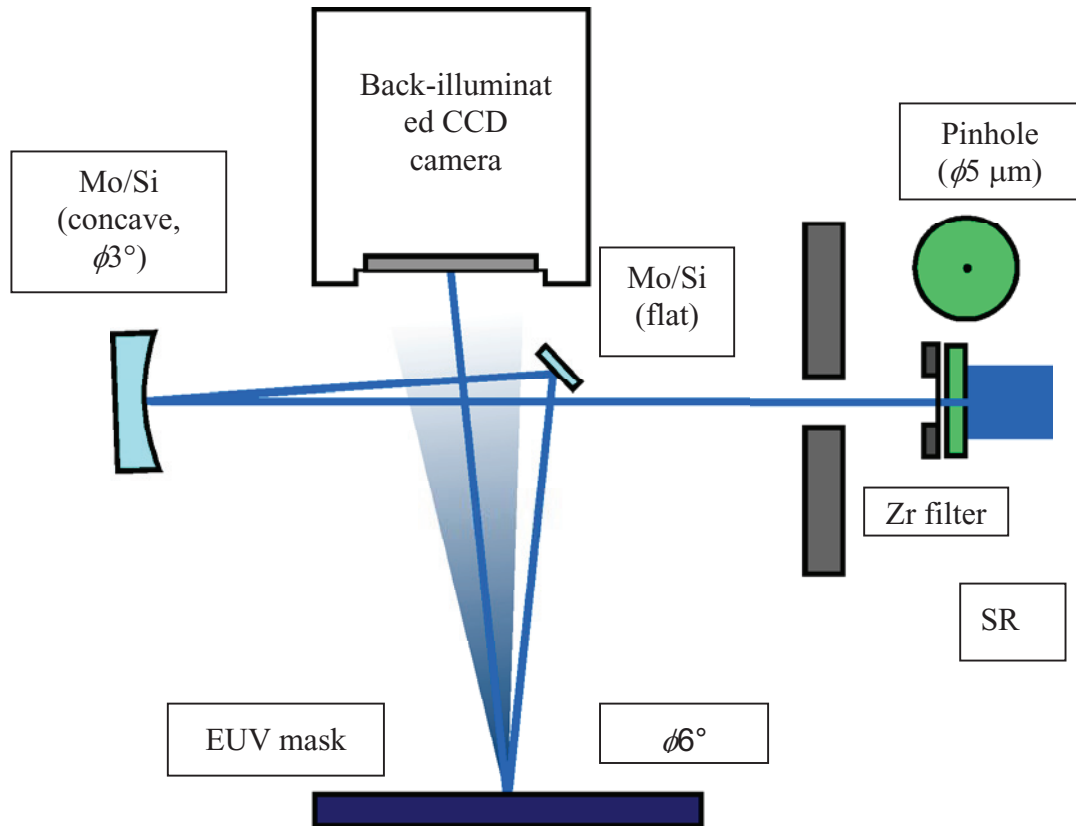


Figure 1. Schematic diagram of coherent EUV scattering microscope (CSM). All the optics, including the CCD camera, are inside the vacuum chamber.

Due to the off-axis illumination of the alpha tools, the CD includes the effects of shadowing by the absorber pattern. The concave mirror (radius of curvature: 163 mm) projects the pinhole image onto the mask. It is 163 mm from the pinhole and the same distance from the mask. Due to aberrations inherent in the use of a pinhole for imaging, the size of the pinhole was made significantly larger than the wavelength. The beam divergence is equal to the calculated diffraction angle. The area of the concave mirror that is exposed is less than a millimeter in diameter. The spot size calculated by means of a ray-tracing program that traced rays from the pinhole to the mask is 1 μm . The pinhole image is almost the same size as the object, which limits the field size of the CSM. To obtain good contrast for the reconstruction of mask images, the diffraction field should be at least 5 μm across to produce interference at the position of the CCD camera. The spatial coherence length of the incident beam is 18 μm , as estimated from the divergence. This is substantially larger than the required field size.

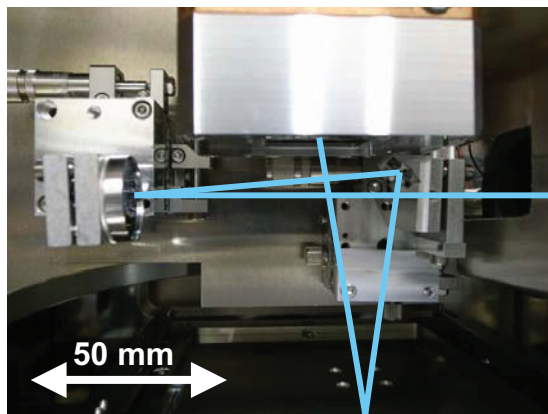


Figure 2. Photograph of coherent EUV scattering microscope (CSM). The solid line is the optical path of the SR light.

The CCD camera (MTE-2048B, Roper Scientific) can operate in a high vacuum and has a back-illuminated CCD without an anti-reflection coating. The surface of the CCD is parallel to the

surface of the mask. The imaging area is 27.6 mm square; it contains a 2048 \times 2048 array of imaging pixels, each of which is 13.5 μm square. The CCD camera has a quantum efficiency of 42% for EUV photons and a 16-bit analog-to-digital converter. The camera is cooled to -50°C . The RMS noise of the CCD was estimated to be 7 counts from counting dark frames for 5 minutes. The dynamic range was estimated to be 4 orders of magnitude. The distance from the mask to the CCD camera is about 92 mm, which is equivalent to an NA of 0.15. The estimated spatial resolution for this NA and coherent illumination is 90 nm. It can be improved by shifting the CCD camera so that it records higher diffraction orders. A 200-nm-thick Zr filter was placed just after the pinhole to remove the UV-visible components of the specular reflection from the Mo/Si multilayers. The CSM has a shadowgraph mode that uses visible light to align the mask. In this mode, a linear-stage is used to replace the Zr filter and the 5- μm -diameter pinhole with a visible ND filter and a 4-mm-diameter pinhole. The mask X-Y stage can move ± 60 mm to enable observation of the whole area of an EUV mask of 6025 size with encoders. The step resolution for movement is 4 μm . The CSM chamber has a load lock apparatus for sample exchange, which takes about one hour.

Table 1. Specifications of coherent EUV scattering microscope.

Light source	White SR light (Bending)
Center wavelength	13.5 nm
Bandwidth	0.3 nm
Field size	$\phi 5 \mu\text{m}$
Incident angle	6°
Numerical aperture	0.15
Spatial resolution	45 nm hp
Mask size	6025 glass substrate
Imaging device	Back-illuminated CCD

III. FABRICATION OF EUVL MASK PATTERNS

Test EUV masks were fabricated to evaluate the CSM specifications. Since coherent EUV scattering microscopy is a new technique for observing EUV masks, various types of masks with a variety of patterns and phase defects are needed for the evaluation. In this study, we fabricated standard line-and-space (L/S) and hole patterns to develop our fabrication technique. The masks consist of a Si substrate, a Mo/Si multilayer coating, and a TaN absorber layer. The Mo/Si multilayer has 40 6.9-nm-thick periods; and the ratio of the Mo layer thickness to the period thickness is 0.4. The TaN layer is 80 nm thick and has a calculated reflectivity of less than 0.1%. In the mask fabrication process (Fig. 3), first a Si substrate is coated with a Mo/Si multilayer by magnetron sputtering (MPS-4500, ULVAC). Next, the TaN layer is deposited; and a spin coater covers it with a 200-nm-thick layer of

ZEP520A resist. Electron beam lithography (ELS-7500, ELIONIX) is used to write the pattern in the resist; and the mask is etched by ICP dry etching (TCP 9400SE Alliance, Lam Research). Three types of patterns were fabricated: horizontal and vertical L/S patterns, and holes. The half pitch (hp) ranged from 50 to 500 nm. Each pattern was formed on a 20- μm -square area, which is larger than the field size (ϕ 5 μm). Forty-eight patterns were fabricated in each 300- μm -square block (Fig. 4). Nine blocks were fabricated on a 4-inch Si wafer, along with alignment marks to make alignment of the mask easy. The alignment marks are useful for locating the position of a pattern in the shadowgraph mode of the CSM. Regarding the fabrication results, the 50-nm-hp patterns collapsed due to the high aspect ratio of the resist. The 60-nm-hp and 200-nm-hp patterns were fabricated successfully (Fig. 5). A half pitch of 60 nm on a mask is equivalent to a half pitch of 15 nm for semiconductor devices.

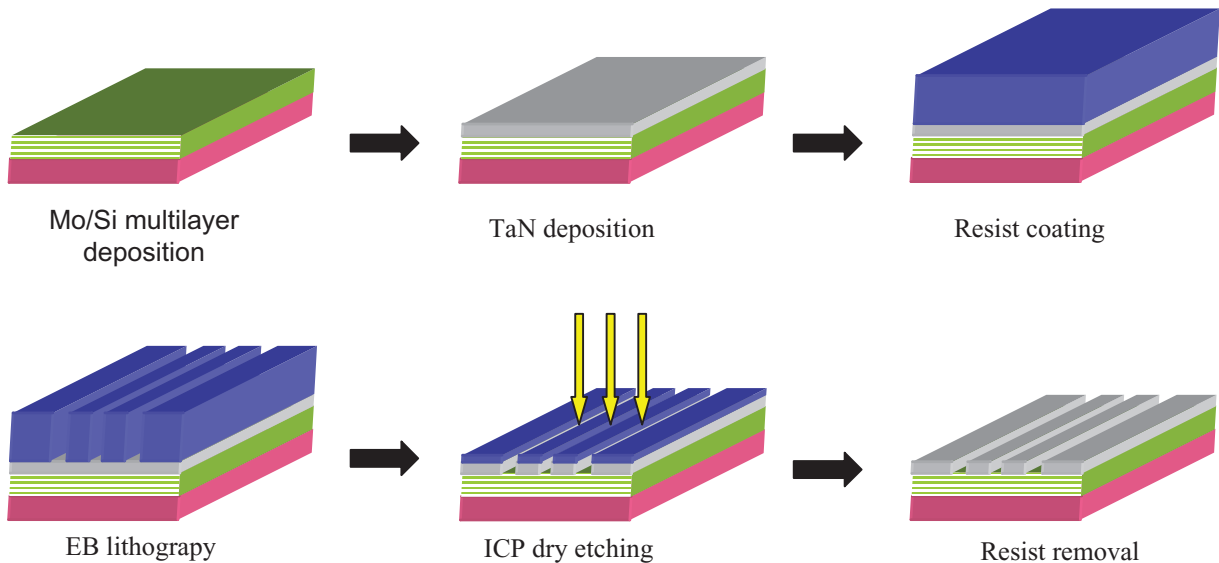


Figure 3. Fabrication process for EUV mask.

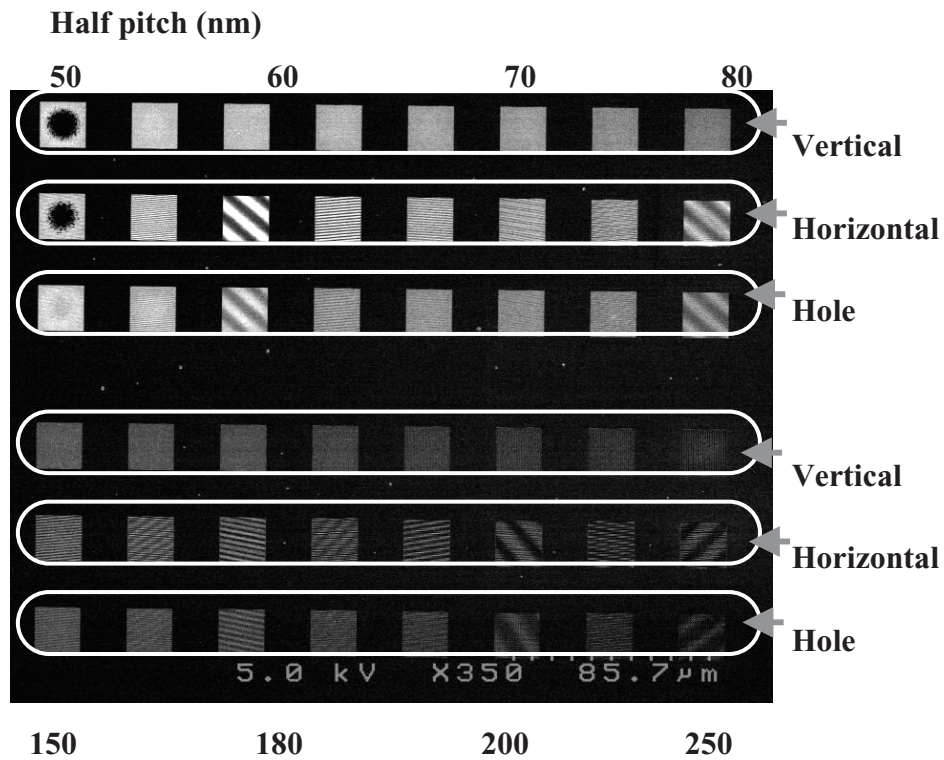


Figure 4. SEM image (top view) of fabricated EUV mask. Each square is about 20 μm on a side. There are 48 squares containing vertical L/S, horizontal L/S, and hole patterns with half pitches ranging from 50 nm to 500 nm.

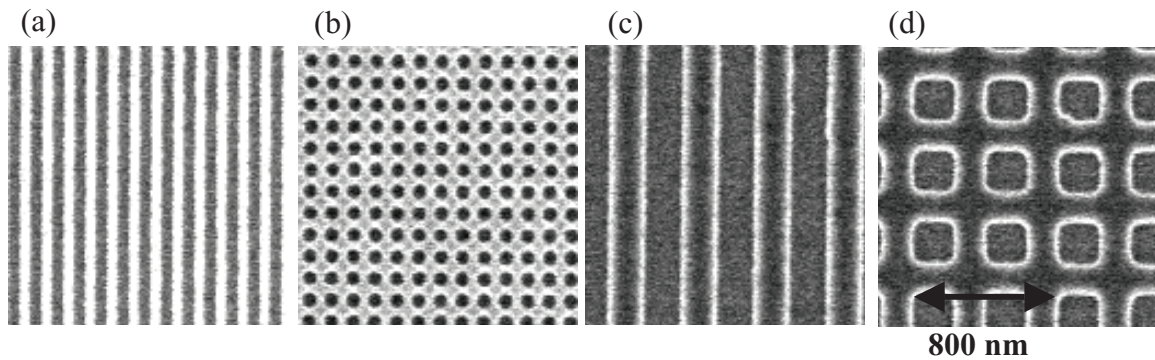


Figure 5. SEM images of fabricated EUV mask: (a) 60-nm-hp L/S, (b) 60-nm-hp holes, (c) 200-nm-hp L/S, (d) 200-nm-hp holes.

IV. RESULTS

To obtain a contrast image of the mask, the CCD camera signal was measured at two positions, namely, on the surface of the Mo/Si multilayer and on the surface of the absorber layer, with a ratio of 39. The reflectivity contrast was found to be as high as 0.95. The reflectivity of the absorber layer was estimated to

be 1.5%, assuming the reflectivity of the Mo/Si multilayer to be about 60%. Since the reflectivity of the absorber layer was higher than the calculated value ($< 0.1\%$), the thickness and/or the absorption coefficient of that layer must be different from the values used in the calculation.

Figure 6 shows images obtained with the CSM of the 200-nm-hp L/S pattern in Fig. 5(c): (a) CCD image, (b) reconstructed image, (c) magnified image of (b), and (d) profile at the center of the reconstructed pattern. The shadowing effects of the absorber pattern are negligible because the incident light was parallel to the L/S pattern. The exposure time was limited to 12 minutes so that the CCD

signal would not be saturated with zero-order light. Figure 6(a) is the diffraction intensity recorded by the CCD camera. The center signal is zero-order light, and up to 4 diffraction orders were recorded. The aura around the zero order is due to the Fraunhofer diffraction of the pinhole. The signal counts for the zero, 1st, 2nd, 3rd, and 4th diffraction orders were 44300, 17955, 915, 1803, and 527, respectively.

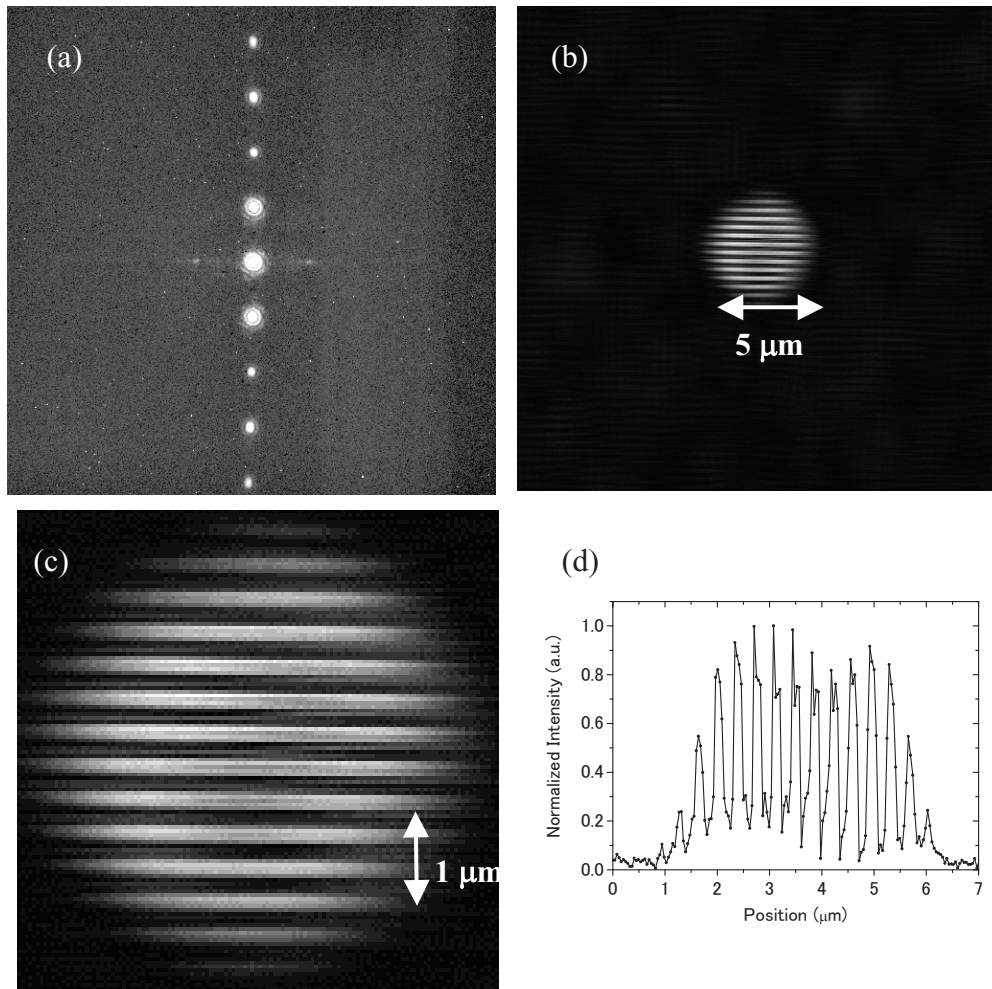


Figure 6. CSM results for 200-nm-hp L/S pattern: (a) CCD image, (b) reconstructed image obtained with HIO algorithm, (c) magnified image of (b), and (d) profile of center of (c).

The CD of the absorber thickness was found to be 224.2 ± 2.6 nm by fitting the peak diffraction intensities to the Fraunhofer diffraction distribution. On the other hand, a one-minute exposure yielded a CD of 224.8 ± 3.7 nm. Since these values are virtually the same, we can conclude that a one-minute exposure is sufficient for estimating the CD. The exposure time could be further reduced by increasing the field of view and by developing a peak detection algorithm. The CD obtained with the SEM was 199

nm, which is smaller than that obtained with the CSM. The SEM detects secondary electrons at the surface of the absorber, and the CSM detects the distribution of the reflectance. Thus, the CD for absorber patterns obtained with the SEM is smaller because the patterns have sloping edges. The dependence of CD on absorber shape will be investigated in the future.

In reconstructing a diffraction image, the signal-to-noise (S/N) ratio is improved by resampling the CCD data to reduce the size of the pixel array

from the original 2048×2048 pixels to 512×512 pixels, where the estimated oversampling ratio⁷ is 16. A threshold is also put on the CCD signal to further reduce the noise. The images in Fig. 6(b-c) are reconstructions obtained with 200 iterations of the HIO algorithm. They correlate well to the SEM image in Fig. 5(c). For the reconstruction, the phase in real space was not constrained to be real and positive because the target of the CSM contained a phase defect. In addition, the absorber pattern produces a phase shift corresponding to its thickness. The constraint used in reconstruction was the size of the support area (that is, the illuminated area). The support area was optimized so as to reduce the error signal in real space (mask image) in the unilluminated area. A loose support constraint was initially applied, but the bright image of the 5- μm field moved around in the support area as the iteration proceeded. For optimization, a tight support size was chosen, with a step-by-step increase in the support size to reduce the error. The CD of the reconstructed image profile is about 219 nm, which is

about the same as the fitting results for the diffraction peaks.

Figures 7 and 8 show a 100-nm-hp L/S pattern and a 400-nm-hp hole pattern, respectively, taken with the CSM using exposure times of 8 and 10 minutes. Estimation of the CD requires not only zero- and 1st-order diffraction images but also 2nd-order ones. At present, the CSM cannot record 2nd-order diffraction for patterns with a half pitch of less than 100 nm because of the limited NA. However, 1st-order diffraction was clearly recorded for half pitches from 60 nm to 90 nm. Thus, the pattern with the smallest hp (60 nm) fabricated in our laboratory exhibited a periodic structure when observed with EUV light. In Fig. 7, the reconstruction for the 100-nm-hp L/S pattern is very good. The CD obtained from the SEM image is 95 nm; that from the CSM image is 120.7 ± 2.1 nm; and that from the reconstructed image profile is 119 nm. The CD from the CSM is larger than that from the SEM.

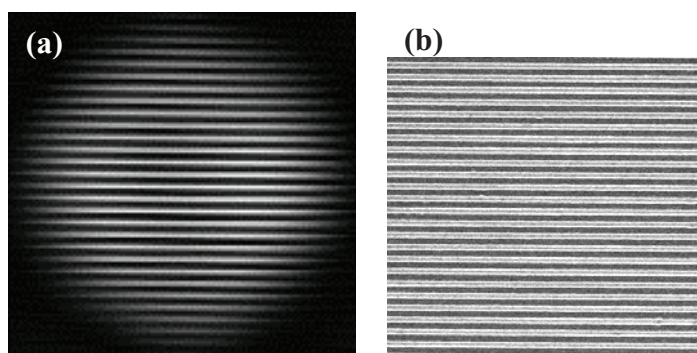


Figure 7. 100-nm-hp L/S pattern: (a) reconstructed image obtained with CSM and (b) SEM image.

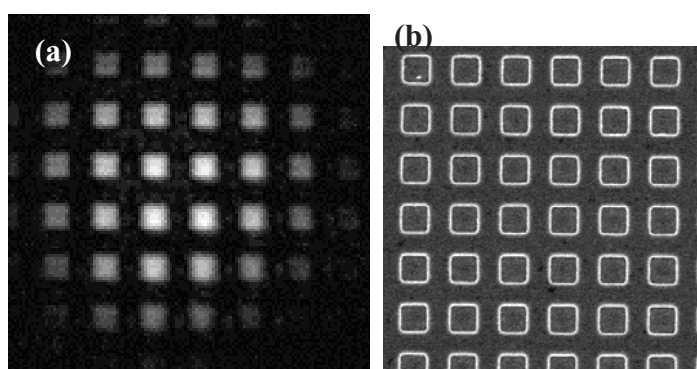


Figure 8. 400-nm-hp hole pattern: (a) reconstructed image obtained with CSM and (b) SEM image.

For the hole pattern in Fig. 8, the reconstructed image corresponds to the SEM image. However, there is a reconstruction error in the absorber region, possibly due to the low reflectivity of the EUV mask.

The count for the zero-order signal was about 3,000, which is only 1/10 of that for the L/S pattern. The L/S and hole patterns were fabricated on the same substrate, but the absorber layer was not completely etched off the holes, even though the dry etching

process was identical. The etching conditions for the

absorber layer need to be optimized.

V. CONCLUSION

A CSM has been developed for the actinic inspection of EUV lithography masks, and it has been installed at the NewSUBARU synchrotron facility. To evaluate its performance, EUV masks containing L/S and hole patterns with half pitches ranging from 50 nm to 500 nm were fabricated, and the CSM was used to image them. EUV mask patterns with half pitches down to 100 nm were successfully reconstructed. For L/S patterns, the image shapes were well reconstructed and matched those in the SEM images. The actinic CD of an L/S pattern was estimated from a one-minute exposure with the CSM, and was found to be only 25 nm wider than the CD obtained with a SEM. Our results demonstrate that the CSM can be used to image EUV masks and obtain the actinic CD. Thus, the CSM is a practical tool for inspecting EUV masks.

In the near future, we will develop a tabletop high-order harmonic generation (HHG) laser EUV source¹¹ for the practical inspection of EUV masks. The power will be 1000 times greater than that of our present source, which wastes most of the light in achieving high spatial coherence. The target defect detection sensitivity of this actinic inspection tool is less than 20 nm for the 22-nm node, which translates into a feature size of 5 nm on a wafer. The target sensitivity for the CD is about 0.1 nm, and the target scanning time for a whole mask is less than 90 minutes.

Acknowledgement

This work was partially supported under the JST-CREST project “Development of Ultra-Fine Structure Metrology System using Coherent EUV Source.”

References

1. Semiconductor Industry Association, “International Technology Roadmap for Semiconductors: 2007 Lithography”, Austin, TX, International SEMATECH.
2. T. Terasawa, Y. Tezuka, M. Ito and T. Tomie, SPIE Proc. **5446**, 804 (2004).
3. A. Barty, Y. Liu, E. Gullikson, J. S. Taylor, and O. Wood, SPIE Proc. **5751**, 651 (2005).
4. K. A. Goldberg, P. P. Naulleau, A. Barty, S. B. Rekawa, C. D. Kemp, R. F. Gunion, F. Salmassi, E. M. Gullikson, E. H. Anderson and H. Han, SPIE Proc. **6730**, 67305E (2007).
5. T. Haga, H. Takenaka and M. Fukuda, J. Vac. Sci. Technol. B **18**, 2916 (2000).
6. K. Hamamoto, Y. Tanaka, H. Kawashima, S. Y. Lee, N. Hosokawa, N. Sakaya, M. Hosoya, T. Shoki, T. Watanabe and H. Kinoshita, Jpn. J. Appl. Phys. **44**, 5474 (2005).
7. J. Miao, P. Charalambous, J. Kirz and D. Sayre, Nature **400**, 342 (1999).
8. J. Miao, Y. Nishino, Y. Kohmura, B. Johnson, C. Song, S. H. Risbud and T. Ishikawa, Phys. Rev. Lett. **95**, 085503 (2005).
9. J. R. Fienup, Appl. Opt. **21**, 2758 (1982).
10. T. Watanabe, T. Haga, M. Niibe and Hiroo Kinoshita, J. Synchrotron Rad. **5**, 1149 (1998).
11. E. J. Takahashi, Y. Nabekawa and K. Midorikawa, Appl. Phys. Lett. **84**, 4 (2004).

Imaging Performance Improvement of an Extreme Ultraviolet Microscope

Kei Takase, Yoshito Kamaji, Naoki Sakagami, Takafumi Iguchi, Masaki Tada, Yuya Yamaguchi, Yasuyuki Fukushima, Tetsuo Harada, Takeo Watanabe, and Hiroo Kinoshita
Laboratory of Science and Technology for Industry, University of Hyogo
1-1-2 Kouto, Kamigori, Ako-gun, Hyogo 678-1205, Japan

The extreme ultraviolet microscope (EUVM) has been developed for an actinic mask inspection of a EUV finished mask and a EUV blank mask. Using this microscope, amplitude defects on a finished mask and phase defects on a glass substrate are observed. However, it has a problem of low contrast, which originates from 1) thermal noise of a charge coupled device (CCD) camera, 2) wave aberrations of an optical component, and 3) a nonuniform illumination intensity. To resolve these issues, EUVM was improved. 1) To reduce a thermal noise, a cooled CCD camera is installed. 2) To remove wave aberrations of a back-end turning mirror, a Mo/Si multilayer-coated thick glass substrate with a high surface accuracy is employed instead of a Si wafer substrate. Furthermore, in situ alignment was carried out to remove wavefront aberrations for a Schwarzschild imaging optics. In addition, 3) by installing a scanning system on the front-end turning mirror, a highly uniform illumination intensity was achieved. As a result, images of less than 100 nm without astigmatism were obtained.

1. Introduction

In Accordance with the ITRS roadmap, extreme ultraviolet lithography (EUVL) is expected to be introduced into the high-volume manufacturing process from the 22-nm half-pitch node from 2013.¹⁾ The fabrication of a defect-free mask is the first issue of EUVL technology.²⁾ There are two types of defects on EUVL masks. One is an amplitude defect and the other is a phase defect.³⁻⁷⁾ An amplitude defect originates from either a particle on the surface of the multilayer or a flaw in the multilayer.^{8,9)} On the other hand, a phase defect is produced when the multilayer is deposited over either a bump or a pit on the substrate. Since the intensity of reflected light decreases owing to a phase shift, the projection image of the mask area with the phase defect is affected.

There are two techniques of detecting a small defect on an EUVL mask: using deep ultraviolet (DUV) light¹⁰⁾ and using EUV light at the exposure wavelength.¹¹⁻¹⁹⁾ Mask defect inspection using DUV light is a conventional method that is used in optical lithography. However, this inspection has a difficulty in detecting a phase defect inside the Mo/Si multilayer of an EUVL mask because the DUV light is reflected on the surface of a mask. Thus, the at wavelength mask inspection method is necessary for phase defect inspection of an EUV mask. Therefore, we constructed an extreme ultraviolet microscope (EUVM) system.^{3-5,20)} Figure 1 shows the configuration of

the actinic EUVM installed at the BL-3 beamline of the NewSUBARU synchrotron radiation (SR) facility. It consists of Schwarzschild optics (NA, 0.3; magnification, 30x) as the illumination and imaging optics, an X-Y-Z sample stage, an X-ray zooming tube connected to a CCD camera, and an image processing computer. It is installed in a vacuum chamber (pressure, 1×10^{-5} Pa) on a vibration isolation table. Figure 2 shows the mechanism of phase defect inspection with EUVM. When the multilayer fulfills the Bragg condition, the EUV light that penetrates into the multilayer is normally reflected. However, if there is a defect pattern on a substrate under the multilayer, the Bragg condition is not satisfied in the multilayer, the light on the defect could not reflect in the right direction to Schwarzschild optics and makes no imaged on the X-ray zooming tube. Thus, an image of a phase defect is observed by a EUVM. EUVM can image phase defects directly, even on a multilayer with a flat surface.

We have observed the finished mask with the absorber pattern and the mask blanks with programmed phase defects to identify the critical dimensions of phase defects on mask blanks.⁷⁾ However, there were nonuniform intensity distribution and wave aberrations. In this paper, image quality improvement technologies are discussed.

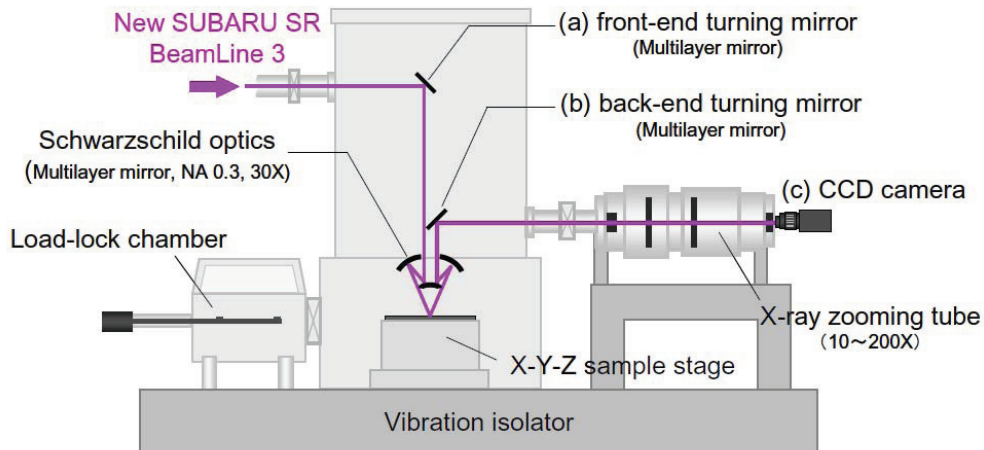


Fig. 1 Setup configuration of the EUVM system. (a) front-end turning mirror (b) back-end turning mirror (c) CCD camera.

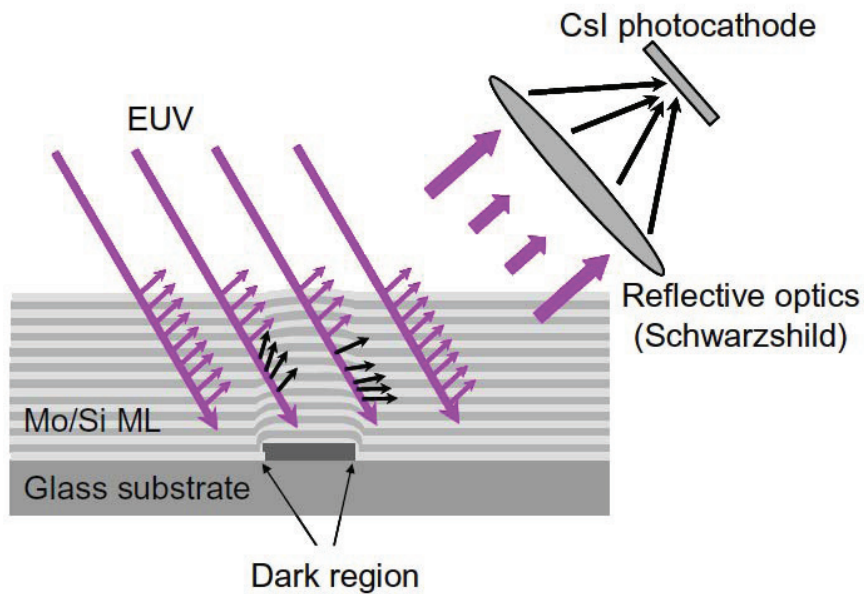


Fig. 2 Mechanism of phase defect inspection.

2. Issue of Imaging Quality

Figure 3 shows an image of a 300-nm-half-pitch (hp) elbow pattern observed using EUVM in our previous work²¹⁾. Since the image includes remarkable wavefront aberrations, the resolution in the horizontal direction and that in the vertical direction are different. These aberrations resulted from the surface

flatness of the substrate of the back-end turning mirror and the wavefront error of the Schwarzschild optics. Furthermore, this image includes nonuniform intensity, which reduces the resolution of the imaging. This nonuniformity also resulted from the surface figure error of the front-end mirror.

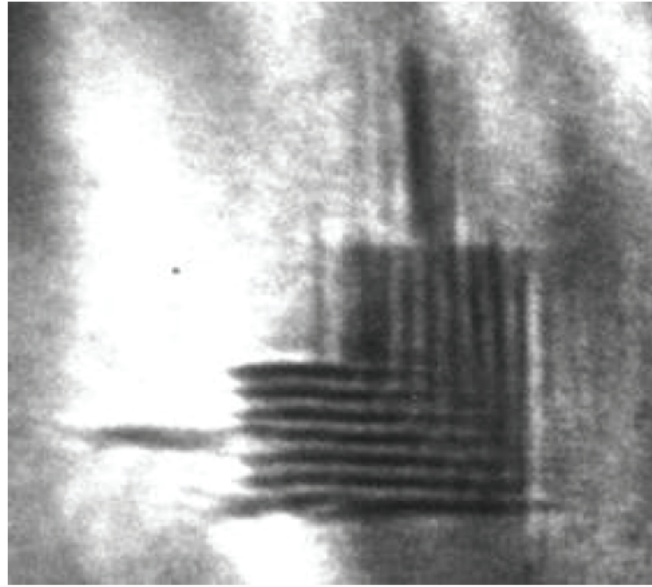


Fig. 3 EUVM image of 300-nm-hp elbow pattern in our previous work (magnification: 1800x).

Figure 4 shows the surface flatness of the Si wafer substrate of the back-end turning mirror. As shown in Fig. 4, the surface figure of the back-end turning mirror was about 166 nm (rms). To reduce

wave aberrations, a lower-figure-error substrate should be employed. In addition, in situ alignment of Schwarzschild optics is required to reduce wavefront aberrations.

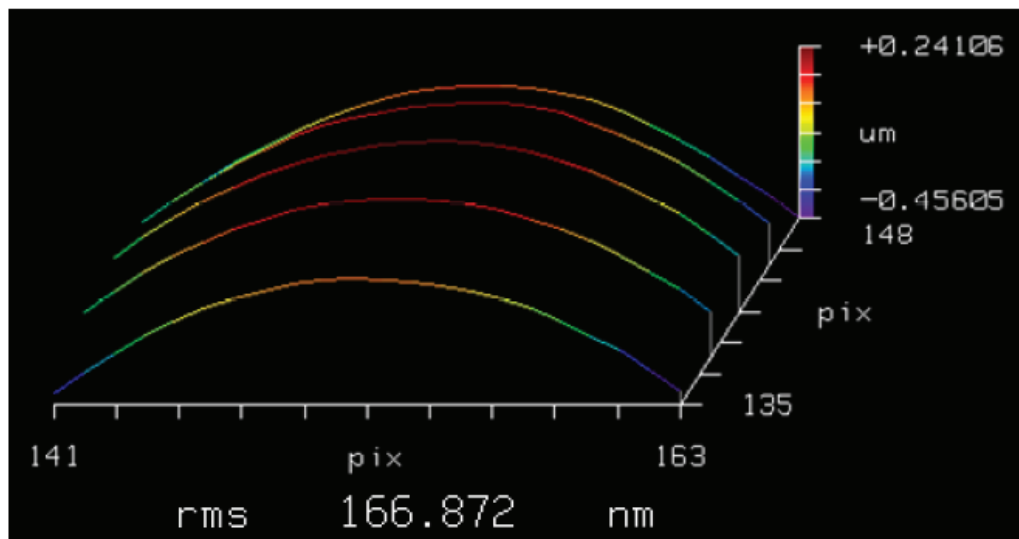


Fig. 4 The surface flatness of Si wafer substrate of back-end turning mirror was about 166 nm (rms).

Figures 5(a) and 5(b) show images of the 300-nm-half pitch (hp) pattern taken using EUVM at total magnifications of (a) 1800x and (b) 6000x, respectively. The noise considered to be thermal

noise of CCD camera is observed at the magnification of 6000x. To reduce the thermal noise of CCD camera, a cooling CCD camera is effective.

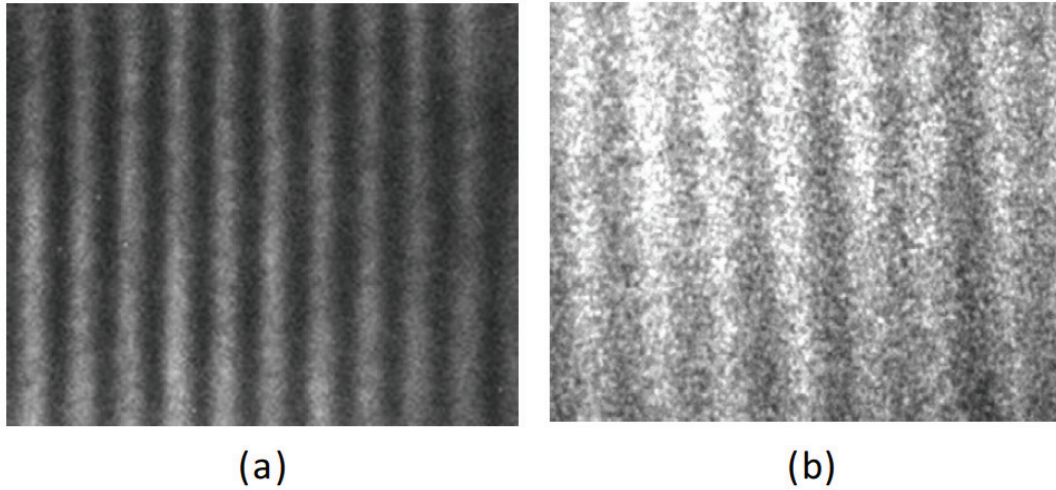


Fig. 5 EUVM images of 300-nm-hp pattern taken at total magnifications of (a) 1800x and (b) 6000x.

3. Imaging Quality Improvement

3.1 Thermal noise reduction utilizing cooling CCD camera

The conventional CCD camera was replaced with a cooling CCD to increase a high S/N ratio of the EUVM images by reducing thermal noise. Table I shows the performance of the CCD camera and cooling CCD camera. Figure 6 shows the background images taken by the conventional (a) and cooling (b) CCD cameras without the optical input observed by EUVM and the intensity distribution of the image. The cooling CCD temperature was set at a minimum cooling temperature of -27 °C. The thermal noise of the cooling CCD camera disappeared, as shown Fig. 6(b), and the camera enabled the acquisition of uniform-background images. Therefore, the cooling CCD camera also enabled the acquisition of EUVM

images of high contrast at a maximum magnification of 200x. Figures 7(a) and 7(b) show the EUVM images of a 150-nm-hp pattern at a magnification of 6000x before and after the updating the CCD camera. The contrast of the 150-nm-hp pattern was increased from 0.22 to 0.38 when using a cooling CCD camera. The contrast can be calculated using the following equation:

$$Contrast = \frac{I_{max} - I_{min}}{I_{max} + I_{min}},$$

where I_{max} and I_{min} are the average maximum value and the average minimum value of the EUV intensity distributions of the line and space pattern, respectively.

Table I . The performance of a CCD camera and a cooling CCD camera.

	CCD camera	Cooling CCD camera
Imaging area (μm^2)	9.0×6.7	14.8×10.0
Pixels	1392×1040	2184×1472
Pixel size (μm)	6.45×6.45	6.8×6.8
Minimum cooling temp. (°C)	—	-27

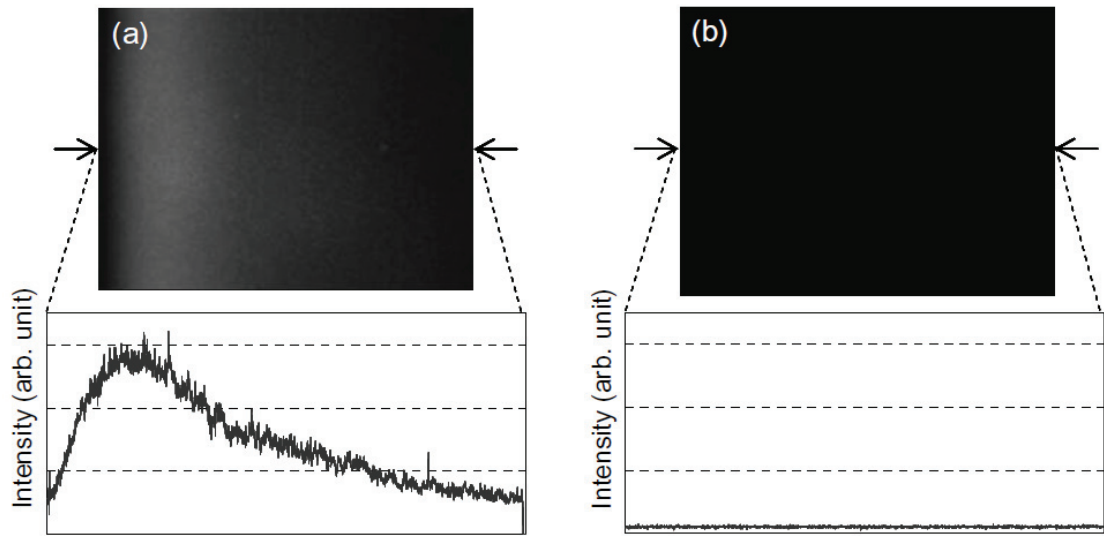


Fig. 6 EUVM background images without optical input and the intensity profiles of each image. (a) taken with a CCD camera, (b) taken with a cooling CCD camera.

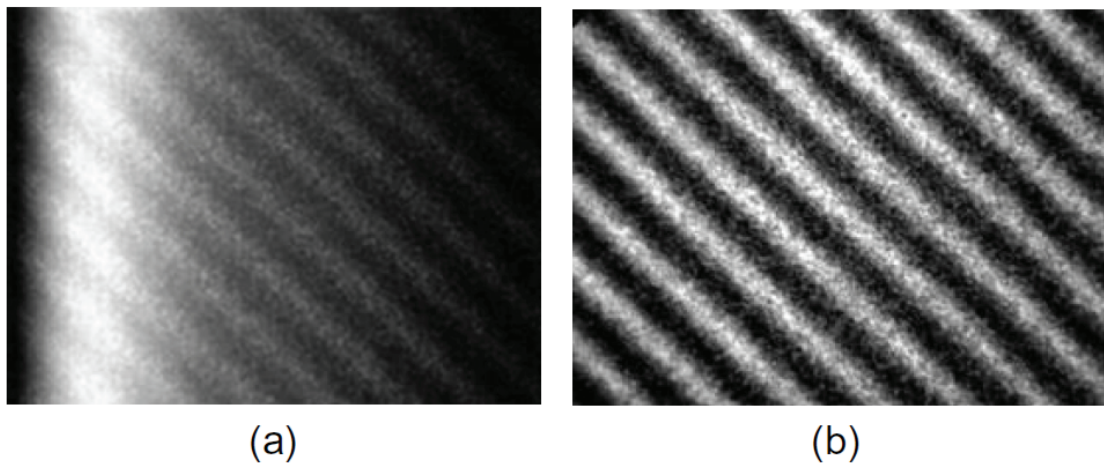


Fig. 7 EUVM images of 150 nm Line and Space (L/S) pattern (a) taken with a CCD camera, (b) taken with a cooling CCD camera (magnification: 6000x).

3.2 Reduction of wave aberration to improve optical components

To reduce the wavefront aberration, in general, a smooth and flat mirror surface and highly accurate alignment of the optical system are necessary for the imaging. In the EUVM system, a Mo/Si multilayer coated on the Si wafer was employed as the back-end turning mirror. As shown in Fig. 4, this mirror has a surface figure error of 166 nm (rms), it causes a large wavefront aberration and defocusing. Furthermore, in the alignment of an optical system (carried out by wavefront measurement using a laser interferometer) in the atmosphere, alignment accuracy changes after a period time. It causes imaging aberrations.

The Mo/Si multilayer coated on a thick glass substrate with a smooth surface was employed as a back-end turning mirror in the EUVM system, as indicated by (b) in Fig. 1 instead of the Mo/Si multilayer coated on a Si wafer substrate to improve wave aberrations. The wavefront error of the updated mirror was measured using a Fizeau interferometer (ZYGO GPI) and has a flatness of 3.7 nm (rms), as shown Fig. 8. In addition, we also carried out in situ alignment of the Schwarzschild imaging optics to reduce wave aberrations. Namely, an X-Y-Z-axis alignment mechanical system for each mirror of the imaging optics, which enables movement in vacuum is installed in the optical housing.

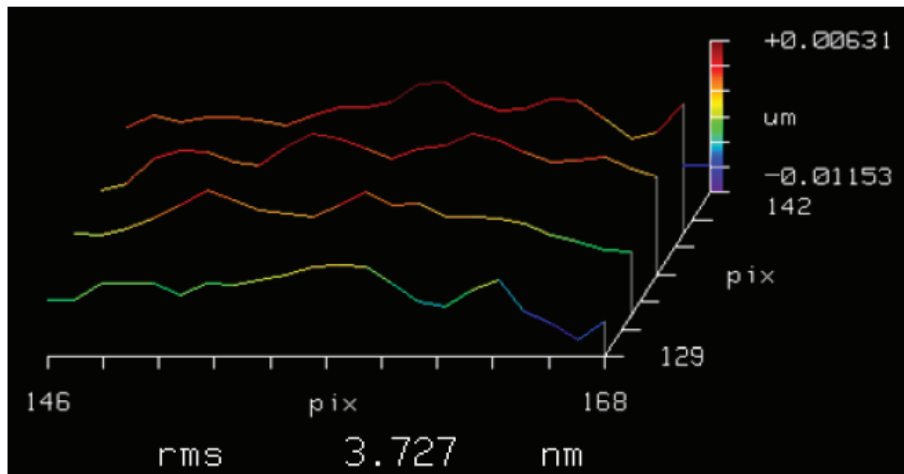


Fig. 8 The surface flatness of thick glass substrate of back-end turning mirror was about 3.7 nm (rms).

Figures 9(a) and 9(b) show the observed images of a 480-nm-hp elbow pattern before and after reducing wavefront aberrations, respectively. As a

result of changing a thick mirror and introducing in situ alignment, the wavefront aberrations and resolution were improved.

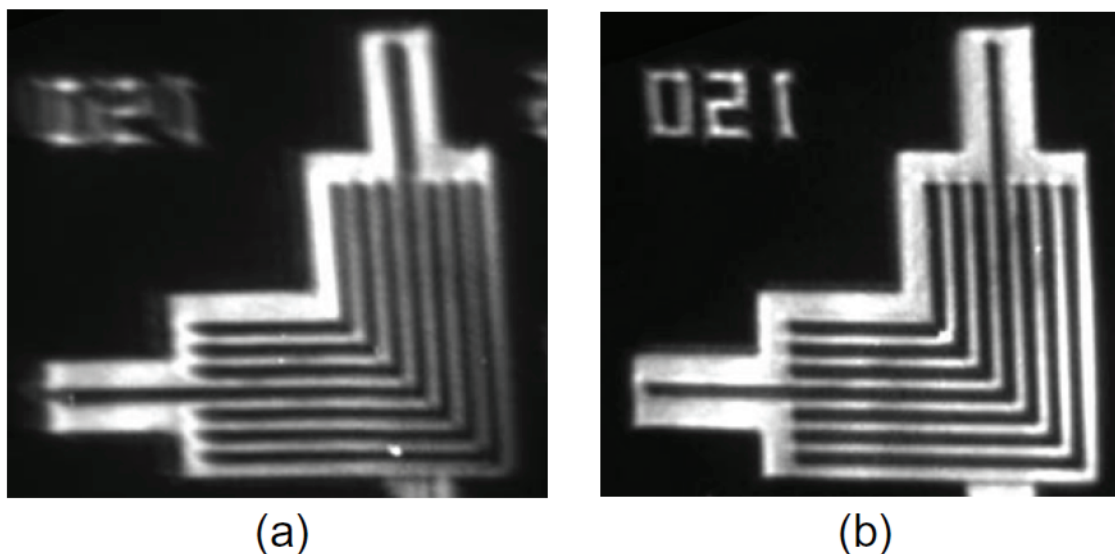


Fig. 9 EUVM images of 480-nm-hp elbow pattern. (a) before upgrading of imaging optics. (b) after upgrading of imaging optics (magnification: 600x).

3.3 Achievement of uniform illumination intensity

It was difficult to recognize the existence of phase defects from the intensity distribution on an EUVM image recorded using the static illumination as shown Fig. 10(a), because the signal of the defects is hidden by the noise that causes the nonuniform illumination intensity. This nonuniform illumination intensity distribution seems to be caused by the figure error of front-end mirrors. Then, in order to average a nonuniform illumination intensity distribution, the

front-end turning mirror [as indicated by (a) in Fig. 1] was scanned. A piezo actuator was employed for scanning a mirror.

A uniform illumination was successfully obtained after the front-end-turning-mirror scanning. Figures 10(a) and 10(b) show the EUVM images of a programmed bump defect of 160 nm width recorded by static illumination and scanning illumination. Figures 10(c) and 10(d) show the illumination intensity distributions along the imaginary lines

between two arrows in Fig. 10(a) and Fig. 10(b), respectively. By reducing noise intensity by a front-end-turning-mirror scanning method, the phase

defect signal was recognized clearly, as shown in Fig. 10(d).

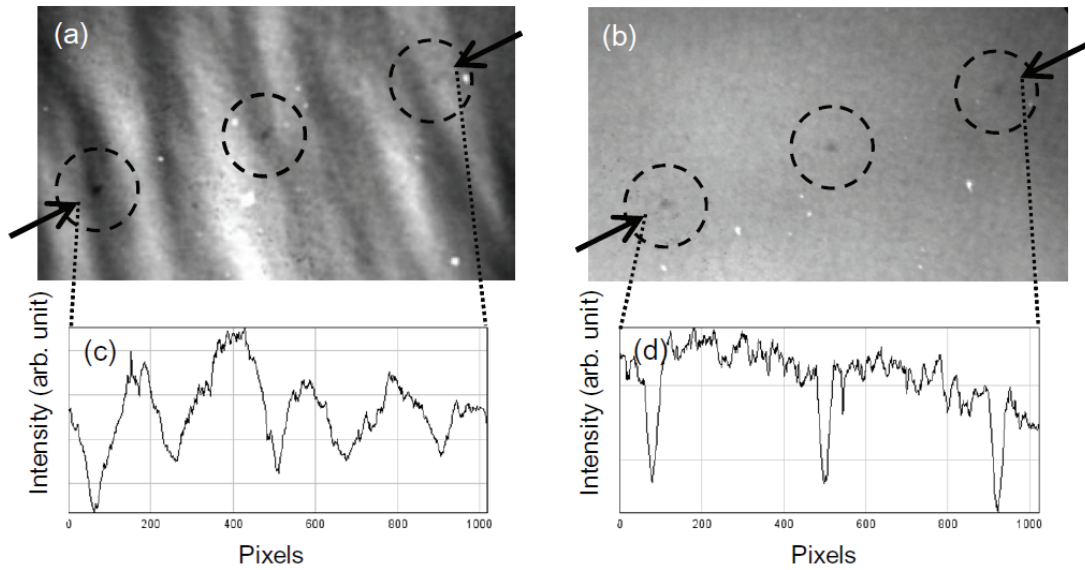


Fig. 10 EUVM images of programmed bump defect width of 160 nm size recorded with (a) static illumination and (b) scanning illumination. (magnification: 600x) (c) and (d) show the illumination intensity distributions along the imaginary lines between two arrows in (a) and (b) images.

4. Imaging performance of EUVM

After the improvement as described in § 3, the resolution and image contrast of line and space absorber patterns were evaluated. Figure 11 shows the images of 150-, 130-,120-, 110-, and 100-nm-hp patterns obtained by EUVM. Then, the contrast as shown Fig. 11, was calculated from the illumination

intensity distribution of the EUVM images. Although the resolution and contrast of the EUVM images were improved, the resolution and contrast were still not sufficient for the 22-nm-node requirement. Further studies are required for the improvements of resolution and contrast.

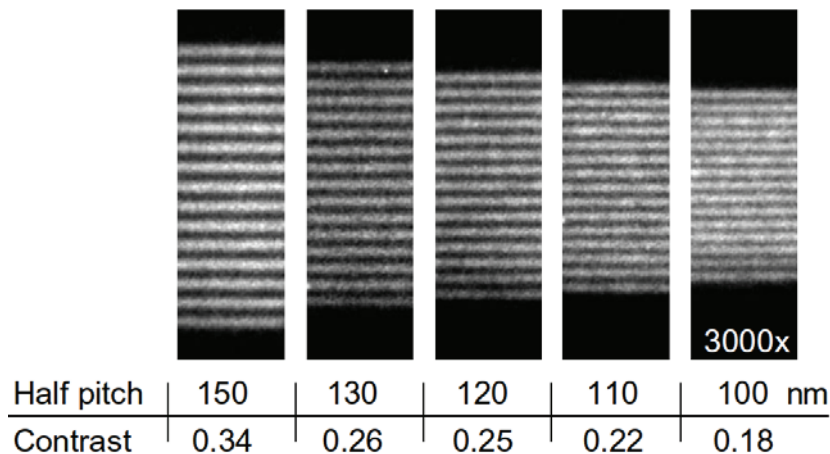


Fig. 11 EUVM images of 150, 130, 120, 110 and, 100-nm-hp patterns and there contrast values (magnification: 3000x).

5. Conclusions

EUVM images of high contrast at a high magnification were obtained using the cooling CCD camera. Wavefront aberrations were reduced and resolution was improved by employing a Mo/Si multiplayer-coated thick glass substrate of high surface accuracy on a back-end turning mirror and

good-alignment of Schwarzschild imaging optics. Utilizing a scanning system on a front-end turning mirror, the phase defect was recognized clearly in EUVM owing to reduction of background intensity noise. By these improvements EUVM image quality was improved.

References

- 1) International Technology Roadmap for Semiconductors (2004) : Lithography.
- 2) H. Kinoshita, K. Kurihara, Y. Ishii, and Y. Torii: J. Vac. Sci. Technol, **B7**(1989) 1648.
- 3) K. Hamamoto, Y. Tanaka, S. Y. Lee, N. Hosokawa, N. Sakaya, M. Hosoya, T. Shoki, T. Watanabe, and H. Kinoshita: J. Vac. Sci. Technol, **B23** (2005) 2852.
- 4) K. Hamamoto, Y. Tanaka, H. Kawashima, S. Y. Lee, N. Hosokawa, N. Sakaya, M. Hosoya, T. Shoki, T. Watanabe, and H. Kinoshita: Jpn. J. Appl. Phys. **44** (2005) 5474.
- 5) K. Hamamoto, Y. Tanaka, T. Yoshizumi, N. Hosokawa, N. Sakaya, M. Hosoya, T. Shoki, T. Watanabe, and H. Kinoshita: Jpn. J. Appl. Phys. **45** (2006) 5378.
- 6) K. A. Goldberg , A. Barty, Y. Liu, Y. Tezuka, T. Terasawa, J. S. Taylor, H. Han, and O. R. Wood: J. Vac. Sci. Technol, **B24** (2006) 2824.
- 7) Y. Kamaji, K. Takase, T. Yoshizumi, T. Sugiyama, T. Uno, T. Watanabe, and H. Kinoshita: Jpn. J. Appl. Phys. **48** (2009) 06FA07.
- 8) T. Liang, A. Stivers, R. Livengood, P.-Y. Yan, G. Zhang, and F.-C: Lo: J.Vac. Sci. Technol, **B18** (2000) 3216.
- 9) E. M. Gullikson, C. Cerjan, D. G. Stearns, P. B. Mirkarimi, and D. W. Sweeney: J. Vac. Sci. Technol, **B20** (2002) 81.
- 10) Lasertec DUV Mask Review Station MRS248 [<http://www.lasertec.co.jp/products/mrs248.html>].
- 11) T. Haga, H. Takenaka, and M. Fukuda: J. Vac. Sci. Technol, **B18** (2000) 2916.
- 12) T. Haga, H. Kinoshita, K. Hamamoto, S. Takada, N. Kazui, S. Kakunai, H. Tsubakino, and T. Watanabe, Jpn: J. Appl. Phys. **42** (2003) 3771.
- 13) H. Kinoshita, T. Haga, K. Hamamoto, S. Takada, N. Kazui, S. Kakunai, H. Tsubakino, T. Shoki, M. Endo, and T. Watanabe: J. Vac. Sci. Technol, **B22** (2004) 264.
- 14) T. Terasawa, Y. Tezuka, M. Ito, and T. Tomie: Proc. SPIE **5446** (2004) 804.
- 15) Y. Tezuka, M. Ito, T. Terasawa, and T. Tomie: Proc. SPIE **5446** (2004) 870.
- 16) A. Barty, Y. Liu, E. Gullikson, J. S. Taylor, and O. Wood: Proc. SPIE **5751** (2005) 651.
- 17) Y. Liu, A. Barty, E. Gullikson, J. S. Taylor, J. A. Liddle, and O. Wood: Proc. SPIE **5751** (2005) 660.
- 18) K. A. Goldberg, P. P. Naulleau, A. Barty, S. B. Rekawa, C. D. Kemp, R. F. Gunion, F. Salmassi, E. M. Gullikson, E. H. Anderson, and H.-S. Han: SPIE **6730** (2007) 67305E.
- 19) T. Terasawa, T. Yamane, T. Tanaka, T. Iwasaki, O. Suga, and T. Tomie: Jpn. J. Appl. Phys. **48** (2009) 06FA04.
- 20) Y. Tanaka, T. Watanabe, K. Hamamoto, and H. Kinoshita: Jpn. J. Appl. Phys. **45** (2006) 7163.
- 21) M. Osugi, K. Tanaka, N. Sakaya, K. Hamamoto, T. Watanabe, and H. Kinoshita: Jpn. J. Appl. Phys. **47** (2008) 4872.

Development of the Extreme Ultraviolet Interference Lithography System

*Yasuyuki Fukushima, Naoki Sakagami, Teruhiko Kimura,
Yoshito Kamaji, Takafumi Iguchi, Yuuya Yamaguchi, Masaki Tada,
Tetsuo Harada, Takeo Watanabe, and Hiroo Kinoshita

*Laboratory of Advanced Science and Technology for Industry, University of Hyogo,
3-1-2 Koto, Kamigori, Hyogo 678-1205, Japan*

e-mail: yasuyuki@lasti.u-hyogo.ac.jp

Extreme ultraviolet interference lithography was carried out at the long undulator beamline in NewSUBARU. It was confirmed that the spatial coherence length is 1.1 mm using a 10- μm -wide slit in the Young's double slit experiment. A 25-nm half pitch (hp) resist pattern was successfully replicated by extreme ultraviolet interference lithography (EUV-IL) utilizing a two-window transmission grating pattern of a 50-nm line and space (L/S). For the replication of a 20-nm L/S resist pattern by EUV-IL, we contrived a fabrication process that is suitable for a transmission grating pattern of 40-nm L/S and smaller. Employing a hard-mask process with a silicon dioxide (SiO_2) layer on a tantalum-nitride (TaN) layer in the fabrication of a two-window transmission grating, we successfully achieved five times larger dry-etch selectivity in comparison with a non-hard-mask process. As a result, we confirmed the ability this process to apply to a 40-nm hp grating.

1. Introduction

Extreme ultraviolet lithography (EUVL)¹⁾ is the most promising technology for a 22-nm half-pitch (hp) and it will be required for high-volume-manufacturing lithographic technology by the year 2013.²⁾ Resist materials and process technologies are two of the three top issues. In addition, according to the ITRS roadmap, EUVL is strongly predicted to be expanded to the 20-nm node by the year 2017 and to the 11-nm node by the year 2022. For the 20-nm node and the 11 nm-node, the requirements of line width roughness (LWR) are 0.8 nm (3σ) and 0.6 nm (3σ), respectively. Because the required size of LWR is smaller than the molecular size of a resist, a satisfying the LWR criterion is not easy. Thus,

because the development of resist material should be started earlier than the development of the EUV exposure alpha tool, extreme ultraviolet interference lithography (EUV-IL)³⁻¹²⁾ should be recognized as an important part in the evaluation of resist materials at 20-nm and smaller.

The EUVL interference exposure tool was installed at the BL-9 long undulator beamline in the NewSUBARU synchrotron radiation facility. The EUV-IL exposure tool including a two-window transmission grating was installed at the end station of the BL9C beamline. In this report, we focus on the coherence length measurement, exposure result, and fabrication process using a hard-mask process for a silicon dioxide (SiO_2) layer on a transmission grating.

2. Beamline Setup for EUV-IL in NewSUBARU

EUV-IL was constructed at the BL9 long undulator (LU) beamline in NewSUBARU. Figure 1 shows the beamline setup of the EUV-IL. An LU source spectrum with the peak at a specific wavelength can be obtained by tuning the gap between the magnets of the undulator.¹³⁾ Because the long undulator in NewSUBARU has a total length of 10.8 m and has 200 periods for high-brilliance radiation, the brilliance of EUV light with the undulator as a source is approximately 50,000 times higher than that with a bending magnet as a source.¹⁴⁾ To achieve a 20-nm L/S pattern and smaller on a wafer by EUV-IL, a

large spatial coherence length can be increased by enlarging the distance between the pinhole and the transmission grating. Thus, a large spatial coherence length and a low exposure time can be realized simultaneously by increasing the light intensity employing the long undulator. As described in §4, a spatial coherence length of more than 1 mm can be achieved. Figure 2 shows the light spectrum used in this experiment. The EUV light was focused on a pinhole using an optical component. At the pinhole position, the beam is focused to a size of 10 μm in the y -direction. Because the distance from the pinhole to the resist is maintained at approximately 3.3 m and

the high wavelength range beyond 20 nm is removed by a 0.2- μm -thick zirconium (Zr) filter, the light is

monochromated with a wavelength of 13.4 nm on the resist sample.

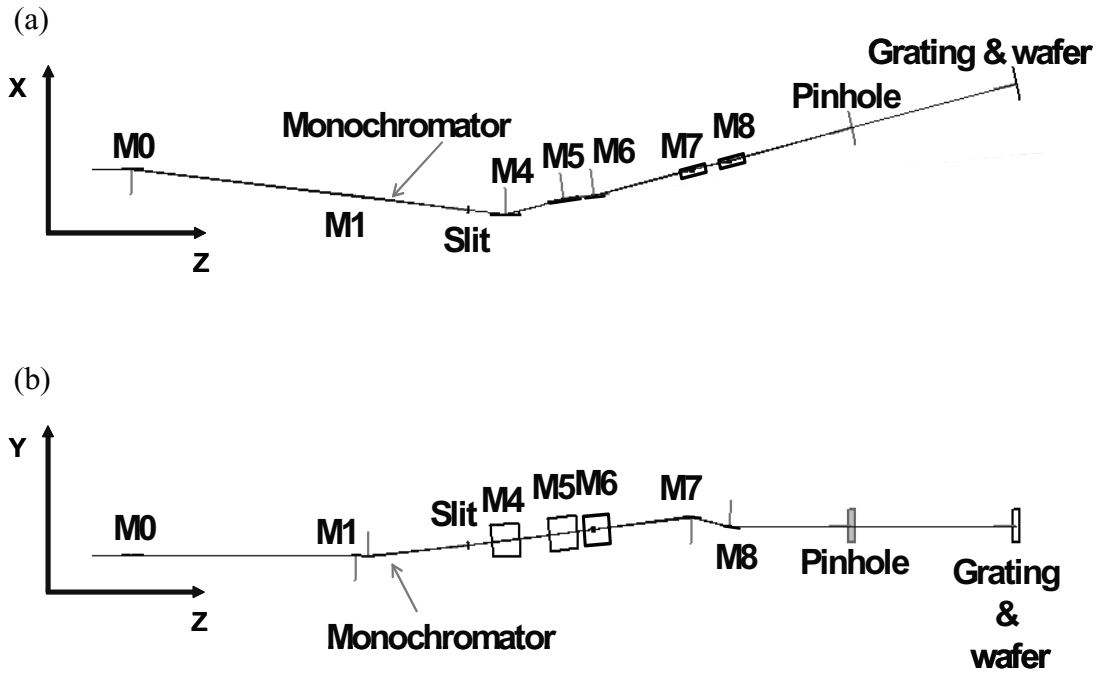


Fig. 1. BL9 beamline setup of EUV-IL: (a) top view and (b) side view.

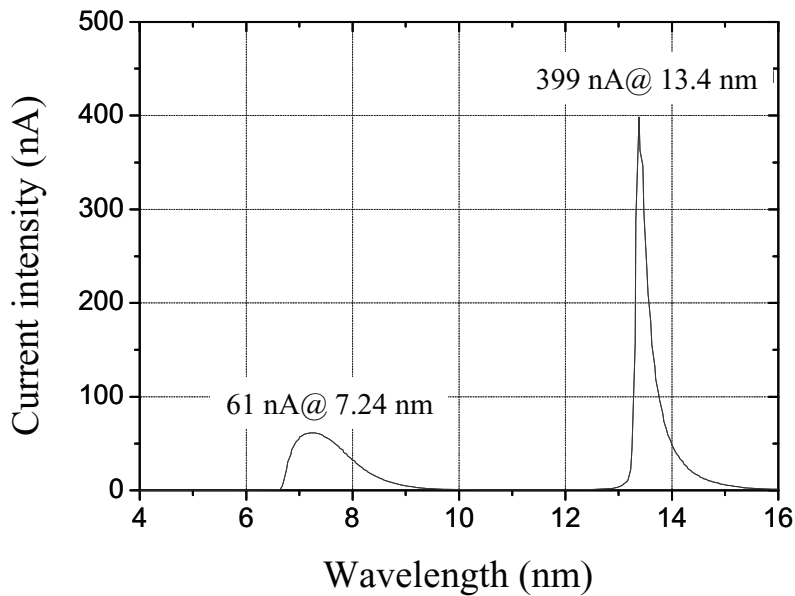


Fig. 2. Spectrum of long undulator at the BL9 beamline used for EUV-IL.

3. Principle of EUV

Figure 3 shows the principle of EUV-IL. In the dual beam interference system, double periodic interference fringes are created at a position fitting two phases when the +1st order ray diffracted from one window of the grating interferes with the -1st

order ray diffracted from another window of the grating. The diffraction condition of the grating can be expressed as $m\lambda = d(\sin \theta_f - \sin \theta_i)$, where m , d , θ_f , and θ_i are the number of the diffraction order, the pitch size of the grating pattern, the angle of transmitted light, and the angle of

incident light, respectively. In addition, the pitch size of interference fringes p is expressed as $p = \lambda / (2 \sin \theta)$, where θ is half of the angle between the propagating directions of the two beams of the +1st and -1st diffraction orders. Considering normal incident light, an incident light angle may be expressed as $\theta_i = 0$. Then, the pitch size of interference fringes p is expressed as $p = d / 2$. Thus, the half-size of the grating pattern size can be replicated on a wafer. In EUV-IL the distance

between the two windows has to be smaller than the coherence length. In addition, if the grating pitch pattern d becomes smaller, the diffraction angle θ_f of the -1st and +1st diffraction orders becomes larger. If the distance between two windows of a transmission grating is constant, the distance between the grating and the wafer becomes smaller. Thus, a larger coherence length may relax the distance between the grating and the wafer.

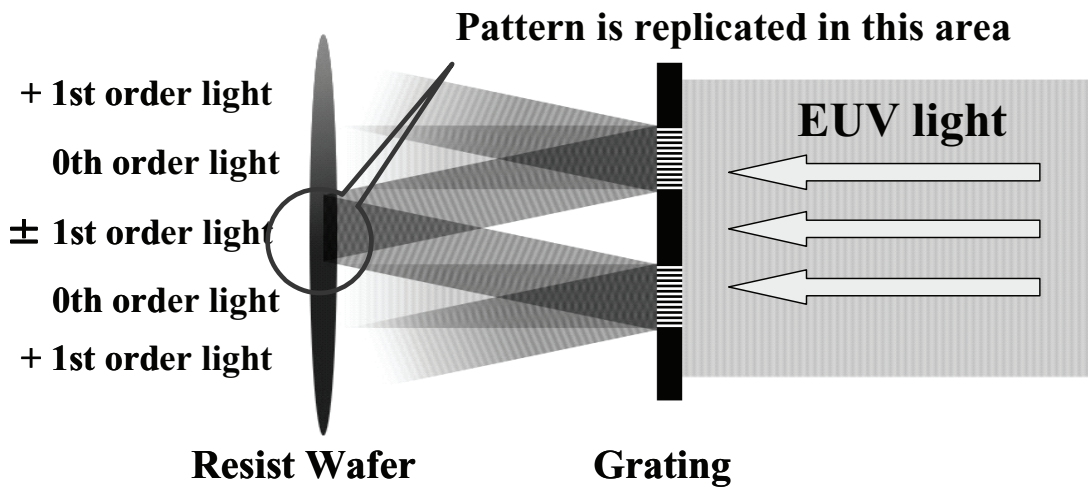


Fig. 3. Principle of EUV interference lithography.

4. Spatial Coherence Measurement

The spatial coherence of the light source can be determined by Young's double slit experiment. Figure 4 shows the experimental setup for the spatial coherence measurement.^{15, 16} The distance between the single slit and the double slit was 0.9 m, and the distance between the double slit and the photodiode installed in the exposure chamber was 2.4 m. The light intensity was measured by changing the

photodiode position in the vertical direction, as shown in Fig. 4(b). Two single slits of 3 mm (horizontal) \times 25 μ m (vertical) in size and 3 mm (h) \times 10 μ m (v) in size were prepared. The size of each slit in the double slit was 3 mm (h) \times 25 μ m (v). Four double slits with separations of 40, 160, 320, and 640 μ m were prepared for Young's double slit experiment.

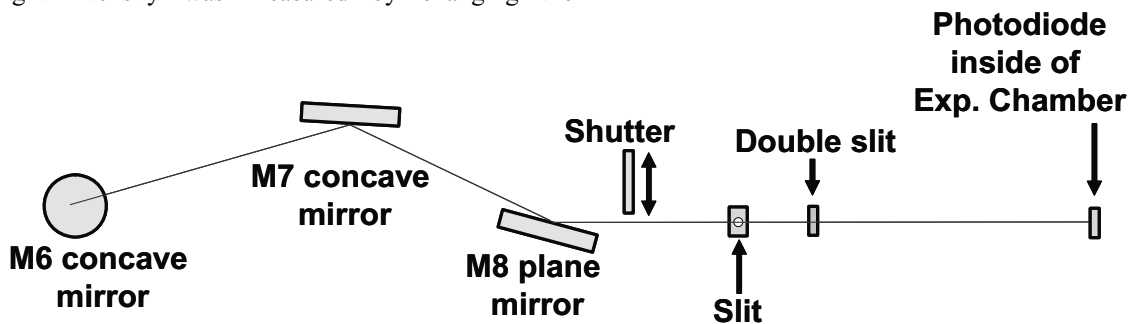


Fig. 4. Experimental setup for spatial coherence measurement.

The spatial coherence was calculated by the following method. The contrast of the spatial coherence is expressed as $Contrast = \exp(-d_s^2 / 2R_c^2)$, where $R_c (= 2 \times l_c)$, l_c , and d_s are the coherence radius, the spatial coherence length at the double slit position, and the double slit separation, respectively. The spatial coherence length is defined for the condition where $Contrast = 0.88$. Furthermore, the measured value of $Contrast$ is expressed as $Contrast = (I_{max} - I_{min}) / (I_{max} + I_{min})$, where I_{min} and I_{max} are the minimum photodiode current and the maximum photodiode current, respectively. When the distance between the single slit and the double slit and the distance between the double slit and the photodiode are taken into account, the spatial coherence length (L_c) at the grating position is expressed as $L_c = 2.4 \times l_c / 0.9$.

Figures 5(a), 5(b), and 5(c) show the results of light intensity measurements using a 25- μm slit with double slit separations of 40, 160, and 320 μm , respectively. In addition, Fig. 5(d) shows the result of light intensity measurements using a 10- μm slit with a double slit separation of 640 μm . In this figure, the vertical axis is the measured current from a photodiode, and the horizontal axis is the distance to the double slit in the y -direction. $Contrast$ can be obtained using eq. (5) by substituting the maximum and minimum values obtained from these graphs. Figure 6 shows results. The vertical axis is normalized $Contrast$, and the horizontal axis is the double slit separation. Using 25- μm and 10- μm single slits, the spatial coherence lengths (l_c) at the double slit position were 204 and 440 μm , respectively. Thus, it was confirmed that spatial coherence (L_c) using a 25- μm slit and a 10- μm slit was 544 and 1173 μm at the transmission grating position, respectively. As a result, a large spatial coherence length was achieved for replicating a 20-nm L/S pattern and smaller.

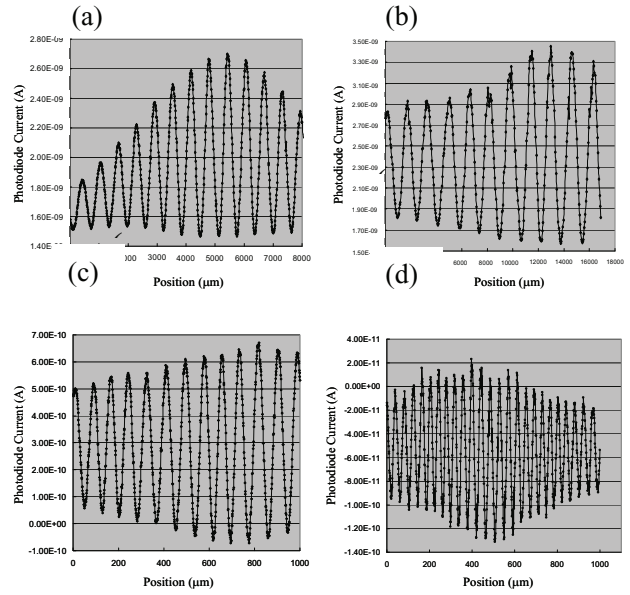


Fig. 5. Examples of light intensity measurement at the grating position: (a) slit width 25 μm and double slit separation 40 μm , (b) slit width 25 μm and double slit separation 160 μm , (c) slit width 25 μm and double slit separation 320 μm , and (d) slit width 10 μm and double slit separation 640 μm .

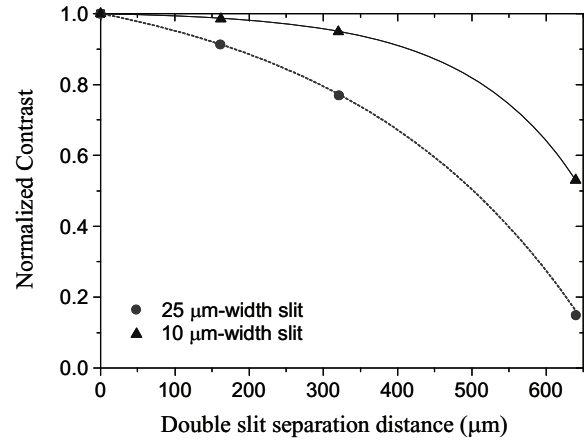


Fig. 6. Results of spatial coherence length measurement.

5. Resist Patterning by EUV-IL

25 nm hp resist pattern was replicated by EUV-IL using the 100-nm-pitch transmission grating. A wafer stage and a grating stage were installed in the EUV-IL exposure chamber. The wafer stage consists of x -, y -, and z -stages and a tilt stage. The grating stage consists of x - and y - stages and a tilt stage. Using these stages, the light axis was adjusted. A nonchemically amplified resist ZEP520A was spin-coated on a 4-in. wafer. The resist thickness was

50 nm, and the prebake was carried out at 180 $^{\circ}\text{C}$ for 180 s. The exposure conditions were as follows: using a 25- μm (vertical) slit, the distance between the wafer and the transmission grating was 250 μm , the current was 560 nA after transmission grating, and the exposure time was 12 s. Development was carried out at 23 $^{\circ}\text{C}$ for 90 s with o-xylene, and the wafer was rinsed at 23 $^{\circ}\text{C}$ for 30 s with isopropyl alcohol.

Figure 7 shows a photograph of a replicated ZEP520A resist pattern of a 34-nm line and a 16-nm

space (25-nm hp) pattern observed using a critical dimension scanning microscope (CD-SEM; Hitachi S8840). In the near future, various types of

chemically amplified resist will be evaluated. In addition, in future studies, we will approach replicating 20-nm hp resist patterns and smaller.

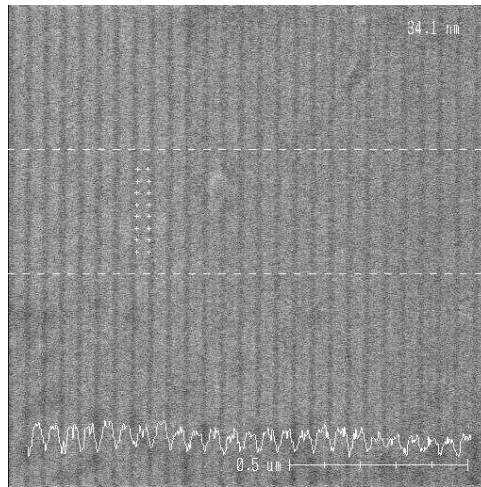


Fig. 7. SEM image of replicated ZEP520A resist pattern of a 25-nm hp.

Using a two-dimensional transmission grating, as shown in Fig. 8(a), with a four-beam diffraction, a dot or hole pattern can be replicated. In this case, for a 50-nm L/S grating pattern, a 35-nm hp dot resist pattern was replicated, as shown in Fig. 8(b). The

resist was ZEP520A. The resist thickness was 50 nm. The resist development and rinse conditions were the same as those used in replicating the L/S resist pattern.

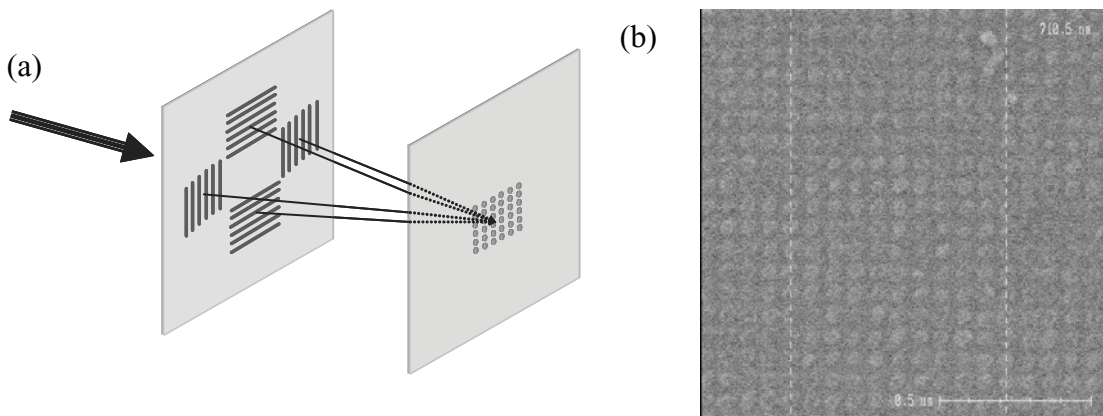


Fig. 8. (a) Configuration of two-dimensional transmission grating and (b) SEM image of replicated ZEP520A resist pattern of 35-nm hp dot resist pattern.

6. Transmission Grating Fabrication by Applying a Hard-Mask Process

The fabrication of a transmission grating¹⁷⁾ is a key technology for EUV-IL. For replicating resist patterns of 20-nm hp and smaller, it is necessary to make a transmission grating of a 40-nm L/S pattern. Figure 9 shows the fabrication of a transmission grating. A 4-in. silicon wafer coated on both sides with a silicon nitride (Si_3N_4) layer in 300 nm thick was prepared. The transmittance of a 300-nm-thick

Si_3N_4 layer is 7.4%. For the grating absorber, a TaN layer with 70 nm thick was coated on a Si_3N_4 layer, which has a good absorbance of 99.6% for EUV light.¹⁸⁾ Considering the dry-etch selectivity between a resist and TaN, to fabricate 30-nm and 40-nm L/S TaN patterns with 70 nm thick, the resist should be 200 nm thick. Therefore, it is impossible to make 30- and 40-nm L/S resist patterns with 200 nm thick, because the resist pattern collapses. On the other hand, if a 20-nm-thick silicon dioxide (SiO_2) layer is

deposited on a TaN layer used for a hard-mask process, the required thickness of the resist is about 60 nm. The dry-etch selectivity of a resist and of TaN was approximately 0.32. However, in the case of using a hard-mask process for a SiO₂ layer, the dry-etch selectivity of the resist and the TaN was approximately 1.7. The dry-etch selectivity of the resist and the TaN is improved fivefold by employing a hard-mask process.

TaN and a SiO₂ layers are deposited on a Si₃N₄ layer using a magnetron sputtering system. As a result, it is possible to make a 40-nm L/S grating pattern and smaller using two metal layers that have greatly different dry-etch rates, as shown in Fig. 10. A ZEP520A resist was spin-coated on a wafer, and a resist pattern was replicated by electron beam (EB) lithography. The resist pattern was transferred to a SiO₂ layer by an inductively coupled plasma (ICP) dry-etch system (TCP9400SE, Lam Research) assisted by a fluorocarbon (CF₄) gas. The etch condition of assisted-gas flow-rate, ICP radio-frequency (RF) power, and bias power are 60 sccm, 100 W, and 25 W, respectively. A SiO₂ pattern was transferred to a TaN layer by an ICP dry-etch

method assisted by chlorine (Cl₂) gas. The etch conditions of assisted-gas flow-rate, ICP RF power, and bias power are 25 sccm, 100 W, and 25 W, respectively. As shown in Fig. 10(b), because the etching selectivity between a ZEP520A resist and a SiO₂ layer was 0.51, and that between SiO₂ and TaN was 3.4, the selectivity between a ZEP520A resist and a TaN layer was 1.7. Thus, as shown in Fig. 10, the etch selectivity between a ZEP520A resist and a TaN layer using a hard-mask process is five times larger than that using a non-hard-mask process. A backside Si₃N₄ layer of a desired aperture was removed by a reactive-ion-etch (RIE) method assisted by CF₄ gas using a metal mask. The silicon substrate of a desired aperture was removed by a wet-etch process using an aqueous solution of potassium hydroxide (KOH) at a temperature of 80 °C.¹⁹⁾ Figure 11(a) shows a photograph of a finished TaN transmission grating on a 4-in. Si wafer after a wet-etch process. Nine transmission gratings can be fabricated per wafer. Using this method, because a 60-nm L/S grating pattern was successfully formed, as shown in Fig 11(b), we will try to make a 40-nm L/S grating pattern in the next stage.

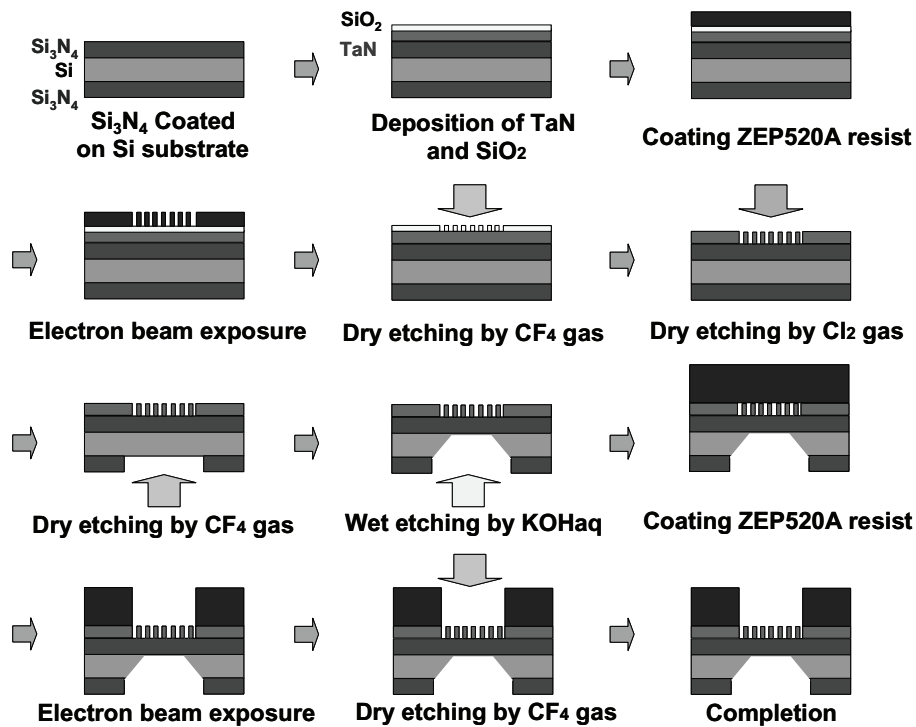


Fig. 9. Fabrication of a transmission grating.

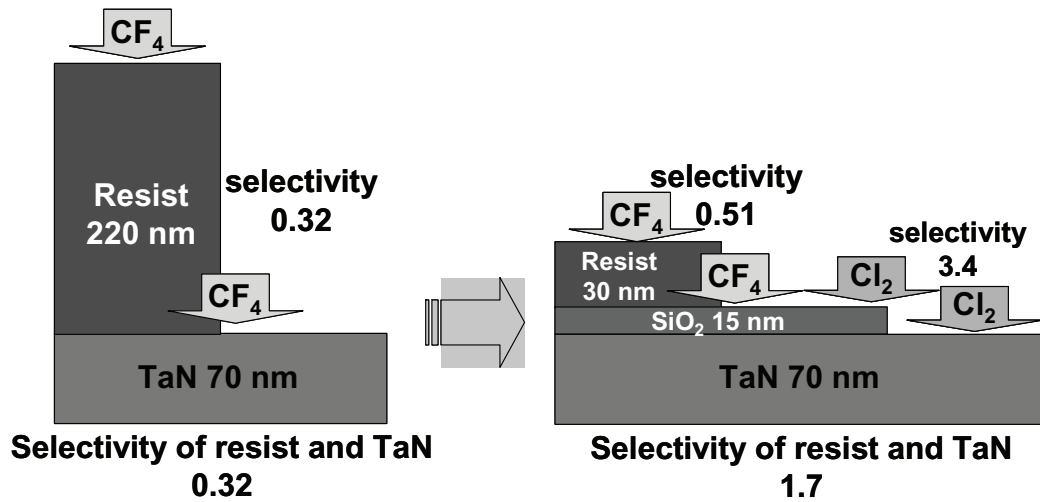


Fig. 10. Dry-etching selectivities of SiO_2 and TaN.

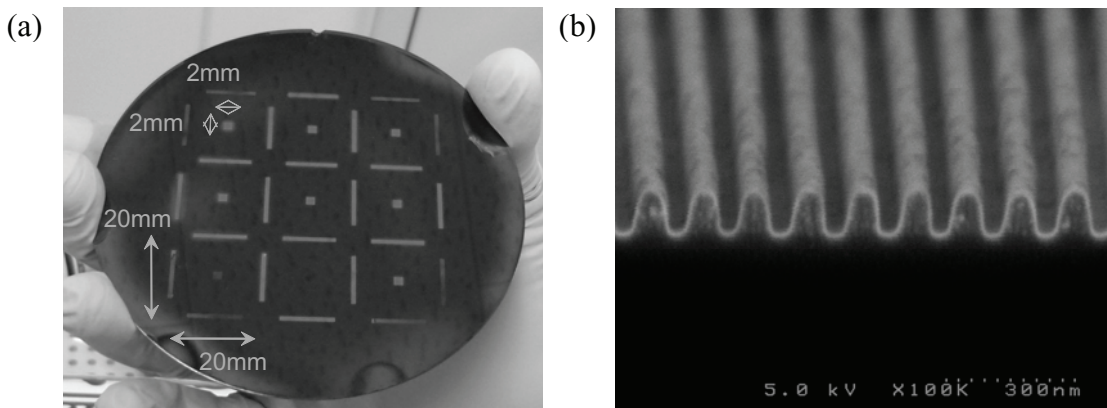


Fig. 11. (a) Photograph of a finished TaN transmission grating on a 4-in. silicon wafer after wet-etching, and (b) SEM image of the cross-sectional view of a 60-nm L/S grating pattern.

Furthermore, to improve the contrast of the interference fringes, the intensity of EUV light transmitted from outside a TaN grating patterned area has to be reduced with an additional resist absorber layer. Thus, a 1- μm -thick ZEP520A resist was spin-coated on a TaN grating pattern, but only the TaN grating patterned area was exposed by the EB writing tool. After the development of the resist, the

residual resist on the TaN grating pattern was removed completely by a CF_4 dry-etch process. Thus, 70-nm-thick TaN and a 1- μm -thick resist were used as an additional absorbers for the outside of a TaN grating patterned area, which has a total absorbance of 99.998% including the TaN and the additional resist layer of ZEP520A.

7. Conclusions

Extreme ultraviolet interference lithography was carried out at the long undulator beamline in NewSUBARU. It was confirmed in Young's double slit experiment that the spatial coherence length is 1.1 mm using a 10- μm -wide slit. A 25-nm half-pitch (hp) resist pattern was successfully replicated by EUV-IL utilizing a two-window transmission grating pattern

with a 50-nm line and space (L/S). For the replication of a 20-nm L/S resist pattern and smaller by EUV-IL, we developed a fabrication process suitable for a transmission grating pattern of 40-nm L/S and smaller. Employing a hard-mask process using a silicon dioxide (SiO_2) layer on a tantalum-nitride (TaN) layer in the fabrication of a two-window transmission grating, a fivefold larger dry-etch

selectivity in comparison with the non-hard-mask process was successfully achieved. As a result, we

confirmed the ability to apply this method to a 40-nm hp grating.

Acknowledgment

We would like to thank the Japan Society for the Promotion Science for the Grant-in-Aid for Scientific Research.

References

- 1) H. Kinoshita, K. Kurihara, Y. Ishii, and Y. Torii: *J. Vac. Sci. Technol. B* **7** (1987) 1648.
- 2) ITRS Road map: <http://www.itrs.net/>.
- 3) H. H. Solak, D. He, W. Li, S. Singh-Gasson, F. Cerrina, B. H. Sohn, X. M. Yang, and P. Nealey: *Appl. Phys. Lett.* **75** (1999) 2328.
- 4) H. H. Solak, C. David, J. Gobrecht, V. Golovkina, F. Cerrina, S. O. Kim, and P. F. Nealey: *Microelectron. Eng.* **67** (2003) 56.
- 5) M. Wei, D. T. Attwood, and T. K. Gustafson: *J. Vac. Sci. Technol. B* **12** (1994) 3648.
- 6) P. P. Naulleau, C. N. Anderson, and S. F. Horne: *Proc. SPIE* **6517** (2007) 65172T.
- 7) H. H. Solak: *J. Phys. D: Appl. Phys.* **39** (2007) R171.
- 8) H. Shiotani, S. Suzuki, D. Gun Lee, P. Naulleau, Y. Fukushima, R. Ohnishi, T. Watanabe, and H. Kinoshita: *Jpn. J. Appl. Phys.* **47** (2008) 4881.
- 9) H. H. Solak, D. He, W. Li, and F. Cerrina: *J. Vac. Sci. Technol. B* **17**(6) (1999) 3052.
- 10) S. Suzuki, Y. Fukushima, R. Ohnishi, T. Watanabe, and H. Kinoshita: *J. Photopolym. Sci. Technol.* **21** (2008) 435.
- 11) Y. Ekinci, H. H. Solak, C. Padeste, J. Gobrecht, M. P. Stoykovich, and P. F. Nealey: *Microelectron. Eng.* **84** (2007) 700.
- 12) A. Isoyan, Y.-C. Cheng, F. Jiang, J. Wallace, M. Efremov, P. Nealey, and F. Cerrina: *Proc. SPIE* **6921** (2008) 69212R.
- 13) D. T. Attwood, P. Naulleau, K. A. Goldberg, E. Tejnil, C. Chang, R. Beguiristain, P. Batson, J. Bokor, E. M. Gullikson, M. Koike, H. Medeck, and J. H. Underwood: *IEEE J. Quantum Electron.* **35** (1999) 709.
- 14) S. Hashimoto, A. Ando, M. Nibe, S. Miyamoto, Y. Shoji, Y. Fukuda, T. Tanaka, and Y. Gomei: *Nucl. Instrum. Methods Phys. Res., Sect. A* **467** (2001) 141.
- 15) Y. Nagata, K. Furusawa, Y. Nabekawa, and K. Midorikawa: *Opt. Lett.* **32** (2007) 722.
- 16) H. F. Schouten, T. D. Visser, and E. Wolf: *Opt. Lett.* **28** (2003) 1182.
- 17) P. P. Naulleau, C. H. Cho, E. M. Gullikson, and J. Bokor: *J. Synchrotron Radiat.* **7** (2000) 405.
- 18) <http://www-cxro.lbl.gov/>
- 19) K. Sato, M. Shikida, Y. Matsushima, T. Yamashiro, K. Asaumi, Y. Iriye, and M. Yamamoto: *Sens. Actuators A* **64** (1998) 87.

High-Precision Analysis for Material Analysis Beamline at BL05 for Industrial Enterprises

T. Hasegawa¹, M. Uemura¹, M. Motoyama², S. Matsui² and K. Kanda²
1 Synchrotron Analysis L.L.C., Hyogo-ku, Kobe, Hyogo 652-0863 Japan
2 University of Hyogo, Kamigori, Ako, Hyogo 678-1205 Japan

Abstract

A material analysis beamline for the industrial enterprises' use was completed at BL05 in March 2008. BL05 consists of two branch lines, one is a double crystal monochromator beamline (BL05A) for the use in the higher-energy region (1300-4000 eV) and the other is a varied line spacing plane grating (VLSPG) monochromator beamline (BL05B) for the use in the lower-energy region (50-1300 eV), which cover the whole energy range of the soft X-ray region from 50 eV to 4000 eV. These two branch lines can be operated simultaneously. The X-ray absorption fine structure (XAFS) measurements in the total electron yield (TEY) and fluorescence yield (FLY) can be performed at BL05A and BL05B. In addition, the X-ray photoelectron spectra (XPS) can be measured at BL05B.

Introduction

Recently, the needs for material analysis in the soft X-ray region using synchrotron radiation has increased in the analysis industry. A material analysis beamline for the industrial enterprises' use was completed at BL05 in March 2008. The whole useful energy range of the BL05 is the soft X-ray region from 50 to 4000 eV and X-ray absorption spectrum can be measured with a high-energy resolution. BL05 will be managed and maintained by the Synchrotron Analysis L.L.C. (SALLC), which is composed of the industrial companies, in cooperation with the staffs of the Laboratory of Advanced Science and Technology for Industry in University of Hyogo. Industrial users can be assisted by staffs of SALLC in the measurement at BL05. In this paper, we will introduce BL05 and report recent activities.

Layout of BL05

Bending magnet beamline BL05 consists of two branch lines (BL05A, BL05B) for the use in the wide range from 50 eV to 4000 eV. Photo.1 shows a photograph of BL05. BL05A, which is mounted with a double crystal monochromator, can be used in the energy range of 1300-4000 eV by exchanging several monochromatizing crystals. On the other hand, BL05B is mounted with a varied line spacing plane grating (VLSPG) monochromator, which is designed to cover the energy range 50-1300 eV with three gratings. Because the incident beam from the bending magnet is provided for two branch lines through the different windows of mask, these lines can be operated simultaneously.

Specifications of BL05A

Toroidal mirrors are used as a pre-mirror and a focusing mirror of BL05A, for the purpose to introduce a high-photon flux to the end station. InSb (111) crystals and Si (111) crystals are prepared for a Golovchenko-type double crystal monochromator. The XAFS measurements in the total electron yield

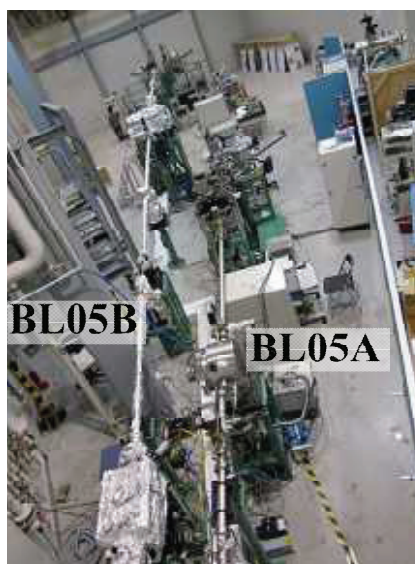


Photo.1 Photograph of beamline BL05.

(TEY) and fluorescence yield (FLY) using SDD (SII, Vortex) can be performed. The fluorescence XAFS spectra can be measured samples at the under an atmospheric pressure by the replacement of an end station to He using Be window. The chamber can maintain 8 samples of 25 mm corner because of industrial use.

Specifications of BL05B

The constant-deviation monochromator consisting of a demagnifying spherical mirror and VLSPG, which can provide to high resolution, simple wavelength scanning with fixed slits, was mounted on BL05B. The including angle of the monochromator is 175°. VLSPG consists of three gratings (100-, 300- and 800-lines/mm). Fig.1 shows a calculated diffraction efficiency of each grating. Expected resolution ($E/\Delta E$) is 3,000. Two

measurement chambers are prepared at the end station of BL05B. The XAFS spectra in the total electron yield and fluorescence XAFS spectra using SSD (EDAX) can be measurement in the high vacuum chamber. In addition, the X-ray photoelectron spectra (XPS) using spherical electron analyzer (VG Scienta, R3000) can be measured in the ultra high vacuum chamber. These chambers can be replaced each other within 1 hour. Each chamber can maintain 16 samples of 25 mm corner.

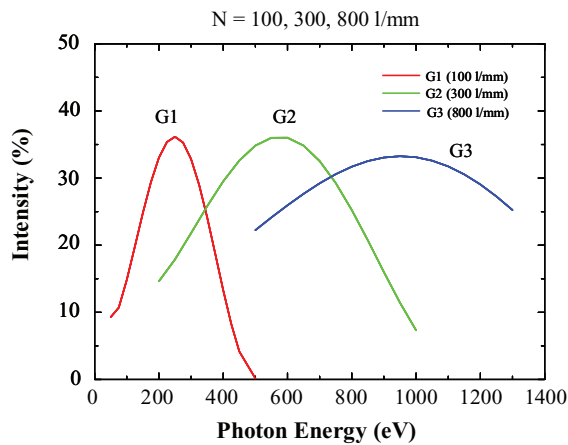


Fig.1 Diffraction efficiency of BL05B.

Measurement

We measured standard samples by means of the TEY method at BL05B and obtained absorption spectra in each grating, 100- or 300- or 800-lines/mm. Fig.2-4 show boron K-edge, calcium and nickel $L_{3,2}$ -edge near-edge X-ray absorption fine structure (NEXAFS) spectra of *h*-BN, CaF_2 powder and Ni sheet. The spectrum have been normalized to I_0 and had a linear pre-edge background removed. For *h*-BN, an intense peak at 191 eV appeared clearly in Fig.3, which is assigned to transition from $B1s$ to the

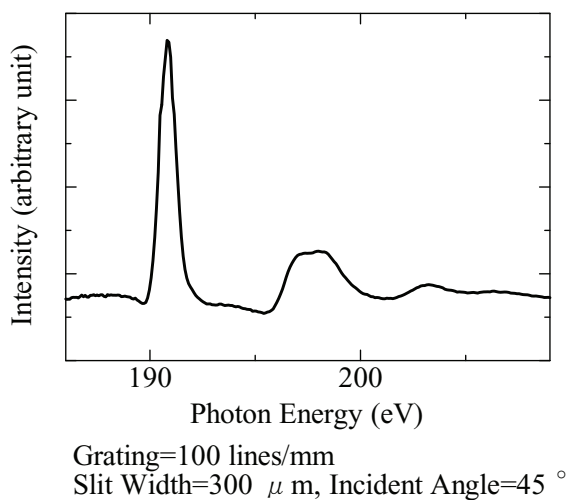


Fig.2 *h*-BN B K-edge NEXAFS spectrum.

unoccupied $B2p \pi^*$, the spectrum was the same shape as the one Jiménez et al. reported [1]. Additionally, the calcium $L_{3,2}$ -edge spectral shape of CaF_2 almost corresponds to the spectrum reported by Naftel et al. [2]. The nickel $L_{3,2}$ absorption peaks are observed at 853 and 871 eV, respectively [3].

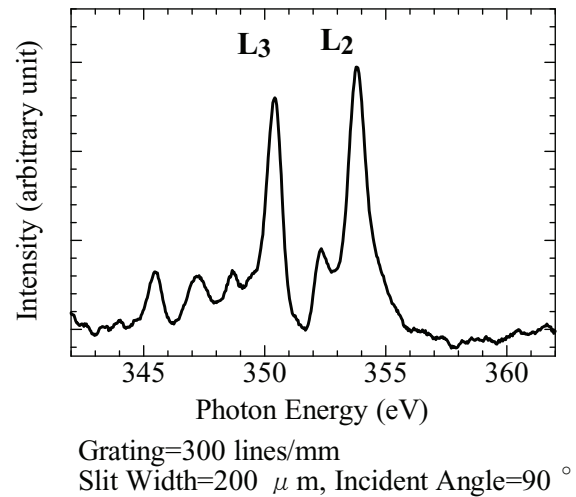


Fig.3 CaF_2 Ca $L_{3,2}$ -edge NEXAFS spectrum.

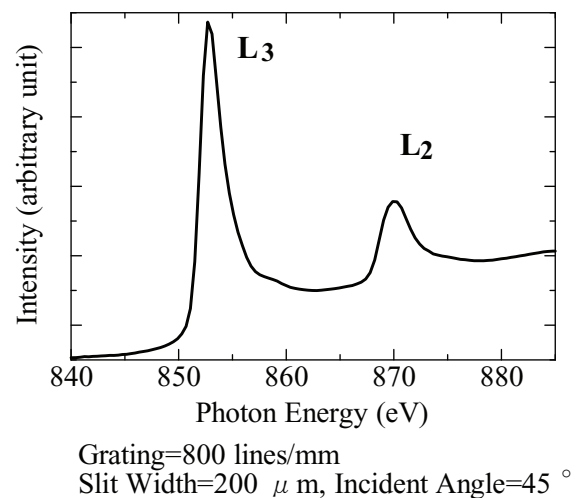


Fig.4 Ni $L_{3,2}$ -edge NEXAFS spectrum.

References

- [1] I.Jiménez, A.F.Jankowski, L.J.Terminello, D.G.J. Sutherland, J.A.Carlisle, G.L.Doll, W.M.Tong, D.K. Shuh, F.J.Himpsel: *Phys. Rev.*, **B55**, 12027 (1997).
- [2] S.J.Naftel, T.K.Sham, Y.M.Yiu, B.W.Yates: *J. Synchrotron Rad.*, **8**, 255 (2001).
- [3] J.A.Bearden, A.F.Burr: *Rev. Mod. Phys.*, **39**, 125 (1967).

Effect of the Soft X-ray on the Highly-Hydrogenated Diamond-Like Carbon Film

Kazuhiro Kanda¹, Kumiko Yokota², Masahito Tagawa², Mayumi Tode³, Yuden Teraoka³, Shinji Matsui¹
¹Laboratory of Advanced Science and Technology for Industry, University of Hyogo, ² Graduate School of Engineering, Kobe University, ³ Japan Atomic Energy Agency
E-mail: kanda@lasti.u-hyogo.ac.jp; Tel.: +81-791-58-0476

Abstract

Hydrogen was found to emit from the highly-hydrogenated Diamond-Like Carbon (H-DLC) films by the irradiation of synchrotron radiation (SR) even in the vacuum. The hydrogen content in the H-DLC film decreased exponentially with a soft X-ray exposure dose. In addition, the decrement of hydrogen content was found to decrease with increasing of the initial hydrogen content in the H-DLC film. It was interpreted that the etching rate of H-DLC increased with its hydrogen content.

Introduction

Diamond-Like Carbon (DLC) films generally have durability against the synchrotron radiation (SR) in the absence of oxygen gas.¹⁾ Recently, hydrogen was emitted from the highly-hydrogenated DLC (H-DLC) films by the irradiation of soft x-ray even in the vacuum, and increase in the film density, hardness and refractive index were reported.²⁾ In the present study, we investigated the departure process of hydrogen from the highly-hydrogenated DLC film by the exposure to soft X-ray in the vacuum using three kinds of highly-hydrogenated DLC thin films, which contained difference hydrogen contents.

Experiments and Results

Highly-hydrogenated DLC thin films were deposited on Si wafer with 200 nm thickness by amplitude-modulated RF plasma-CVD method.³⁾ We called these films H-DLC50, H-DLC40 and H-DLC30, in order of hydrogen content. The irradiation of SR against DLC films was carried out at BL-6 of NewSUBARU.⁴⁾ The SR at the BL-6 sample stage had a continuous spectrum from IR to soft X-ray, which was lower than 1 keV. Rutherford backscattering spectrometry (RBS) and elastic recoil detection analysis (ERDA) are available for evaluating quantitative determination for all elemental composition, specially hydrogen, of thin films with high accuracy, being unnecessary for standard samples. In this study, the hydrogen content of DLC film has been determined by RBS and ERDA techniques using a tandem Pelletron accelerator, SSDH-2 in the Kobe University. Figure 1 depicts the SR dose dependences of hydrogen content estimated using ERDA/RBS techniques. The hydrogen content in the low-hydrogenated DLC film kept constant independent on a soft X-ray exposure dose. On the other hand, that in the high-hydrogenated DLC film decreases exponentially with a soft X-ray exposure dose. Thus, the departure of the hydrogen was observed from high-hydrogenated DLC films, while was not observed from the low-hydrogenated DLC film by soft X-ray irradiation. The mechanism of the departure process of hydrogen from DLC film by SR

exposure was discussed on the basis of the measurements of etching depth and thermal desorption spectra.

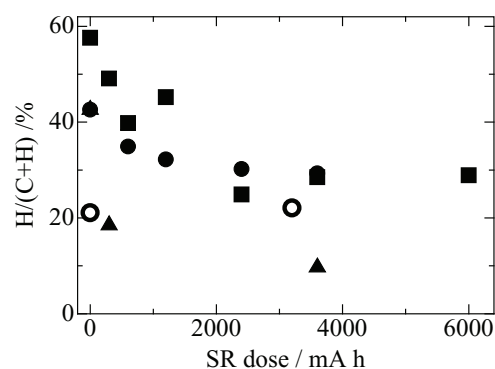


Fig. 1 The SR dose dependences of the hydrogen content. Circle, square, and triangle indicate H-DLC50, H-DLC40 and H-DLC30 respectively. Open circle indicates low hydrogenated DLC film synthesized using PBII/D method.

References

- [1] H. Kyuragi and T. Urisu, *Appl. Phys. Lett.*, **50** (1987) 1254
- [2] H. Matsuura, et. al., *SEI Technical Review*, **171** (2007) 39 (Japanese)
- [3] T. Nakahigashi, et. al., *Tribology International*, **37** (2004) 907
- [4] K. Kanda, et. al., *Jpn. J. Appl. Phys.*, **42** (2003) 3983

Acknowledgements: A part of this work was supported by the New Energy and Industrial Technology Development Organization (NEDO) under the work entitled “Advanced Fundamental Research Project on Hydrogen Storage Materials”. We also thank to use SSDH-2 of Accelerator and Particle Beam Experimental Facility, Faculty of Maritime Sciences, Kobe University for the RBS measurement.

Photoemission Study of Hydrogenated Amorphous Carbon Thin Films as a Function of Annealing Temperature

Yuichi Haruyama¹, Masahito Tagawa², Kumiko Yokota², and Shinji Matsui¹
¹ Laboratory of Advanced Science and Technology for Industry, University of Hyogo
² Graduate School of Engineering, Kobe University

Abstract

The electronic structure in hydrogenated amorphous carbon (a-C:H) thin films was investigated as a function of the annealing temperature using photoemission spectroscopy. The photoemission results of the valence band and the C 1s core level suggested that the graphitization of the a-C:H film proceeds by annealing at more than 400 °C. From the photoemission spectra of the C 1s core level, the coordination of C atoms in the a-C:H film were evaluated as a function of the annealing temperature. Based on the evaluations, the electronic structure of the a-C:H film as a function of the annealing temperature is discussed.

Introduction

Since amorphous carbon thin films have interesting properties such as high hardness, low friction coefficient, and chemical inertness, the study of amorphous carbon thin films has attracted a great deal of attention for wide applications [1-2]. Due to their properties, amorphous carbon films are mainly used in industrial products as coatings for the magnetic heads and media of hard disk drives, the machine parts for mold, the cutting tools, etc. In order to produce good amorphous carbon films, various vapor phase methods have been extensively attempted so far, and the properties of the hydrogenated amorphous carbon (a-C:H) films formed by vapor phase methods have been studied. In the previous studies using Raman and Auger electron spectroscopy, the a-C:H films were thermally stable up to 260 °C. However, it was pointed out that the thermal stability in the a-C:H films was not good at more than 300-400 °C due to the hydrogen desorption and the graphitization of a-C:H films.

Although photoemission spectroscopy studies are important to investigate the electronic structure such as the density of states, the orbital characteristic, the sp^2 and sp^3 contents, etc., there are few reports on photoemission spectra of the valence band region and C 1s core level in the a-C:H films [3-4]. In particular, the evolution of photoemission spectra of the valence band region and C 1s core level in the a-C:H films as a function of the temperature has not been clarified. In this study, we investigated the electronic structure in the a-C:H film as a function of the annealing temperature using photoemission spectroscopy.

Results and discussion

Figure 1 shows the photoemission spectra of the valence band region in the a-C:H film as a function of the annealing temperature. The annealing temperatures of a-C:H film are denoted beside each spectrum. In the top, the photoemission spectrum in graphite is located for

comparison. After annealing at 200 °C, no clear change was observed as compared to the photoemission spectrum at RT. With increasing the annealing temperature at 400 °C, a small peak at 3.0 eV appeared. With increasing the annealing temperature at 600 °C, several peaks were clearly observed at 19.0, 13.0, 10.0, 7.8, 5.5 and 3.0 eV. With further increasing the annealing temperature at 800-950 °C, a peak at 6.7 eV in addition to the several peaks at 19.0, 13.0, 10.0, 7.8, 5.5 and 3.0 eV were observed. The photoemission spectra after annealing at 600-950 °C are similar to that of graphite except for the peak at 6.7 eV. Therefore, the several peaks at 19.0, 13.0, 10.0, 7.8, 5.5 and 3.0 eV are derived from graphite although the origin of the peak at 6.7 eV is not clear at present. This indicates that the annealing at 600-950 °C causes the graphitization of a-C:H film. In addition, the observation of the peak at 3.0 eV after annealing at 400 °C suggests that the graphitization of a-C:H film starts to arise below this temperature.

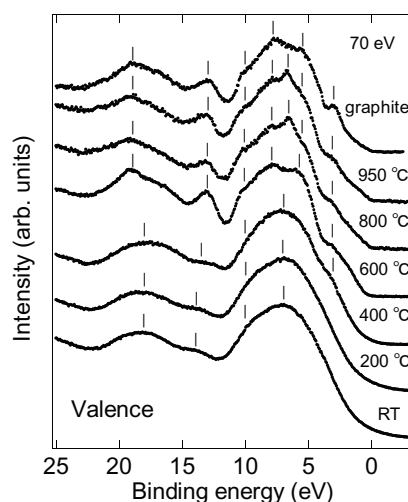


Fig.1 Photoemission spectra of the valence band region in the hydrogenated amorphous carbon film as a function of the annealing temperature.

Figure 2 shows the photoemission spectra (dots) of the C 1s core level in the a-C:H film as a function of the annealing temperature. A shift of the peak position to the lower binding energy side was observed with increase the annealing temperature. In addition, the width of the photoemission spectra of the C 1s core level in a-C:H films were observed to be narrower with increase the annealing temperature. In the photoemission spectrum in graphite, a peak at ~284.4 eV with a wide tail to the higher binding energy side was observed. The photoemission spectrum of the C 1s core level in the a-C:H film after annealing at 950 °C is similar to that of graphite. The broader spectral feature at lower temperature suggests that there are some C 1s components in different chemical environments. In the previous photoemission study of unhydrogenated amorphous carbon films, the photoemission spectra of the C 1s core level were essentially composed of two components positioned at 284.4 and 285.2 eV [5-6]. From the position of the binding energy in graphite and diamond, the two components at 284.4 and 285.2 eV were assigned to the C 1s electrons originating from the sp^2 and sp^3 hybridized carbon atoms, respectively. In the case of a-C:H films, the contribution from the C-H bonded carbon atoms in addition to the sp^2 and sp^3 hybridized carbon atoms would be needed. In the previous photoemission spectrum of the C 1s core level in the hydrogen terminated C(111) surface, only a single peak was observed, indicating that the binding energy of the bulk C 1s component is same as that of C-H bonded C 1s component [7]. This also suggests that the electro-negativity of carbon atoms is similar to that of hydrogen atoms on the hydrogen terminated C(111) surface. Therefore, the C 1s electrons originating from the C-H bonded carbon atoms were tentatively assigned to the component at 285.2 eV. In this case, it is difficult to reliably distinguish between the sp^3 hybridized and the C-H bonded carbon atoms from the photoemission spectra. In the previous study of a-C:H films formed by the vapor phase methods such as the ion plating and ECR plasma methods [4], the sp^2 contents estimated from the XPS spectra were in good correspondence to those estimated from the EXAFS spectra although there is an influence of the C-H bonded carbon atoms on the photoemission spectra of the C 1s core level. This result suggests that there is almost no influence on the estimation of the sp^2 hybridized carbon atoms using the XPS spectra. Therefore, the contents of the sp^2 hybridized carbon atoms and the contents of the sum of the sp^3 hybridized and the C-H bonded ($sp^3 + C-H$) carbon atoms could be estimated using the XPS spectra. For this reason, a curve fitting analysis was performed on the photoemission spectra of the C 1s core level using two components positioned at 284.4 and 285.2 eV. In Fig. 2, the best fitting results (lines) for a-C:H films are shown. The sp^2 and $sp^3 + C-H$ carbon

contents in a-C:H films, which are evaluated from the area intensity of each component, are summarized in Ref. 8. The error range for evaluation of the sp^2 and $sp^3 + C-H$ carbon contents was $\pm 5\%$. After annealing at 200 °C, almost no change was observed. With increasing the annealing temperature at 400 °C, the sp^2 carbon content increased by 5%. With increasing the annealing temperature at 600 °C, the sp^2 carbon content increased rapidly by 18%. With further increasing the annealing temperature at 800-950 °C, the sp^2 carbon content increased gradually. The sp^2 content in the a-C:H film after annealing at 950 °C was shown to be highest as compared with those after annealing at less than 800 °C. These results indicate that the graphitization of a-C:H films starts below 400 °C and proceeds with increasing the annealing temperature.

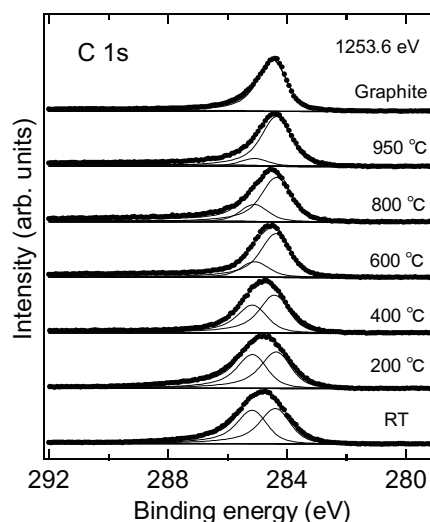


Fig.2 Photoemission spectra (dots) of the C 1s core level in the hydrogenated amorphous carbon film as a function of the annealing temperature. In the top, the photoemission spectrum of graphite is located for comparison. The fitting results (lines) are also plotted in each spectrum.

References

- [1] J. Ullmann, Nucl. Instrum. Methods Phys. Res., Sect. B **127** (1997) 910.
- [2] H. Tsai and D. B. Bogy, J. Vac. Sci. Technol. A **5** (1987) 3287.
- [3] J. Schafer *et al.*, Phys Rev B **53** (1996) 7762.
- [4] Y. Haruyama *et al.*, Jpn. J. Appl. Phys. **47** (2008) 3380.
- [5] P. Merel *et al.*, Appl. Surf. Sci. **136** (1998) 105.
- [6] J. Diaz *et al.*, Phys. Rev. B **54** (1996) 8064.
- [7] J. F. Morar *et al.*, Phys. Rev. B **33** (1986) 1340.
- [8] Y. Haruyama *et al.*, Jpn. J. Appl. Phys. **48** (2009) 055505-3.

Control of Oxygen Contamination in BN Thin Film Prepared by Reactive Magnetron Sputtering

Masahito Niibe and Yoshie Maeda
LASTI, University of Hyogo

Abstract

To control oxygen contamination in BN thin film prepared by sputtering technique, high purity gases of Ar:6N and N₂:6N5 were used for magnetron sputtering as well as inserting purifier into the gas line. The vacuum chamber was baked at low temperature of 60 °C for about 17 hrs before thin film preparation. Oxygen concentration was evaluated by B-K edge X-ray absorption spectroscopy (XAS) as well as XPS and XAS analyses. It was found that the amount of oxygen contamination was controlled to be less than 1.4 % in the prepared BN thin film.

Introduction

For fabrication of metal nitride thin films by reactive sputtering, oxygen contamination becomes often problematic. For example, ultra high vacuum system was proposed to use for preparation of titanium nitride thin film [1]. However, in the thin film fabrication system practically used for coating of mechanical tools, it is necessary to develop the technique to control oxygen contamination for open-air thin film fabrication system. We examined the contamination control technique in preparation of boron nitride (BN) thin film which is one of the easily oxidizing materials.

Experiments

The BN thin films were fabricated by an RF magnetron sputtering system with open-air type sample changing. The cross-sectional schematic view of the system is shown in Fig. 1. The back ground pressure of the preparation chamber was about 2×10^{-4} Pa. Mixed gas of Ar and N₂ with mixing ratio of 1:1 was used for sputtering. The target was a sintered h-BN with 125 mm in diameter. The substrate temperature was not controlled and was less than 50 °C during the sample preparation. We supposed that the origins of oxygen contamination were residual water vapor in the chamber and also water and

oxygen gas contained in the sputtering gases from the gas cylinders. The purity of used gas was improved from 99.999% to 99.9999% (6N) for Ar and from 99.9995% to 99.99995% (6N5) for N₂ gas in the cylinder. Gas purifiers (PURERON GP-05) were also inserted into the gas introduction lines. The vacuum chamber was baked at low temperature of 60 °C for about 17 hrs before thin film preparation.

Oxygen concentration in the prepared film was evaluated by X-ray photoemission spectroscopy (XPS, Shimazu ESCA-1000) and B-K edge X-ray absorption spectroscopy (XAS) at the BL9 [2] in the NewSUBARU SR facility. The XAS measurement was carried out by total electron yield (TEY) mode with measuring sample current when the photoelectron emitted by soft X-ray absorption. An Auger electron spectroscopy (AES) was also employed for depth analysis.

Results

Figure 2 shows a B-K edge XAS spectrum of a prepared BN thin film, the oxygen concentration of which was comparatively high. The structure of the BN film was hexagonal (h-BN). Four sharp π^* resonance peaks were observed at the photon energy from 192 to 194eV. These peaks were formerly

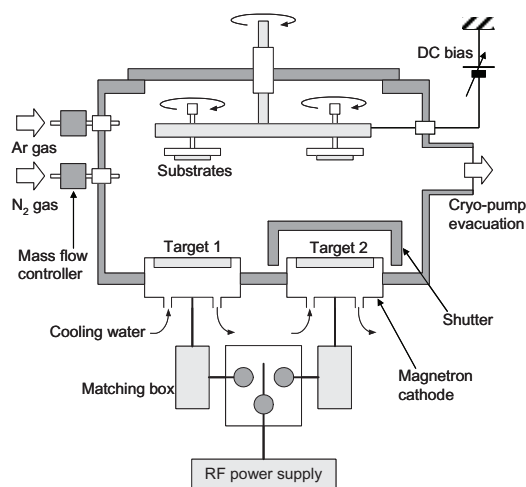


Fig. 1 Cross-sectional schematic view of the RF magnetron sputtering system.

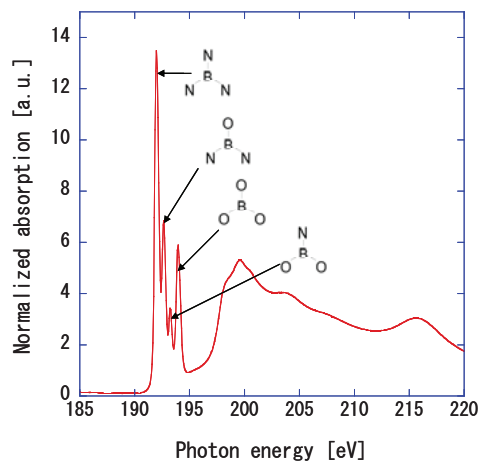


Fig. 2 Typical B-K edge XAS spectrum of a prepared BN thin film.

identified by the authors [3] as B atoms coordinated by three N atoms (192.0 eV), and B atoms bound to one-to-three oxygen atoms substituted for three nitrogen atoms surrounding for higher energy three peaks as shown in the figure.

Figure 3 shows the QMS intensity change of residual H₂O(18) and O₂(32) components in the chamber during the long term baking. Although, the data scattered day by day, the average amounts of residual gases in the chamber decreased 79% for H₂O and 92% for O₂ during four months operation.

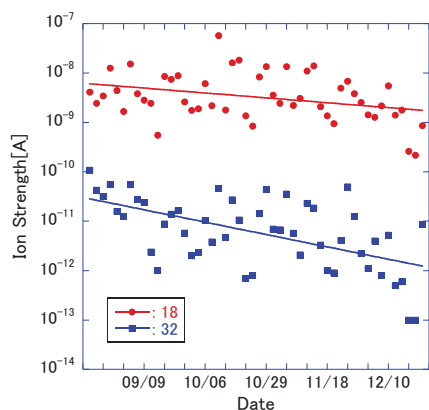


Fig. 3 QMS intensity change of residual H₂O(18) and O₂(32) components in the chamber during the long term baking.

B-K edge XAS spectra of prepared BN thin films before and after improvement in vacuum atmosphere is shown in Fig. 4. The intensity of three π^* peaks at the higher energy side decreased remarkably after the improvement. A curve fitting calculation indicates that ratio N and O atoms bonding to the B atoms for the sample of before the improvement was 73% and 27%, respectively. However, the values changed for the sample after improvement as 92% and 8%, respectively.

Depth analysis of the prepared sample was carried out by AES analyzer at the Faculty of Engineering, University of Hyogo, because etching gun for depth

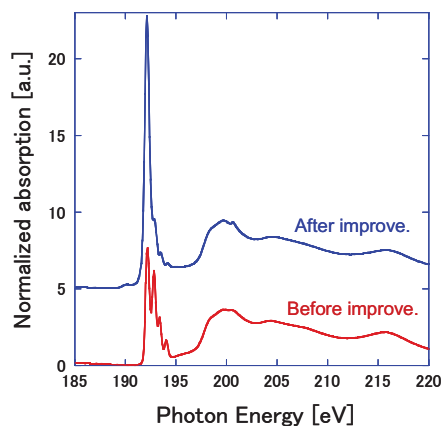


Fig. 4 B-K edge XAS spectra of prepared BN thin films before and after the improvement in vacuum atmosphere.

analysis was not provided yet for XPA and XAS equipments. Figure 5 show the AES spectra of prepared BN thin film before and after the Ar ion etching. Some amounts of oxygen and carbon were observed on the surface of the thin film as-deposited and exposed to open air. The oxygen concentration at the surface evaluated by AES measurement was about 5 atomic %. However, after the 100 sec etching with Ar ion, the oxygen concentration decreased rapidly to about 1.4%.

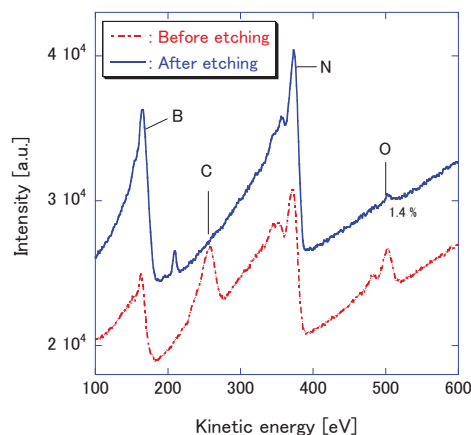


Fig. 5 AES spectra of BN thin film prepared before and after the Ar ion etching.

Conclusion

The oxygen contamination was successfully controlled by using high purity sputtering gas and long term baking with low temperature for open air type magnetron sputtering system.

Acknowledgment

The authors thank to Prof. Shozo Inoue at the University of Hyogo for his support to measure the AES depth profile and the spectra.

References

- [1] K. Hoshi *et al.*, Proc. ISSP2007 Kanazawa Japan.
- [2] M. Niibe *et al.*, AIP Conf. Proc. **705** 576 (2004).
- [3] M. Niibe *et al.*, Bulletin Soc. Discrete Variational Xa, **21**, 179 (2008).

Semi-quantitative analysis of carbon contamination on MLMs using high power EUV light

Takahiro Nakayama^a, Hiroyoshi Kubo^a, Akira Miyake^a, Hiromitsu Takase^a, Shigeru Terashima^a,
Shintaro Kawata^b, Takashi Aoki^b, Shuichi Matsunari^b,
Hiroo Kinoshita^c, Takeo Watanabe^c, Masahito Niibe^c

^aCanon, 23-10, Kiyohara-Kogyodanchi, Utsunomiya-shi, Tochigi-ken, 321-3298, Japan

^bNikon, 1-10-1, Asamizodai, Sagamihara-shi, Kanagawa-ken, 228-0828, Japan

^cLaboratory of Advanced Science and Technology for Industry (LASTI), Univ. of Hyogo, 3-1-2, Kouto, Kamigori-cho, Ako, Hyogo 678-1205, Japan

Abstract

It is very important to mitigate oxidation of multilayer mirrors (MLMs) and carbon deposition onto MLMs to extend the lifetime of EUV exposure tool. In this study we focused on carbon deposition on Si-capped multilayer mirror. We made experiments of EUV irradiation to the MLMs using apparatuses connected to an undulator beamline (BL9) of synchrotron radiation facility New SUBARU in the University of Hyogo. This undulator beamline stably gives us high-power EUV light. As the result of experiments, we found that carbon deposition rate was constant until carbon thickness became 2.5 nm.

Introduction

HVM (High Volume Manufacturing) EUV Scanner is needed to operate for several years without high maintenance cost. In order to estimate a lifetime for HVM, we have to figure out scaling law. We focus on the scaling law of contaminations on multilayer mirrors (MLMs). Carbon deposition on MLMs causes a damage of optical performances. We have to elucidate a photochemical reaction of EUV irradiation to the MLMs and estimate carbon deposition rate for HVM. We have found dependences of carbon deposition rate on average EUV intensity, hydrocarbon partial pressure, characteristics of EUV source¹⁻³. We have elucidated these dependences by carbon deposition rate. But we do not know whether carbon deposition rate is constant or not. So we need to make sure if carbon deposition rate is constant to understand the reaction quantitatively.

Experiments and Results

We made experiments using an apparatuses connected to an undulator beamline (BL9) in NewSUBARU synchrotron radiation facility in the University of Hyogo. Figure 1 shows schematic diagram of the apparatus.

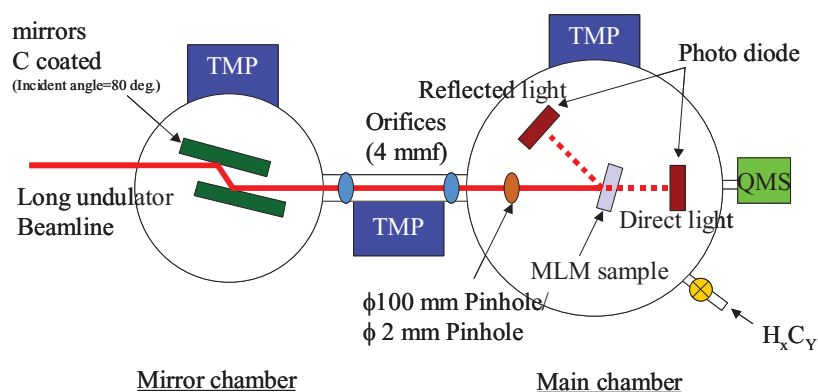


Figure 1. Schematic diagrams of EUV irradiation apparatus

We used X-ray photoelectron spectroscopy (XPS) and obtained carbon deposition quantity from photoelectron intensity of C(1s). We converted photoelectron intensity of C(1s) into a carbon film thickness. Furthermore, we calculated carbon deposition rate by dividing the carbon film thickness by the total irradiation time. The average EUV intensity distribution is shown in Fig. 2. Figure 2 also shows carbon thickness distribution as an example. Dependence of carbon deposition rate on average EUV intensity was figured out using these data. Figure 3 shows the dependence of carbon deposition rate on average EUV intensity. Decane (C₁₀H₂₂) was injected at the partial pressure of 1E-6 Pa. The carbon deposition rate does not increase proportionally to the average EUV intensity.

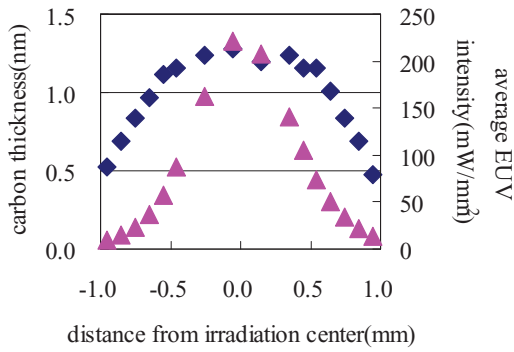


Figure 2. Distribution of Carbon thickness and average EUV intensity

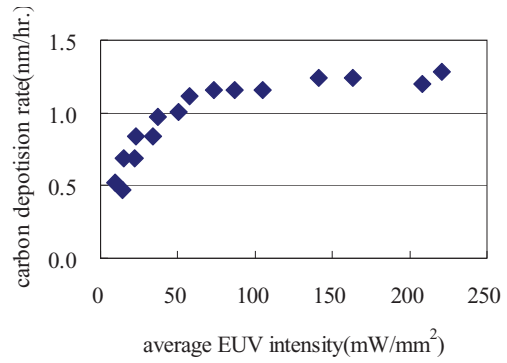


Figure 3. Dependence of carbon deposition rate on average EUV intensity

A standing wave on MLMs affects on generating secondary electrons⁴. It is considered that carbon is deposited by interaction between secondary electrons and adsorbed molecules. So carbon deposition rate must be changed by the standing wave. We made experiments to figure out if carbon deposition rate changes depending on time during EUV irradiation. Experimental results show time dependence of carbon thickness in fig. 4. The result is comparing between two different EUV intensities. Carbon thickness was increasing constantly until it became 2.5 nm. We fitted experimental data by least square method and it was good agreement.

Table 1. Experimental conditions.

Decane partial pressure (Pa)	Irradiation time (min.)
1E-5	5
1E-5	15
1E-5	30

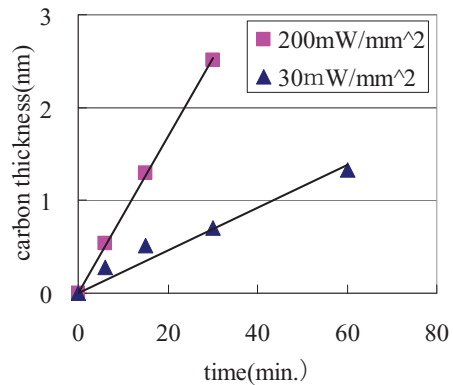


Figure 4. Time dependence of carbon thickness

In conclusion, we made experiments using an undulator beamline (BL9) in NewSUBARU synchrotron radiation facility and figured out dependence of carbon deposition rate on average EUV intensity up to high EUV intensity. We also figured out if carbon deposition rate is constant. The carbon deposition rate does not depend on carbon thickness until it becomes 2.5 nm. The standing wave does not affect on carbon deposition on our MLMs so much. As future works, we need to calculate amount of secondary electrons depending on carbon thickness and compare simulation with experimental results.

ACKNOWLEDGMENT

A part of this work was supported by the Ministry of Economy Trade and Industry (METI) and New Energy and Industrial Technology Development Organization (NEDO).

REFERENCES

- [1] H. Takase, "Study of Ruthenium-capped Multilayer Mirror for EUV Irradiation Durability", Proc. of SPIE Vol. 6151, 35, 2006
- [2] T. Nakayama, "Phenomenological analysis of carbon deposition rate on the multilayer mirror", Proc. of SPIE Vol. 6921, 3B, 2008
- [3] T. Nakayama, et. al., "Analysis of carbon deposition on multilayer mirrors by using two different beamlines", Proc. of SPIE 7271(2009) 72713P.
- [4] S. B. Hill et. al., "Accelerated lifetime metrology of EUV multilayer mirrors in hydrocarbon environments", Proc. of SPIE 6921,42 , 2008

Electronic State of Ti in Ultra-fine Grained SUS316L-1%TiC

M. Terasawa, T. Mitamura, M. Niibe, LASTI, University of Hyogo
T. Yamasaki, Dept. of Materials and Chemistry, Graduate School of Engineering, University of Hyogo
H. Kurishita, Institute for Materials Research (IMR), Tohoku University
M. Kawai, Institute of Material Structure Science, High Energy Accelerator Research Organization (KEK)

Abstract

Ultra fine grained (UFG) materials of SUS316L were fabricated by mechanical alloying (MA) and hot isostatic pressing (HIP) treatments. It was found that addition of about 1 % TiC powder was effective to reduce the grain size down to 100 nm, and the materials exhibited superior irradiation resistance and mechanical properties. The electronic states of the TiC in the UFG materials were analyzed by XANES spectroscopy at NewSUBARU BL9.

Introduction

In the J-PARC program, which is a large accelerator development project in Japan to promote use of secondary particles, such as neutron, pi- and myu-particles, neutrino and so on, very high energy and high current proton beams are utilized. For the neutron source in the J-PARC facility, liquid mercury target enveloped with metallic container is planned to be adopted. The container materials must be tough for heavy irradiation induced by intense proton and neutron flux, in addition to severe erosion due to mercury exposure. One of the candidate materials is ultra fine grained (UFG) SUS316L-1%TiC. It is strongly expected that the materials are developed so as to show tough resistance for such phenomena.

We are developing ultra-fine grained materials of austenitic stainless steel (316L) with addition of small amount of TiC powder. In this work, electronic state analysis of TiC in the UFGSUS316L-TiC materials was investigated by XANES spectroscopy in order to elucidate the effect of TiC addition.

Experiments and Results

Fabrication of ultra-fine grained materials

Ultra-fine grained materials of austenitic stainless steel (SUS316L) were fabricated by mechanical-alloying (MA) and hot isostatic pressing (HIP) treatments. Powder of SUS316L (an average particle size: 44 – 105 μ m), combined with TiC (0.57 μ m), was used as the starting materials.

The SUS316L-1.0wt.% TiC materials with the average grain sizes of 100 nm were obtained by 80 % cold roll and annealing at the temperature of 800°C, after MA and HIP (800°C) treatment. The fabricated materials have exhibited superior resistance to neutron irradiation examined in JMTR up to 1.14×10^{24} n/m² ($E_n > 0.1$ MeV). The hardness increase of the materials after the irradiation is only 6.0 %, though much higher increase (73 %) is shown in the simultaneous irradiation of the standard SUS316L specimens. (Fig.1) The lower void swelling of the

ultra-fine grained materials than standard 316L is also found in 1 MeV electron irradiation, as shown in Fig.2.[1,2]

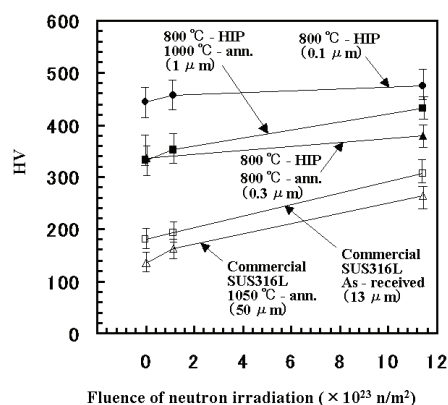


Fig.1 Vickers microhardness of the UFG316L-TiC as a function of neutron irradiation dose ($E_n > 0.1$ MeV)

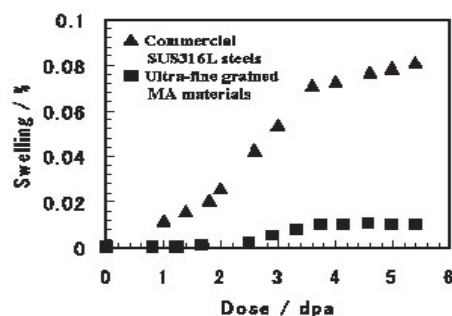


Fig.2 Void swelling of the UFG316L-TiC irradiated by 1 MeV electrons at 400°C

The ultra-fine grained W-1.1wt.% TiC materials with the grain size of 50 – 100 nm have been also obtained by the same fabrication method, and exhibited excellent resistance to the irradiation with neutrons and helium ions. [3,4]

Electronic state analysis of TiC in UFG materials

In the fabrication of the UFG materials, small amount (about 1 wt.%) of TiC addition is found extremely effective to control the grain size, as described above

in both SUS316L and W. Although it is suggested that TiC nano particles act so as to pin the grain boundary during the fabrication process, what kind of interaction of TiC with matrix materials is concerned, and by what mechanism the pinning is governed are not clear.

We tried to measure the electronic states of Ti in the SUS316L-1.0wt.% TiC consolidates, as a preliminary step to elucidate the behavior of Ti or TiC in the fabrication process. XANES spectroscopy was performed at the end-station of the long undulator beamline BL9 in the NewSUBARU SR facility using a high resolution monochromator. The data were collected by a total electron yield (TEY) mode in which the sample current was measured when the photoelectron emitted by soft x-ray absorption. The values were normalized with a simultaneously recorded photoemission signal from a gold mesh, which indicates the soft x-ray intensity incident into the sample. At the present time, XANES spectra of Ti-L and C-K absorption edge of TiC in the SUS316L-1.0wt.% TiC consolidates were measured.

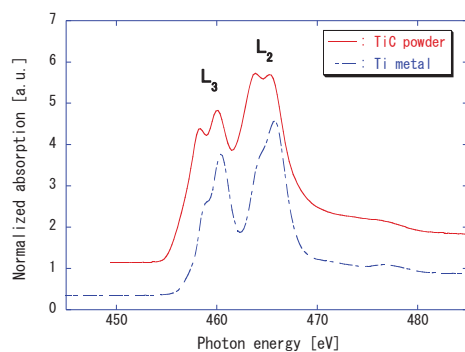


Fig.3. Ti-L_{2,3} edge XANES spectra of Ti and TiC

Fig.3 shows Ti-L_{2,3} absorption spectra for pure Ti (99.99 %) metal and TiC powders measured for reference before the XANES study for the fabricated SUS316L-TiC materials. A peak of Ti-L₂ (2p_{1/2}) and L₃ (2p_{3/2}) was observed at 465.9 eV and 461.4 eV, respectively, in the Ti specimen. On the other hand, each of L₂ and L₃ spectral line exhibits twin peak structure with an additional line with a separation of about 1.5 eV for the TiC powder specimen. The spectral variation is reflected by electronic structure due to different chemical state.

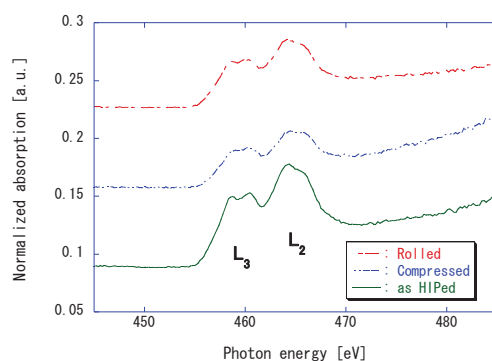


Fig.4. Ti-L_{2,3} edge XANES spectra of UFG316L-TiC materials

Fig.4 shows XANES spectra of Ti-L_{2,3} for the UFG SUS316L-1.0wt.% TiC specimens. Three kinds of materials, that is, as HIPed, high temperature compressed, and cold-rolled, are examined. The XANES spectra observed show characteristic twin peak structures for both L₂ and L₃, which are in general agreement with the spectra shown in TiC powders. The NEXAFS spectra are decomposed for TiC powder and for SUS316L-TiC (as HIPed) as shown in Fig.5a and Fig.5b, respectively. The 2p spectra of TiC powder are separated to two peaks (463.4 eV and 465.5 eV) for L₂, and other two peaks (458.1 eV and 460.0 eV) for L₃. On the other hand, the 2p spectra of SUS316L-TiC (as HIPed) are separated to two peaks (463.9 eV and 465.9 eV) for L₂, and other two peaks (458.4 eV and 460.3 eV) for L₃. The lower energy peak in L₂ is due to t_{2g} (π-bonding), and higher energy peak e_g (σ-bonding). Likewise the lower energy peak in L₃ is due to t_{2g}, and higher energy peak e_g. The energies of the peaks in the UFG materials coincide with the corresponding peaks in the TiC powder. However, the e_g peaks are smaller than the t_{2g} peaks for both L₂ and L₃ in SUS316L-TiC compared with TiC powder. The real reason of this feature is not known at present. It may be concluded almost of all Ti atoms exist in the form of TiC in the UFG materials, but, in the same time, it is suggested other kind of precipitates exist with scarce concentration in the matrix.

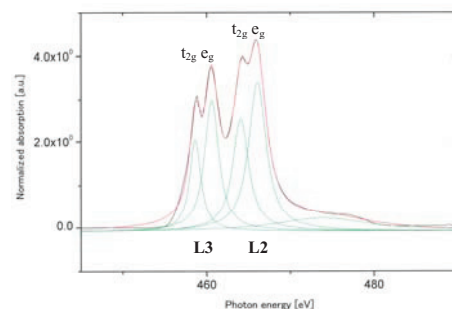


Fig.5a. Ti-L_{2,3} NEXAFS for TiC powder

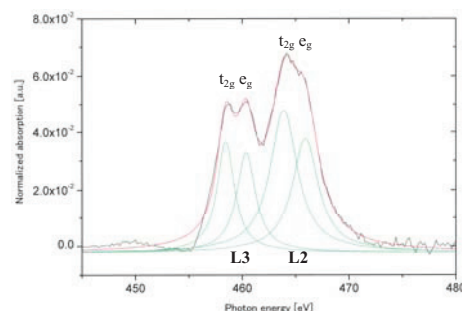


Fig.5b. Ti-L_{2,3} NEXAFS for SUS316L-TiC

References

- [1] Y. Z. Cheng et al, Material Science Forum, **426-432**, pp.1065-1070 (2003).
- [2] H. Matsuoka et al, Proc. ICAPP'05, Seoul, Korea (2005) paper 5687
- [3] H. Kurishita et al, Phys. Scr. T128 (2007) 76-80
- [4] H. Kurishita et al, IWSMT-8 (2006)

Fabrication of High Aspect Ratio Microcoils

Daiji Noda, Masaru Setomoto, and Tadashi Hattori
Laboratory of Advanced Science and Technology for Industry, University of Hyogo

Abstract

Recently, there has been a growing requirement to reduce their size of actuators. Actuators, which held big volume and weight with a part of a product, have been required to reduce their size. However, the miniaturization of electromagnetic actuators has made little progress since it requires three-dimensional micro-fabrication processing and new technologies. We have focused on the fabrication of electromagnetic type microactuators that could be driven at low voltage and with high efficiency but it is well known that existing technologies for miniaturization of these devices are unsuitable because the allowable current path would be too small in microscopic applications. Therefore, we have fabricated a spiral microcoil with narrow pitch and high aspect ratio coil line structures using X-ray lithography and metallization techniques. We have fabricated spiral microcoils at a pitch of 60 μm . Thus, an aspect ratio of coil lines was achieved about 5 as coil lines of 30 μm . By using these techniques, microcoils with narrow pitch and high aspect ratio can be achieved, which are expected to yield high performance.

Introduction

Recently, reductions in size and increases in sophistication have become desirable for many parts and devices. Actuators, which hold big volume and weight with a part of a product, have been required to reduce their size. However, the miniaturization of actuators has made little progress since it requires three-dimensional (3D) micro-fabrication processing and new technologies. On the other hand, LIGA (German acronym for Lithographie Galvanoformung and Abformung) process [1] can be fabricated nano and micro parts for devices. This technique is possible to make high aspect ratio structure fixed the narrow pitch of coil line and space. For the deep X-ray lithography involved in the LIGA process, we used the NewSUBARU Beamline 11 (BL11), which is a synchrotron radiation (SR) facility owned by our university. The x-ray exposure at BL11 was carried out with the workpiece held in a specially manufactured 'nine parts operation' exposure stage [2]. Thus, this stage makes it feasible to do 3D deep X-ray lithography for microcoils. Therefore, we have fabricated a spiral microcoil with high aspect structure on pipe surface for electromagnetic type microactuators using a 3D deep X-ray lithography and metallization techniques.

Design of electromagnetic actuator

As the structure of the magnetic circuit, we used the type called *open frame solenoid*, which is open on the sides [3]. The material of electromagnetic core (fixed core and plunger) and shield parts (yoke) were used Permalloy that is a nickel iron alloy, because it has the largest permeability among soft magnetic metals. When the electrical supply to the coil is turned on, a magnetic flux forms in the gap, deforming the magnetic field and producing suction force on the plunger. If the aspect ratio is increased, the cross section area of coil lines is also increased

allowing a greater current path. Then, the magneto motive force is proportional to the squares of current path in the microcoil in this model [3]. This microactuator having the high aspect ratio of coil line is also expected a high performance in spite of miniature size.

Fabrication process of microcoil

The surface of acrylic pipe for a screw thread structure, this is the coil part, has made using LIGA process. Figure 1 shows the fabrication process of microcoil. First, a cylindrical structure was formed on the surface of acrylic pipe by X-ray lithography. Next, copper was thinly deposited on pipe surface by sputtering in order to use as a seed layer in the electroforming. And, copper was formed into narrow pitch spiral structure by electroforming. Then, pipe surface was completely covered with copper film.

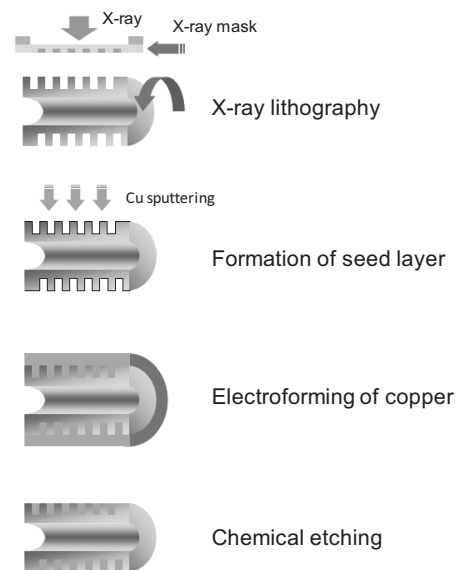


Fig. 1: Process flows of microcoil

Finally, forming Cu layer over the pipe surface was etched until the isotropic portions of wiring were exposed. We have fabricated a spiral microcoil at a pitch of 20 μm , as shown in Fig. 2. Thus, an aspect ratio of coil lines was achieved about 5 as coil lines of 30 μm . Following the seed layer deposition, we

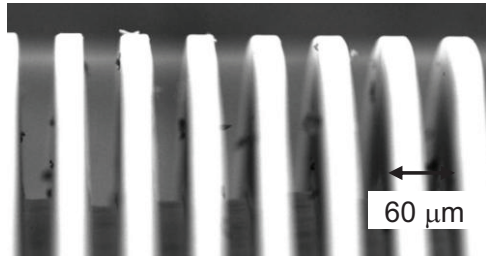


Fig. 2: SEM image of coil lines on acrylic pipe with aspect ratio of 5

formed uniform copper electroplating for the current path of microcoils. Here, we proposed and introduced the new technique of reverse pulse current for electroforming in order to form high aspect ratio structures. In this result, it was able to be confirmed that plating developed to reach the bottom surface of the grooves, as shown in SEM image of Fig. 3. Finally, isotropic copper etching was performed until the insulated portions of the wiring were exposed, as shown in Fig. 4.

Measurement of suction force

We have also fabricated a measurement system to measure the suction force of designed electro-

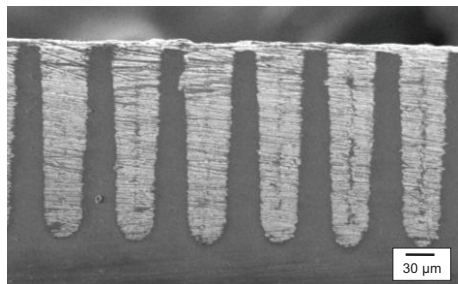


Fig. 3: SEM image of coil lines after copper electroforming

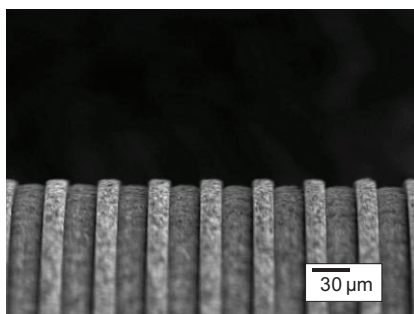


Fig. 4: SEM image of coil lines by isotropic copper etching

magnetic type actuators. This system is very simple structure and easy to exchange the coil part. The gap between plunger and fixed core was adjusted X-, Y-stage. The theoretical values by simulation and actual measurement results of suction force generated by the microcoil were compared, as shown in Fig. 5. These results are relatively in good agreement with theoretical values.

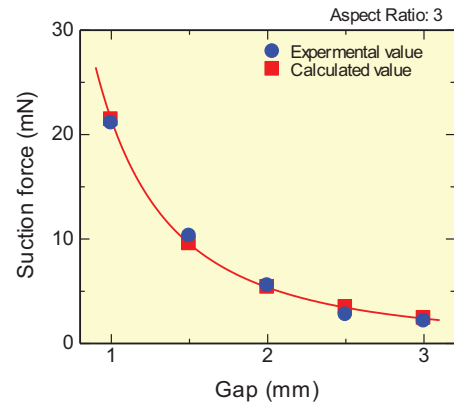


Fig. 5: Suction force comparison between measurement values and simulation results

Conclusions

We have fabricated microcoils with high aspect ratio using a 3D X-ray lithography and metallization technique in order to produce electromagnetic microactuators. We succeeded in producing a threaded structure with 30 μm in coil lines width and about 5 in the maximum aspect ratio.

On the other hand, we developed a measurement system to measure a suction force. In measurement results, theoretical values by simulation values and actual measurement of suction force were compared. By using these techniques, microcoils with high aspect ratio can be achieved, which are expected to yield high performance. It is anticipated that high performance microcoils could also be manufactured, in spite of their miniature size.

Acknowledgment

This research is partially supported by the Grant-in-Aid for Scientific Research on Priority Area, No. 438, "Next-Generation Actuators Leading Breakthroughs", from the Ministry of Education, Culture, Sports, Science and Technology, Japan.

References

- [1] E. W. Becker, W. Ehrfeld, P. Hagmann, A. Maner, and D. Munchmeyer, *Microelectron. Eng.*, **4**, pp. 35-56 (1986).
- [2] H. Mekaru, S. Kusumi, N. Sato, M. Yamashita, O. Shimada, and T. Hattori, *Jpn. J. Appl. Phys.*, **43**, 6B, pp. 4036-4040 (2004).
- [3] Y. Matsumoto, M. Setomoto, D. Noda, and T. Hattori, *Microsyst. Technol.*, **14**, 9-11, pp. 1373-1379 (2008).

Fabrication of X-ray Grating Using X-ray Lithography for X-ray Talbot Interferometry

Daiji Noda¹, Naoki Takahashi¹, Megumi Katori², Yasuto Minamiyama², and Tadashi Hattori¹

¹Laboratory of Advanced Science and Technology for Industry, University of Hyogo,

²Nanocreate Co., Ltd.

Abstract

X-ray radiographic imaging technique is very important in medical, biological, inspection, material science, and so on. However, it is not enough to obtain clear X-ray images of samples with low absorbance materials, such as biological soft tissues. Then, we have used an X-ray phase imaging method of an X-ray Talbot interferometer. In this method, X-ray gratings were required to have narrow pitch and high aspect ratio structure. Therefore, we have developed and fabricated high aspect ratio X-ray gratings with a pitch of 5.3 μm , a height of 30 μm , and a large effective area of 60 mm \times 60 mm using X-ray lithography and narrow electroforming technique. In this paper, we discuss the fabrication process of new X-ray mask and results of X-ray gratings of X-ray lithography technique.

Introduction

X-ray radiographic imaging technique is very important in medical, biological, inspection, material science, and so on. However, it is not enough to obtain clear X-ray images of samples with low absorbance materials, such as biological soft tissues. On the other hand, several methods for generating radiographic contrast from the information of X-ray phase shift have been investigated. It is improvement in the high sensitivity by about 1000 times higher than by conventional absorption contrast. Numerous researchers have studied a variety of methods of phase imaging [1,2]. X-ray Talbot interferometer (XTI) is one of the methods of X-ray phase imaging [1]. In order to use 10-40 keV X-ray irradiation, the Au thickness of absorptive material must be over 20 μm . But, it is not straightforward to make this structure with high aspect ratio by conventional techniques. Then, we have tried in fabricating such X-ray gratings particularly with a large area using X-ray lithography technique.

Fabrication of X-ray mask

The conventional X-ray mask fabrication process was used on Si wafer [3]. In this case, we have used SU-8 as membrane because of large effective area X-ray mask. Therefore, X-ray masks comprising a resin membrane have the disadvantage that, after several cycles of X-ray exposure, they crease and sag due to X-ray-derived heat. As a substitute for the conventional resin membrane, we proposed to fabricate a new X-ray mask using a carbon wafer membrane that has an extremely small thermal expansion coefficient and is easy to process.

Figure 1 shows fabrication process using carbon wafer for membrane material. The fabrication process consists of three steps: (a) depositing a seed layer on the carbon wafer, (b) applying resist over the seed layer to perform patterning by irradiation with UV and development, (c) forming an X-ray absorber, i.e. an Au film, by electrolytic plating. We succeeded

in making new X-ray mask with pitch pattern of 5.3 μm and large effective area of 60 \times 60 mm², as shown in Fig. 2. In contrast to conventional silicon substrates, the newly devised mask fabrication process does not require further membrane application, frame adhesion or substrate etching. Thus, this is very simple process.

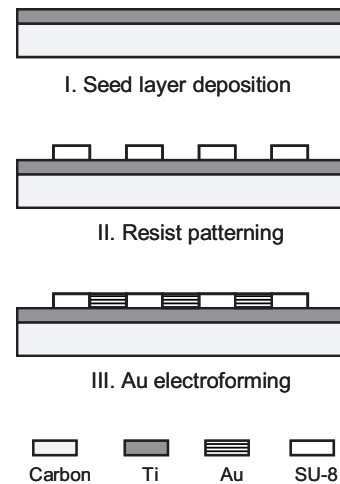


Fig. 1: New fabrication process of X-ray mask

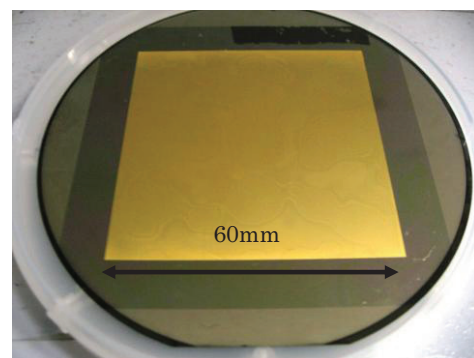


Fig. 2: Picture of carbon X-ray mask

Fabrication of X-ray grating

X-ray lithography using synchrotron radiation has been utilized for 2.5-dimensional applications on flat substrate. Therefore, we took advantage of this technology to fabricate a high aspect ratio structure required for X-ray gratings with a pitch of several micrometers. For X-ray lithography, we used NewSUBARU beamlines 2, which is the synchrotron radiation facility owned by our university [4]. The beamline 2 has a potential of large area patterning across an A4-size area with a highly uniform pattern thickness.

A target specification of the X-ray grating was 5.3 μm pitch pattern and large effective area of $60 \times 60 \text{ mm}^2$. For the deep X-ray lithography, we used a negative photo-resist SU-8. This SU-8 was originally designed for UV lithography. However it could also be used in deep X-ray lithography of high accuracy and high aspect ratio pattern. The pattern quickly collapses when the rinse solution is dried in the development and washing process. In order to solve this problem, we confirmed that line width of a provided cash register strike structure body became big with increase of an exposure a membrane came to be formed overexposure by the space top surface of line & space, as shown in Fig. 3. The X-ray grating was completed by gilding the resist structure of X-ray grating. And, we removed top surface layer using O_2 plasma, as shown in Fig. 4.

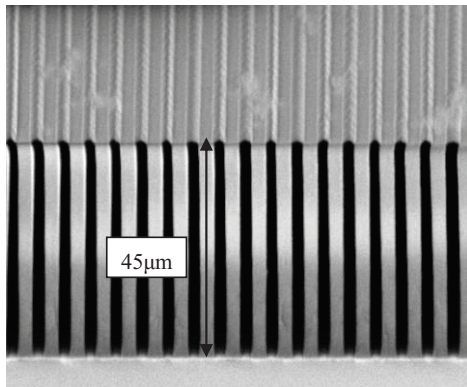


Fig. 3: SEM image of narrow pitch structure with top surface layer

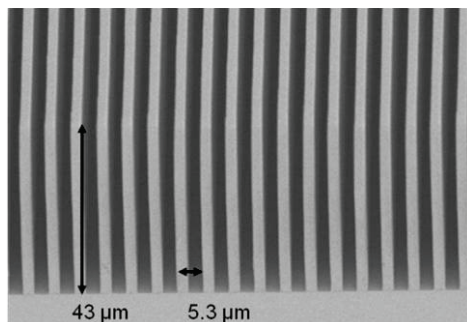


Fig. 4: SEM image of narrow pitch structure without top surface layer

Au absorbing part for the X-ray grating was formed by electroforming. In electroforming, chromium was used as seed film. A non-cyanic based solution was used for Au electroforming. From these results, the designed pitch of 5.3 μm and height of about 40 μm of X-ray grating are realized, as shown in Fig. 5.

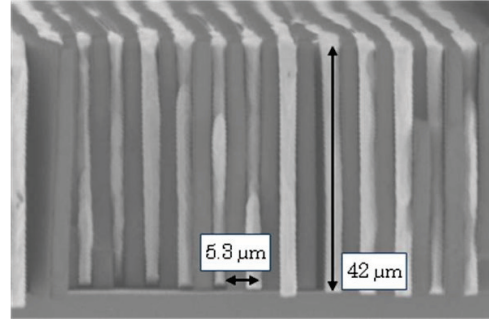


Fig. 5: SEM image of X-ray grating in cross section

Conclusions

We have fabricated X-ray gratings having a pitch of 5.3 μm and a large effective area of $60 \times 60 \text{ mm}^2$ for X-ray Talbot interferometry. We were new and devised that we used a carbon wafer as membrane materials of X-ray mask was used to break off a problem by the heat transformation of the membrane which happened at the time of X-rays exposure. To make a higher aspect ratio X-ray grating, we developed the fabrication process composed of X-ray lithography and micro electroforming method. In X-ray lithography, sticking was observed because of surface tension. Therefore, we formed on top surface layer by overexposure. In this result, the resist structure with high aspect ratio and narrow pitch was obtained without surface tension in large area. After Au electroforming, large area and narrow pitch X-ray grating could be fabricated.

This result suggests that XTI is a novel and simple method for phase sensitive X-ray radiography, and promising method for many imaging applications.

Acknowledgment

This research was supported by the research project “Development of Systems and Technology for Advanced Measurement and Analysis” from the Japan Science and Technology Agency (JST).

References

- [1] A. Momose, Jpn. J. Appl. Phys., **44**, 9A, pp. 6355-6367 (2005).
- [2] C. David, B. Nöhammer, H. H. Solak and E. Ziegler, Appl. Phys. Lett., **81**, pp. 3287-3289 (2002).
- [3] D. Noda, M. Tanaka, K. Shimada, and T. Hattori, Jpn. J. Appl. Phys., **46**, 2, pp. 849- 851 (2007).
- [4] Y. Utsumi, T. Kishimoto, T. Hattori, and H. Hara, Microsyst. Technol., **13**, 5-6, pp. 417-423 (2007).

Fabrication of High Hardness Ni Mold with Electroless Ni-B Thin Layer

Yoshitaka Sawa¹, Kenji Yamashita², Satoshi Nishida², Daiji Noda³, and Tadashi Hattori³

¹Sawa Plating Co., Ltd., ²Nanocreate Co., Ltd.,

³Laboratory of Advanced Science and Technology for Industry, University of Hyogo

Abstract

The nickel electroforming method using a high-concentration nickel sulfamate bath is commonly used to fabricate micro metal molds in the LIGA process; however, this method does not produce micro metal molds of sufficient hardness. In this research, we used a nickel-boron (Ni-B) electroless alloy plating method to obtain a hard nickel plated film having hardness of 832 Hv. It was also ascertained that Ni-B electroless alloy plated film retains its high hardness even during heat treatment in conditions of 250 °C for 1 hour. To deal with the high stresses developed in high-hardness plated films, we proposed double-layer nickel electroforming. This method is covered and used on conventional nickel electroforming layer by high hardness micro mold. High hardness micro metal mold using double-layer was fabricated by nickel electroforming and Ni-B electroless alloy plating method.

Introduction

Recently, strong demand for the sophistication, downsizing and intensified integration of systems used in such cutting-edge areas industries as advanced information communications, medical care, bioscience, environment and energy has been sharply accelerating microsystem applications. In connection with this market demand, a manufacturing method based on transfer technology using micro metal molds has recently been in the spotlight. In particular, the LIGA (acronym for the German words Lithographie, Galvanoformung, and Abformung) process, based on exposure technologies using ultraviolet (UV) rays or synchrotron radiation (SR), is receiving attention. In the LIGA process, a master of the mold that will be formed into a three-dimensional structure is fabricated by lithography technology, and the master mold is then used to fabricate the micro metal mold by electroforming. This micro metal mold is then used for the molding operation.

The mainstream method for manufacturing micro metal molds using the LIGA process [1] is based on the nickel electroforming method. Because Ni electroforming uses electrolytic deposition depending on the Ni electroforming conditions during micro mold creation, a camber can occur on the plated film due to electrode position stress, rendering the micro mold unsuitable for use in making molds. However, the Ni electroforming layer prepared using this additive-free bath exhibits a low surface hardness value of approximately 200 Hv, which is not sufficiently high, since the injection mold hardness requirement is approximately 400 Hv or more, in common practice.

Suggested ways of improving the Ni electroforming layer hardness are to introduce additives into the plating bath to downsize the crystal grains in the electroforming film, and Ni-based alloy plating based on a eutectic process involving phosphorus, boron or

other elements. Numerous reports are available on improving the mechanical properties of Ni electroforming film. In this study, not all the 4-mm-thick micro metal molds were created using hard Ni plated film; we used double-layer Ni plating to form thin membranes of hard Ni plating as a film to cover the camber-free surface of an existing Ni micro mold, in an attempt to make a micro mold that exhibits minimum camber, yet has high mold surface hardness.

Investigation of plating bath

We investigated Ni plating baths that can be used to produce the high-hardness Ni plating layer. In this study, we examined Ni-alloy-based plating baths of three types: commonly known nickel-phosphorus (Ni-P) electroless alloy plating, Ni-P alloy electroforming and nickel-boron (Ni-B) electroless alloy plating. Figure 1 shows a SEM image of the mold master after Ni-B electroless alloy plating (bath temperature: 60 °C). The mold master was made under the same conditions as Ni-P electroless alloy plating. Wrinkles creases did not develop on the photoresist structure side of the Ni-B electroless alloy plating layer. The plating temperature of the Ni-P electroless alloy plating bath, which can be as high as

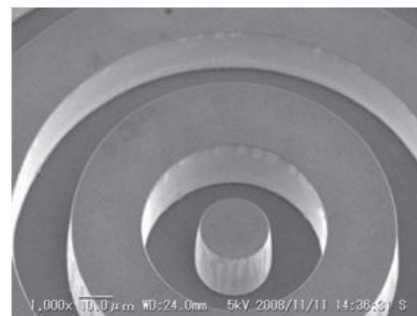


Fig. 1: SEM image of Ni-B electroless plating

90 °C, was considered responsible for the development of wrinkle creases on the plating layer. In response to this problem, this study examined use of a Ni-B electroless alloy plating layer to produce a hard Ni plating layer, since that plating process enabled a lower bath temperature. We assessed this layer mechanical property as a metal mold covering layer.

Results and discussions

The Ni-B electroless alloy plated film was assessed by internal stress, surface hardness, and abrasion examination test. Test samples of approximately 40 μm thick plated film, deposited from the 50 and 60 °C baths, were used.

Figure 2 shows the results of the hardness measurement of Ni-B electroless alloy plated film. The hardness of the plated film deposited from the plating bath at a temperature of 50 °C was 808 Hv and that from the plating bath at a temperature of 60 °C was 832 Hv. The Ni-B electroless alloy plated film did not exhibit any reduction in hardness as a result of heat treatment below 300 °C. The heat treatment at 300 °C yielded hardness values of 904 Hv (for bath temperature of 50 °C) and 960 Hv (for bath temperature of 60 °C), both values being higher than that obtained immediately after deposition without heat treatment.

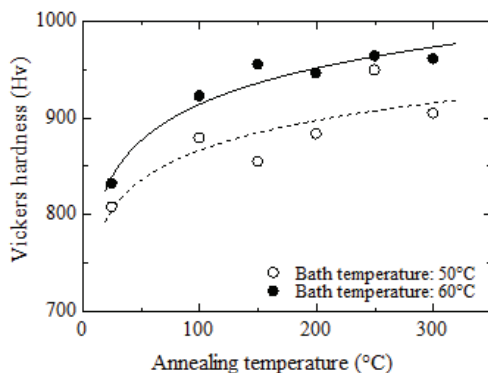


Fig. 2: Measurement results of Vickers hardness

Fabrication of high hardness micro mold

We prepared a Ni micro mold using the double-layer plating method, which combines a hard Ni plated film, with mold covering layer composed of a Ni-B electroless alloy plated film, and a Ni electroforming layer produced in an additive-free bath. In the present study we used a light guide plate pattern with fine reflecting protrusions [2].

We used a Ni-B electroless alloy plating bath at a temperature of 60 °C to deposit a hard Ni plated film approximately 1 μm thick on this mold master. The surface of the hard Ni plated film, deposited before electroforming in an additive-free bath, was soaked in an organic degreasing agent for one minute as pretreatment, and then soaked in a 10% sulfuric acid

solution for one minute as surface activation treatment. This was followed by electroforming in an additive-free bath to enable deposition of a Ni electroforming layer to be 4 mm thick. Figure 3 shows SEM images of the Ni electroforming mold we prepared and of the truncated-cone-shaped reflecting protrusions of the light guide plate. Also shown are SEM images of a cross section of the truncated-cone-shaped reflecting protrusions.

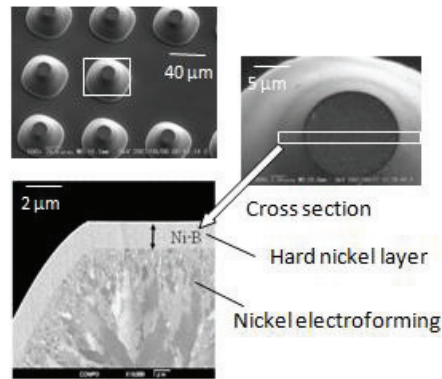


Fig. 3: SEM image of fabricated Ni micro mold with Ni-B double layer

Conclusions

We have studied electroforming molds based on the LIGA process as a technology for manufacturing 3D fine micro-structures. Since nickel electroforming molds fabricated using an additive-free bath do not meet the hardness requirement associated with injection molding, we studied methods of increasing hardness by means of alloy plating. Thanks to the plated film deposited from the Ni-B electroless alloy plating solution, we successfully obtained a hard plated film with a hardness of 800 Hv or more. These results show that we succeed in producing double-layer plating consisting of a hard plated film and electroformed film in an additive-free bath, verifying that the hard Ni plated film that served as a mold covering layer covered the entire mold pattern, and in successfully fabricating molds that accurately transfer mold master patterns prepared by UV lithography.

Furthermore, we will apply the current technology to large electroformed molds, with the aim of establishing a process for making large-area micro metal molds.

References

- [1] E. W. Becker, W. Ehrfeld, P. Haggmann, A. Maner, and D. Munchmeyer, *Microelectron. Eng.*, Vol. 4, pp. 35-56 (1986)
- [2] T. Tanaka, T. Nomura, Y. Funabiki, T. Kitadani, K. Idei, K. Yamashita, D. Noda, and T. Hattori, *Proc. 2006 IEEE Int. Sympo. on Micro-Nano Mechatronics and Human Science*, Nagoya, Japan, pp. 480-485 (2006).

Fabrication of Light Guide Plate for Ultraviolet Range

Yuta Okayama¹, Takaya Fujimoto¹, Kenji Yamashita¹, Satoshi Nishida², Yoshitaka Sawa³,
Daiji Noda¹, and Tadashi Hattori¹

¹Laboratory of Advanced Science and Technology for Industry, University of Hyogo,

²Nanocreate Co., Ltd., ³Sawa Plating Co., Ltd.

Abstract

The light guide plate, as part of the backlight unit in a cellular phone or liquid crystal display, has evolved to meet market demands for low power consumption, high-luminance and high-quality displays. Along with the advance of the light guide plate, light emitting diodes have undergone development as light source for light guide plates. In recent years, the ultraviolet light are used as a source of light of the air cleaner, and it is used as a source of light to activate the titanium dioxide which is photocatalyst. However, common ultraviolet light sources are either line or point light sources. Therefore, we studies surface illuminators that incorporate diffusers in the visible light range. Applying our existing technology, we constructed an unprecedented ultraviolet surface illuminator and measured it using a photocatalyst.

Introduction

In recent years, liquid crystal displays (LCDs) have come to be widely used in cellular phones and TV sets. This popularity has led to growing demand for a higher performance light guide plate as an LCD component. In the light guide plate, light is guided from a light emitting diode (LED) or other point light source to desired locations via total internal reflection rendered by index of refraction differential between air and diffuser material. The light in light guide plate tears a total reflection condition by reflecting in an internal projection (dot) and irradiates the surface [1]. The light guide plate, converts point light source to surface illumination. Figure 1 shows a schematic diagram of a light guide plate. One advantage of the light guide plate is its efficient use of light through the conversion of point light source to surface illumination. To apply our technology to surface illuminators using ultraviolet (UV) light, which have begun to be used recently in home air cleaners and the like, we have embarked on fabricating a light guide plate specifically designed for UV-LEDs.

In this study, optimal bump shape and allocation were derived for UV surface illuminators. Indeed, a light guide plate was fabricated using the molding technology.

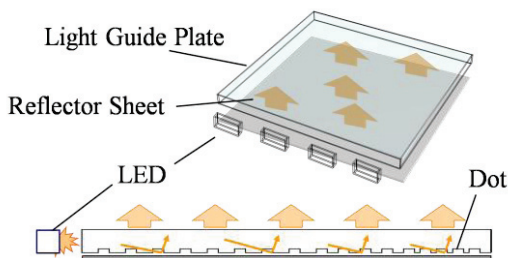


Fig. 1: Schematic diagram of light guide plate

Design of light guide plate by simulation

The reflection dot of the bottom of light guide plate influences irradiation of the light. Therefore, in

achieving uniform surface illumination with a light guide plate alone, the shape and allocation of reflective bumps are of much importance. Optimization of bump shape and allocation enables the creation of a light guide plate for uniform illumination. First, the optimal bump shape was obtained. The bump shape was transformed from a cylindrical column to a truncated cone, using fixed dimensions of 30 μm height and 52 μm base diameter. Comparisons were made among cylindrical column, from 50 to 80 degree tapered truncated cones, taking heed of visible-light diffuser conditions that the laboratory has studied. Simulation results revealed that strong light was emitted near 60 to 70 degree taper angles, as in the visible light range.

In the next step, optimal bump allocation was derived for the 70 degrees taper angle. In this study, the light guide plate we fabricated had bumps in a 48 mm \times 88 mm area on a 52 mm \times 96 mm \times 2.6 mm board. The optimal bump allocation was determined by thinning filled bumps, on the basis of simulation results. From simulation results, the fully uniform placement of bumps was obtained [3]. Before bump allocation optimization, output characteristics were such that the maximum value was 6.39 W/m^2 and the minimum value was 1.15 W/m^2 . After optimization, the maximum value was reduced to 3.23 W/m^2 , while the minimum value was increased to 1.82 W/m^2 . The uniformity ratio, which is an indicator of the degree of illumination uniformity, improved from 35 % to 91 %.

Fabrication of light guide plate

Since the shape was micro sized, the UV-LIGA process was used to fabricate an UV light guide plate, designed as above. As regards the master pattern, a structure was created by lithography, painting with resist that is photosensitive resin wafer. Next, copper was sputtered onto the surfaces of the created master pattern. A mold was then fabricated through Ni electroforming. Consequently, the Ni thickness was set at approximately 4 mm for electroforming. Lastly,

the light guide plate was produced through injection molding using the mold as a cavity [3]. The achieved bump shape was obtained at 10 μm in top diameter, 52 μm in base diameter, 70 degrees in taper angle and 30 μm in height.

Evaluation of light guide plate

Using a photodiode, the emission characteristics of the fabricated light guide plate were measured to verify that the light guide plate would provide uniform illumination. Energy values were calculated from the spectral response characteristics of the photodiode and the wavelength of the light emitted by the LED. The energy distribution was obtained as closely simulation result, as shown in Fig. 2. In the simulation, the maximum and minimum values were 3.23 W/m^2 and 1.82 W/m^2 , respectively, while the molded light guide plate provided maximum and minimum values of 4.25 W/m^2 and 3.10 W/m^2 , respectively. The maximum value increase from the simulation results was probably due to some entry angle deviation that occurred at LED mounting. However, the higher minimum value suggests that the fabricated light guide plate was better than the simulated one used for analysis.

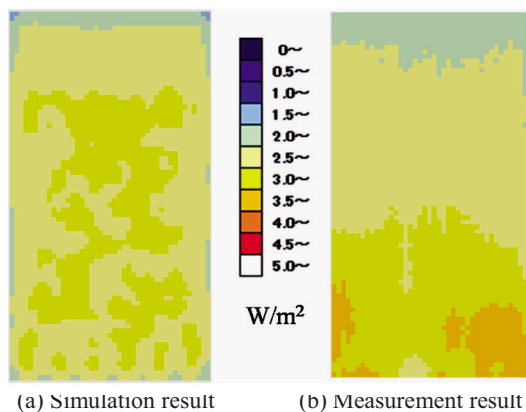


Fig. 2: Energy distribution of light guide plate

Measurement of photocatalyst

In light of such trends, using the light guide plate fabricated in this study we conducted an experiment involving the processing of toluene gas discharged during printing, or from adhesives. We performed what the repetition experiment that we used an active carbon and photocatalyst for, experiment by the change of the irradiation energy and experiment only by photocatalyst. Deodorization measurements using a photocatalyst are conducted either dynamically, by incorporating an external force to generate air flow, or statically, by using a closed space allowing no air flow. In our study, the experiment of the latter type was in a static environment.

In the first experiment, 100 ppm of toluene gas was injected to the container, and the toluene gas concentration was measured 60 minutes later. On the basis of concentration measurement results, toluene

gas was again added so as to achieve 100 ppm. This cycle was repeated several times. Figure 3 shows experiment results. Since no UV light was irradiated in the initial period, the activated carbon came close to saturation after several cycles, diminishing in toluene-processing capacity. However, after a few hours of UV irradiation, the processing capacity of photocatalyst and activated carbon recovered from approximately 50 % to approximately 90 %.

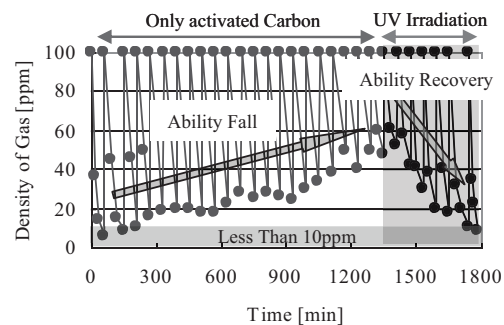


Fig. 3: Results of deodorization measurement for toluene gas

Conclusions

We fabricated an unprecedented UV surface illuminator and assessed its capacity as a light source for reactivating photocatalysts. Bump shape and allocation for uniform illumination of UV light were derived through simulation, achieving uniformity ratio improvement from 35 % to 91 %. The light guide plate for UV light was fabricated using UV-LIGA process. The fabricated light guide plate presented performance comparable to simulation results, with a minimum value exceeding analysis results, though the uniformity ratio did not reach the simulation results.

We intend to conduct processing measurements similar to the toluene gas decomposition experiment, and to closely assess the relationships between energy value and photocatalyst processing capacity. Moreover, for additional increases in emitted energy value, we will review the UV-light diffuser design through simulation.

References

- [1] T. Tanaka, T. Nomura, Y. Funabiki, T. Kitadani, K. Idei, K. Yamashita, D. Noda, and T. Hattori, Proc. of the 2006 IEEE Int. Symp. on Micro-Nano Mechatronics and Human Science, Nagoya, Japan, pp. 480-485 (2006).
- [2] Y. Sawa, T. Tanaka, T. Kitadani, H. Ueno, Y. Itoigawa, K. Yamashita, D. Noda, and T. Hattori, Microsyst. Technol., 14, pp. 1559-1565 (2008).
- [3] Y. Okayama, K. Yamashita, D. Noda, and T. Hattori, Proc. the 2008 IEEE Int. Symp. on Micro-Nano Mechatronics and Human Science, Nagoya, Japan, pp. 408-413 (2008).

Fabrication of Micro Capacitive Inclination Sensor by Resin Molding Method

Hiroaki Miyake¹, Kazufumi Nishimoto¹, Satoshi Nishida², Daiji Noda¹, and Tadashi Hattori¹

¹Laboratory of Advanced Science and Technology for Industry, University of Hyogo,

²Nanocreate Co., Ltd.

Abstract

In various leading-edge technology industries, there is a growing need to reduce the weight and increase the energy saving performance of various electronics products. It is now under development to enable the production of less expensive MEMS devices for low costly production technology. Then, the LIGA process is a technology, which is considered to be suited for mass production, enabling the creation of a microstructure by transferring a pattern from this master mold to a resin. In this study, we fabricated a micro capacitive inclination sensor by using combination of a resin forming method and a mold. We could fabricate and successfully package a resin sensor by molding technique that can be made at low cost production. If a small inclination sensor, having a size of several millimeters, could be made using a resin forming method, production costs could be substantially reduced compared to sensors made with the conventional MEMS process.

Introduction

In various leading-edge technology industries, there is a growing need to reduce the weight and increase the energy saving performance of various electronics products. Although MEMS (Micro Electro Mechanical Systems) technology [1] is not suited for mass-produced sensors since silicon is brittle and expensive and its processing is complicated, involving many processes. On the other hand, the LIGA process is a technology, which is considered to be suited for mass production, enabling the creation of a microstructure by transferring a pattern from this master mold to a resin.

In this study, we fabricated a micro capacitive inclination sensor [2] by using combination of a resin forming method and a mold. If a small inclination sensor, having a size of several millimeters, can be made using a resin forming method, production costs can be substantially reduced compared to sensors made with the conventional MEMS process. Since the dimensions of its sensing region are $7 \times 7 \times 3$ mm³, which are much smaller than the dimensions of conventional sensors, this inclination sensor is expected to be widely used in the field where efficient and reliable attitude control is a primary factor to be considered.

Micro capacitive inclination sensor

This is working principle of a micro capacitive inclination sensor that two semicircular opposing electrodes are set above one circular common electrode [2]. Therefore, two capacitors are formed. The region between the opposing electrodes and common electrode is half filled with oil. The oil inside maintains its level due to gravity when the sensor inclines, so that the amount of oil changes in each capacitor. As a result, the capacitances change, and the angle of inclination of the sensor can be detected, based on this change in the capacitance

values. Capacitance change of the capacitor on the one side of the electrodes ΔC is expressed the proportional inclination angle θ [2].

Fabrication process of sensor

Figure 1 shows the fabrication process for the micro capacitive inclination sensor. In the first step, a mold to be used for forming was prepared by UV (ultraviolet) lithography and Ni electroforming (Figs. 1(A) to (F)). The spacer part of this mold was transferred to a resin by hot embossing molding (Figs. 1(G) and (H)) [3]. The common electrode was formed on a structure having projections and recesses (Figs. 1(I) to (M)). The opposing electrodes, formed by transferring the pattern, were then attached to the common electrode, oil was injected, and the injection port was then sealed to complete the fabrication of the inclination sensor (Figs. 1(N) to (P)). Specifically, an electrode film was formed, only at the recesses on the slit-structured surface having projections and recesses. A patterning method using a mask would be a viable method for forming an electrode at a specified position. Using this method, however, it is very difficult to bring a mask into proper alignment with a non-flat surface; this method also has a drawback in respect of cost. In the case of the process that is the subject of this paper, a significant cost reduction is possible, since an electrode film can be formed without using a mask.

Formation of electrode on resin molding

The inclination sensor comprises two electrodes, i.e., a common electrode and opposing electrode, to form a capacitor. Figure 2 shows images of the cross section of a molding on which resist had been coated, using a spin/spray coating system. As shown in this

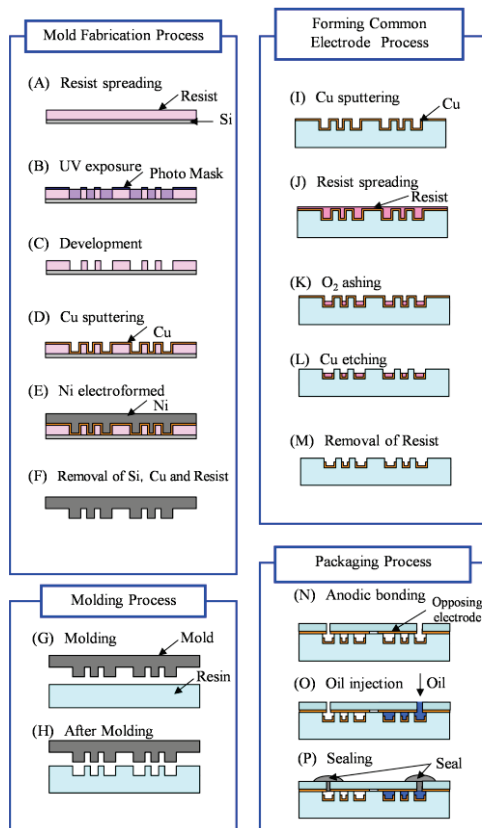


Fig. 1: Fabrication process for sensor using molding

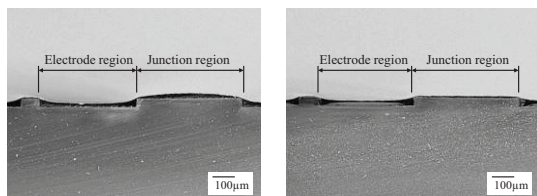


Fig. 2: SEM image of pattern in cross section

image, resist smoothly followed the projections and recesses in the pattern. After resist coating, the thickness of the resist film on the electrode region was the same at that of the film on the junction region. Therefore, if O_2 ashing were performed on a molding having a uniform thickness of resist, resist could not remain only in the recess in the electrode region. Therefore, we placed a resist-coated sample in a container filled with solvent vapor so that resist, exposed to solvent vapor, would melt and be planarized. As is evident from Fig. 2b, the resist coating on the junction part was very thin, compared with a sample, shown in Fig. 2a, which had not yet been planar. Cu electrode was thus formed successfully, only in the recess in the structure, using the proposed new process.

We successfully fabricated a micro inclination sensor as a molded product [4]. In future, we will carry out wiring to complete this inclination sensor,

and then conduct performance evaluations, as shown in Fig. 3.

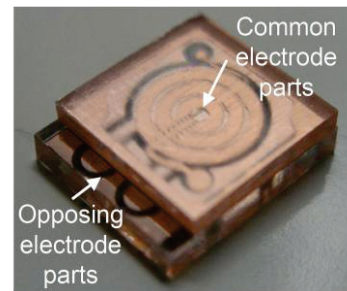


Fig. 3: Picture of completed sensor

Conclusions

Based on low cost molding techniques suited for mass production, we have fabricated a micro capacitive inclination sensor by using a resin molded component. We prepared a mold by UV lithography and Ni electroforming. In addition, using the hot embossing molding technique, we fabricated a structure in which our pre-designed projections and recesses were realized.

We proposed a new process for forming electrodes, only in the recesses in a fabricated resin molded component, without using a mask, and successfully fabricated the common electrode of an inclination sensor. The process proposed and established in this study requires no alignment and makes possible a substantial cost reduction. Although we faced a difficult task of planarizing resist in this process, we used solvent vapor for planarization with satisfactory results. We successfully fabricated a micro inclination sensor as a molded product. In future, we will carry out wiring to complete this inclination sensor, and then conduct performance evaluations.

The techniques using resin-molded parts have the potential to be applied to the production of, not only inclination sensors, such as the one fabricated in this study, but also MEMS devices. If the techniques using resin-molded parts are introduced to the mass-production of MEMS devices, including sensors, at low cost, the range of their applications will further expand to new areas of technology and industry.

References

- [1] F. Kohsaka, J. Liang, T. Matsuo, and T. Ueda, IEEJ Trans. SM, **127**, 10, pp. 431-436 (2007).
- [2] H. Ueda, H. Ueno, K. Itoigawa, and T. Hattori, IEEJ Trans. SM. **126**, 12, pp. 637-642 (2006).
- [3] N. Ishizawa, K. Idei, T. Kimura, D. Noda, and T. Hattori, Microsyst. Technol., **14**, 9-11, pp. 1381-1388 (2008).
- [4] H. Miyake, K. Nishimoto, H. Ueda, H. Ueno, K. Itoigawa, S. Nishida, D. Noda, and T. Hattori, IEEJ Trans. SM, **129**, 9, pp. 283-288 (2009).